QED Corrections in the Radiative Return Method during Measurement of the $e^+e^- \longrightarrow \pi^+\pi^-$ Cross-Section below 1 GeV[¶]

M. I. Konchatnij, N. P. Merenkov*, and O. N. Shekhovtzova

National Science Center Kharkov Institute of Physics and Technology, Kharkov, 61108 Ukraine
*e-mail: merenkov@kipt.kharkov.ua
Received June 23, 2003

We discuss radiative corrections during the measurement of the $e^+e^- \longrightarrow \pi^+\pi^-$ cross-section by the radiative return method without photon tagging. The radiative corrections to the initial-state radiation process are computed for DAΦNE conditions using the quasireal electron approximation for both the cross-section and the underlying kinematics. The efficiency of experimental rules for event selection by the restrictions on the lost invariant mass and so-called "track mass" is estimated. Some numerical calculations illustrate our analytical results. © 2003 MAIK "Nauka/Interperiodica".

PACS numbers: 13.66.Bc; 13.40.-f; 12.20.Ds

1. Testing the consistency of the SM requires a variety of measurements for which radiative corrections play a crucial role. Among such corrections, effects caused by hadronic vacuum polarization in the photon propagator occupy a special place in electroweak precision physics. Because the interaction coupling between quarks and gluons increases at low energies, the corresponding contributions cannot be calculated by *p*QCD but may be computed via dispersion integrals over the experimental e^+e^--annihilation data. Therefore, a precise determination of these effects in the running fine structure constant α^{had} and in the muon anomalous magnetic moment a_μ depends on the precision of the low-energy hadronic cross section $\sigma_h(e^+e^- \longrightarrow$ hadrons) [1–3]. A recent theoretical analysis of these quantities [4] showed that existing data is insufficient at least to solve two important problems: to make a more precise prediction about the location of the light Higgs mass [5] and to draw a conclusion about possible "new physics" (beyond the SM) which would contribute to a_μ [6].

The measurement of σ_h at e^+e^--annihilation by radiative return using the initial state radiation (ISR) process has become an objective reality in resent years [7, 8]. Theoretical aspects of such measurements accounting for radiative corrections (RC) were studied firstly in [9] for the case of collinear small-angle ISR events. Further different approaches, including both analytical calculations [10] and Monte Carlo generators [11],

have been developed to describe the small- and large-angle ISR photon events and satisfy experimental selection rules used at Φ and *b* factories, where the respective experiments have yet to begin.

It is the general opinion that the high-luminosity DAΦNE machine operating in the Φ-resonance region is the ideal collider to scan $\sigma_h(q^2)$ with the center-of-mass energy $\sqrt{q^2}$ varying from the threshold up to 1 GeV just by ISR radiative events. In this region, $\sigma_h(q^2)$ is mainly fulfilled by ρ resonance that decays into the pair $\pi^+\pi^-$. The KLOE detector at DAΦNE measures the 3-momenta of charged pions and selects with high efficiency events with a fixed value of the squared pion invariant mass $q^2 = (p_- + p_+)^2$ in the ISR radiative process

$$e^-(p_1) + e^+(p_2) \longrightarrow \pi^+(p_+) + \pi^-(p_-) + \gamma(k) \qquad (1)$$

without straightforward registration of an ISR photon. This approach makes it possible to use events with collinear photons, which fly in the so-called blind zone and cannot be detected by KLOE calorimeters. Such a method has some advantages, because the corresponding cross section becomes larger by a logarithm enhancement factor $L_0 = \ln(E^2\theta_0^2/m^2)$, where E is the beam energy, θ_0 is the maximum angle of the collinear photon, and m is the electron mass.

In the Born approximation, one can apply the quasireal electron method (QRE) [12] to write the cross section of the process (1) with small-angle ISR photons in

terms of the cross section $\sigma(q^2)$ of the process $e^+ + e^- \longrightarrow \pi^+ + \pi^-$

$$\frac{d\sigma^B}{dq^2} = \frac{\sigma(q^2)}{4E^2}\frac{\alpha}{2\pi}P(z, L_0),$$

$$P(z, L_0) = \frac{1+z^2}{1-z}L_0 - \frac{2z}{1-z}, \qquad (2)$$

$$z = \frac{q^2}{4E^2}, \quad L_0 = \ln\frac{E^2\theta_0^2}{m^2}.$$

However, one must apply an additional restriction on event selection to exclude background due to possible strong 3-pion decays: $\omega \longrightarrow \pi^+\pi^-\pi^0$ and $\Phi \longrightarrow \pi^+\pi^-\pi^0$. The reason is that, in this case, the photon is not detected, and these decays can in general imitate events such as reaction (1), because the neutral pion also remains invisible. It is obvious that, to get rid of such a 3-pion background, one may to select events with the small lost-invariant mass M_{lost}, which is smaller than the pion mass

$$M_{lost}^2 = (p_1 + p_2 - p_+ - p_-)^2 < m_\pi^2. \qquad (3)$$

At the Born level, this restriction is always satisfied, because in this case $M_{lost}^2 = k^2 = 0$. Thus, it has to be taken into account only when calculating the contribution in RC to cross section (2) caused by additional hard photon emission. Such an additional photon, in principle, can be radiated from the initial as well as from the final states. But the collinear (with respect to the electron beam) final state radiation (FSR) is suppressed by a factor of θ_0^2, and even for $\theta_0 = 10°$ the approximation in which terms of the order θ_0^2 are neglected has a very high accuracy, on the level of RC. Therefore, one may consider only the contribution to RC due to hard ISR photons with their invariant mass less than m_π.

2. Instead of restriction (3), in [13] it was suggested to select events with a small difference between the lost energy and the lost 3-momentum modulus

$$\Omega - |\mathbf{K}| < \eta E, \quad \Omega = 2E - E_+ - E_-,$$
$$|\mathbf{K}| = |\mathbf{p}_+ + \mathbf{p}_-|, \quad \eta = 0.02, \qquad (4)$$

where $E_\pm$ ($\mathbf{p}_\pm$) are the energies (3-momenta) of $\pi^\pm$. For reaction $e^+ + e^- \longrightarrow \pi^+ + \pi^- + 2\gamma$, the quantity Ω ($\mathbf{K}$) is the total energy (3-momentum) of two photons. In any event, the lost squared invariant mass cannot be more than $2E(\Omega - |\mathbf{K}|)$; therefore, choice $\eta \leq m_\pi^2/2E^2 \simeq 0.039$ provides an exclusion of the 3-pion background. Thus, inequality (4), in fact, is equivalent to (3).

Restriction (3) defines the upper limit of Ω variation as

$$\Omega_{max} = E(1-z)\left(1 + \frac{\eta}{2}\right). \qquad (5)$$

The corresponding RCs were calculated in [14] neglecting terms of the order η.

In real experiments at DAΦNE, another rule for event selection called "track mass" selection was used [7]:

$$M_{tr} - m_\pi < \Delta M_{tr} \simeq 10 \text{ MeV}. \qquad (6)$$

The track mass M_{tr} for the multiphoton annihilation process $e^+ + e^- \longrightarrow \pi^+ + \pi^- + n\gamma$ is defined such that $E_\pm = \sqrt{\mathbf{p}_\pm^2 + M_{tr}^2}$, provided that for the lost energy one must use $2E - E_+ - E_- = |\mathbf{K}|$ but not Ω, as given in (4). It is clear that in the Born approximation $\Omega = |\mathbf{K}|$, $M_{tr} = m_\pi$ and for $n > 1$ always $M_{tr} > m_\pi$. At the measured 3-momenta $\mathbf{p}_+$ and $\mathbf{p}_-$,

$$M_{tr}^2 = \frac{1}{4}\left[(2E - |\mathbf{K}|)^2 - 2(\mathbf{p}_+^2 + \mathbf{p}_-^2) + \frac{(\mathbf{p}_+^2 - \mathbf{p}_-^2)^2}{(2E - |\mathbf{K}|)^2}\right]. \qquad (7)$$

To express the squared pion mass, we have to substitute Ω instead of $|\mathbf{K}|$ on the right-hand side of Eq. (7). It is clear from physical considerations that track mass selection has to lead to some constraint like (4) and (5), because there is no other possibility to avoid 3-pion final states (at the measured 3-momenta of charged pions) except to forbid large lost invariant mass.

By expanding the difference $M_{tr}^2 - m_\pi^2$ with respect to small quantities $\Delta M_{tr}/E$ and $(\Omega - |\mathbf{K}|)/E$ and using inequality (6), we arrive at

$$\Omega < E(1-z)\left[1 + \frac{\eta(x)}{1+z}\right],$$

$$\eta(x) = \frac{2m_\pi M_{tr}}{E^2}f(x), \qquad (8)$$

$$f(x) = \frac{4x}{(1+x)^2}, \quad x = \frac{E_-}{E_+}.$$

At fixed the squared dipion invariant mass q^2, the energies of pions can be expressed via the scattering angle of a pion with respect to the electron beam direction and the pion mass by the following relation:

$$E_- = \frac{2z[1 + z - (1-z)cK]}{(1+z)^2 - (1-z)^2c^2},$$

$$K = \sqrt{1 - \frac{\delta^2}{z^2}[(1+z)^2 - (1-z)^2c^2]}, \qquad (9)$$

$$E_+ + E_- = E(1+z), \quad c = \cos\theta, \quad \delta = \frac{m_\pi}{2E},$$

where θ is the π^- polar angle.

In the limiting cases $z = 1$ (very soft the ISR photon) and $z = m_\pi^2/E^2$ (at threshold), $E_+ = E_-$ and $f(x) = 1$. In the most interesting region of ρ resonance, the ratio E_-/E_+ changes between 2 and 0.5, which gives

$$\frac{8}{9} < f(x) < 1.$$

The minimum and maximum values of the ratio E_-/E_+ correspond to back-to-back events when a pion with the smaller energy flies in the direction of the ISR photon ($c = 1$), and a pion with the larger energy, in the opposite direction ($c = -1$). If the angle θ increases, the maximum (minimum) value of this ratio decreases (increases) and most events tend to concentrate near $f(x) \simeq 1$. Thus, with good enough accuracy, one can calculate RC in the case of track mass event selection by the simple substitution

$$\eta \longrightarrow \frac{\bar{\eta}}{1+z}, \quad \bar{\eta} = \frac{4m_\pi\Delta M_{\text{tr}}}{E^2} = 0.0225 \quad (10)$$

in the analytical formulas of work [14]. It follows from comparison that inequalities (5) and (8) at $f(x) = 1$.

In Fig. 1a, we compare the total RC for event selection with restrictions (6) (curve *1*) and (4) (curve *2*) in terms of quantity δ^{RC} defined as

$$\frac{d\sigma_{\text{obs}}}{dq^2} = \frac{d\sigma^B}{dq^2}(1 + \delta^{\text{RC}}), \quad (11)$$

where $d\sigma_{\text{obs}}$ is the observed cross section, which includes effects of radiative corrections, and $d\sigma^B$ is defined by Eq. (2). One can see that use of the track mass selection leads to slight loss (for about 1.5–2%) in events in the region of ρ resonance ($0.5 < z < 0.7$) as compared with selection defined by rule (4). It is said that the efficiency of selection (4) is slightly higher than selection (6). As we see, it depends on RC caused by an additional hard photon emission.

3. To estimate the absolute efficiency of event selection by restrictions (4) or (6), one needs to know the number of events without any such restriction. The rest of this paper is dedicated to calculation of RCs in this case provided that at least one collinear ISR photon flies in the direction of the electron beam. For such events, the inequality

$$\mathbf{K}\mathbf{p}_1 > |\mathbf{K}|Ec_0, \quad c_0 = \cos\theta_0, \quad (12)$$

is valid, and to describe radiation of this photon, we use the QRE approximation for both the cross section form and underlying kinematics.

The total RC includes contributions due to additional virtual, soft (with energy less than ΔE, $\Delta \ll 1$), and hard (with energy more than ΔE) photon emission. Virtual and soft corrections do not depend on restrictions on the quantity $\Omega - |\mathbf{K}|$ and must be taken as given
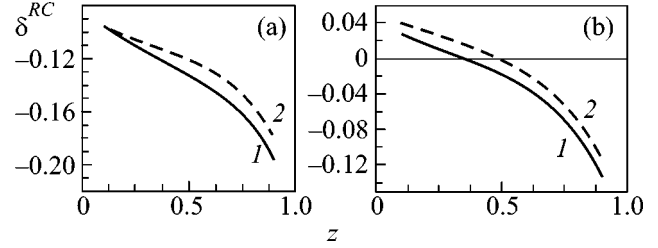
Fig. 1. z dependence of the quantity δ^{RC} as given by Eq. (11) for different restrictions on event selection. Curves in Fig. 1a derived at $\theta_0 = 5°$ by the help of formulas (63) in [14] and rule (10). Curve *1* takes into account restriction (6), and curve *2*, restriction (4). Figure 1b illustrates RC without any restriction on the lost invariant mass for $\theta_0 = 5°$ (curve *1*) and $\theta_0 = 10°$ (curve *2*) derived at this work using Eqs. (22) and (23).

in [14]. It is convenient to divide the correction caused by hard photons into three parts. The first one describes events when both photons fly inside the narrow cone with the opening angle $2\theta_0$ along the electron beam direction. The corresponding contribution to the cross section at the accuracy used also does not depend on the above-mentioned restrictions and was found in [14].

The second part corresponds to events when one photon flies in the electron beam direction while the second one flies along the positron beam inside the narrow cone with the opening angle $2\theta_0'$, $\theta_0' \ll 1$. In the QRE approximation, the respective cross section has the form

$$\frac{d\sigma_2^H}{dq^2} = \frac{\sigma(q^2)}{4E^2}\left(\frac{\alpha}{2\pi}\right)^2\int_{\sqrt{z}}^{1-\Delta} P\left(\frac{z}{y}, L_0\right)P(y, L_0')\frac{dy}{y},$$

$$(13)$$

$$L_0' = \ln\frac{E^2\theta_0'^2}{m^2},$$

where the energy fraction of a photon in the electron beam direction is $1 - z/y$, and in the positron beam, $1 - y$. To determine the lower limit of integration, we have to bear in mind that the event must be considered as radiation along the electron beam (due to inequality (12)); therefore, the energy fraction $1 - z/y$ must be larger than $1 - y$ or $y > \sqrt{z}$.

It is convenient to represent the result of integration on the right-hand side of Eq.(13) as

$$\frac{d\sigma_2^H}{dq^2} = \frac{\sigma(q^2)}{4E^2}\left(\frac{\alpha}{2\pi}\right)^2$$

$$\times\left[2P(z, L)\ln(1-z)(L_0 - 1) - \frac{1+3z^2}{2(1-z)}\ln zLL_0\right.$$

$$+\left(\frac{z(1+z)}{1-z}\ln z - 1 + z\right)(L + L_0) - 2(1-z)\ln(1-\sqrt{z})l_\theta$$

$$-\frac{2z}{1-z}\ln z - 2P(z, L_0)(L-1)\ln\Delta - G_4 l'_\theta\Bigg],$$

$$\tag{14}$$

$$l'_\theta = \ln\frac{\theta'_0}{4},$$

$$G_4 = \left(\frac{1+3z^2}{2(1-z)}\ln z + 1 - z\right)L_0$$

$$-\frac{z(1+z)}{1-z}\ln z + 2(1-z)\ln(1-\sqrt{z}),$$

$$L = \frac{4E^2}{m^2}.$$

Note that the parameter θ_0 defines rule (12) for event selection and is a physical one, while the infrared parameter Δ and angular collinear parameter θ'_0 are auxiliary and have to disappear in the final result for the total RC. The auxiliary angular parameter vanishes when the third part of the RC, due to hard photon emission, is added. This part corresponds to events when one hard photon with 4-momentum $k_1 = (\omega_1, \mathbf{k}_1)$ belongs to the forward narrow cone (with respect to the electron beam) and the other one with 4-momentum $k_2 = (\omega_2, \mathbf{k}_2)$ escapes both (forward and backward) narrow cones, but 3-momentum $\mathbf{K} = \mathbf{k}_1 + \mathbf{k}_2$ lies inside the forward cone as defined by condition (12).

In accordance with the QRE approximation, the starting point for our calculations of the respective differential cross section, suitable for the unrestricted pion phase space, is the following:

$$d\sigma_3^H = \frac{\sigma(q^2)}{4E^2}\frac{\alpha}{2\pi}P(x, L_0)$$

$$\times L_{\mu\nu}^\gamma(xp_1, p_2, k_2)\tilde{g}_{\mu\nu}\frac{\alpha}{4\pi^2}\frac{dxd^3k_2}{x\omega_2},\tag{15}$$

$$\frac{d^3k_2}{\omega_2} = 2\pi\omega_2 d\omega_2 dc_2, \quad c_2 = \cos\theta_2, \quad x = 1 - \frac{\omega_1}{E},$$

where θ_2 is the polar angle of the noncollinear photon and for $L_{\mu\nu}^\gamma(p_1, p_2, k)$ see, for example, [15]. Since our aim is to derive the differential distribution in the squared pion invariant mass q^2, it is convenient to use the relation between q^2 and c_2 to avoid integration over c_2 on the right-hand side of Eq. (15). In addition, it is convenient to use the total photon energy Ω instead of ω_2,

$$q^2 = 4E(E - \Omega) + 2\omega_1\omega_2(1 - c_2),$$

$$\omega_2 = \Omega - \omega_1, \quad dc_2 \longrightarrow \frac{dq^2}{2\omega_1\omega_2}, \quad d\omega_2 = d\Omega.\tag{16}$$

Because the photon with 4-momentum k_2 is a noncollinear one, we can neglect the electron mass in the expression for $L_{\mu\nu}^\gamma$ on the right-hand side of Eq. (15) and write the distribution over the dipion squared invariant mass in the following form:

$$\frac{d\sigma_3^H}{dq^2} = \frac{\sigma(q^2)}{4E^2}\left(\frac{\alpha}{2\pi}\right)^2\Bigg\{-L_0 - \frac{4(L_0-1)E\Omega_z}{\omega_1^2} - \frac{zE^2L_0}{(E-\omega_1)^2} + \frac{2zE - [(1+z)E + \Omega_z]L_0}{E-\omega_1}$$

$$+ \frac{[2(1+z)^2 - 4z - (1-z)^2]E^2 + (1+z)(1-2L_0)E\Omega_z + \Omega_z^2 L_0 - (1-z)(\Omega - 2\omega_1)E}{Z}\Bigg\}\frac{d\omega_1 d\Omega}{E\Omega_z},\tag{17}$$

$$\Omega_z = \Omega - E(1-z), \quad Z = \omega_1(\Omega - \omega_1) - E\Omega_z.$$

This distribution differs from that given in [14], where restriction (4) was also applied and approximation $\Omega = E(1-z)$ used for all terms nonsingular at this point. It is not a case for the considered situation, because the upper limit of integration with respect to Ω now differs considerably from $E(1-z)$. To find the integration region in (17), we have to take into account, together with condition (12),

$$-c'_0 < c_2 < c_0, \quad \Delta E < \omega_1 < \Omega - \Delta E,$$

$$c'_0 = \cos\theta'_0.\tag{18}$$

The system of inequalities (12) and (18) defines the integration region with respect to ω_1 and Ω as given by relations (47) in [14] with one very essential change: $\Omega_{\max} = 2E(1 - \sqrt{z})$. This region is shown in Fig. 2.

The list of all necessary integrals which contribute in the limiting case $1 - c_0 \ll 1$, $1 - c'_0 \ll 1$ is

$$\frac{1}{E\Omega_z} = 2(1-z), \quad \frac{1}{\Omega_z(E-\omega_1)} = \ln^2 z + 2Li_2(1-z),$$

$$\frac{E}{\Omega_z (E - \omega_1)^2} = -\frac{2}{z} \ln z,$$

$$\frac{1}{Z} = -\frac{1}{2} \ln z (l_\theta - l'_\theta) + \frac{\pi^2}{6} - \frac{1}{4} \ln^2 z + 2 Li_2(-\sqrt{z}),$$

$$l_\theta = \ln \frac{\theta_0^2}{4},$$

$$\frac{\Omega_z}{EZ} = \left[z - 1 - \frac{1+z}{2} \ln z \right] (l_\theta - l'_\theta) + 2\sqrt{z}(1 - \sqrt{z})$$

$$+ z \ln z - (1 - z) \ln(1 - \sqrt{z})$$

$$+ (1 + z) \left[\frac{\pi^2}{6} - \frac{1}{4} \ln^2 z + 2 Li_2(-\sqrt{z}) \right], \qquad (19)$$

$$\frac{E}{Z \Omega_z} = \frac{1}{1-z} \left[-\frac{1}{2} l_\theta^2 - (l_\theta + l'_\theta) \ln \frac{1-z}{\Delta} - \frac{1}{2} \ln z (l_\theta + l'_\theta) \right.$$

$$\left. + \frac{\pi^2}{3} - \frac{1}{4} \ln^2 z + 2 Li_2(-\sqrt{z}) \right],$$

$$\frac{\Omega - 2\omega_1}{Z \Omega_z} = \frac{1}{2} l_\theta^2 + (l_\theta + l'_\theta) \ln \frac{1-z}{\Delta}$$

$$+ 2(l_\theta - l'_\theta) \ln(1 + \sqrt{z}) + 2 \ln^2(1 + \sqrt{z})$$

$$- 4 Li_2(1 - \sqrt{z}) + 4 Li_2 \left(\frac{1 - \sqrt{z}}{1 + \sqrt{z}} \right) + \frac{\pi^2}{2},$$

where we omit for brevity the symbol of the integral and differentials $d\omega_1$ and $d\Omega$ on the left sides of these relations.

The corresponding cross section reads

$$\frac{d\sigma_3^H}{dq^2} = \frac{\sigma(q^2)}{4E^2} \left(\frac{\alpha}{2\pi} \right)^2$$

$$\times [2 P(z, L_0) G_1 + L_0 G_2 + G_3 + G_4 l'_\theta],$$

$$G_1 = -\frac{1}{2} l_\theta^2 - \ln \frac{(1-z)\sqrt{z}}{\Delta} l_\theta + \frac{\pi^2}{3} - \frac{1}{4} \ln^2 z + 2 Li_2(-\sqrt{z}),$$

$$G_2 = \left[z - 1 + \frac{1+z}{2} \ln z \right] l_\theta - 2(1 - \sqrt{z})$$

$$+ (2 + z) \ln z - 2(1 - z) \ln(1 + \sqrt{z})$$

$$- (1 + z) \left[\frac{\pi^2}{6} + \frac{3}{4} \ln^2 z + Li_2(1 - z) + Li_2(-\sqrt{z}) \right], \qquad (20)$$

$$G_3 = -[2(1 - z) \ln(1 + \sqrt{z}) + z \ln z] l_\theta$$

$$+ (3z - 2) \frac{\pi^2}{3} + z \left[\frac{3}{2} \ln^2 z + 4(Li_2(1 - z) + Li_2(-\sqrt{z})) \right]$$
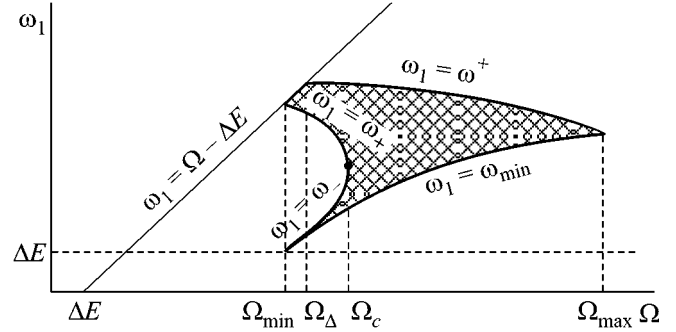
Fig. 2. The integration region with respect to ω_1 and Ω in cross section (17), as defined by inequalities (47) in [14] (where all the notation is also given) but with $\Omega_{max} = 2E(1 - \sqrt{z})$.

$$+ 2(1 - z) \left[-\ln^2(1 + \sqrt{z}) \right.$$

$$\left. + 2 \left(Li_2(1 - \sqrt{z}) - Li_2 \left(\frac{1 - \sqrt{z}}{1 + \sqrt{z}} \right) \right) \right].$$

As one can see, terms containing l'_θ enter with opposite signs in (14) and (20) and vanish in their sum.

To eliminate the infrared auxiliary parameter Δ and write the total RC to the Born cross section (2) of radiative process (1) under the considered conditions for event selection, we have to sum all possible contributions:

$$\frac{d\sigma^{RC}}{dq^2} = \frac{d\sigma^{S+V}}{dq^2} + \frac{d\sigma_1^H}{dq^2} + \frac{d\sigma_2^H}{dq^2} + \frac{d\sigma_3^H}{dq^2}. \qquad (21)$$

The expressions for $d\sigma^{S+V}$ and $d\sigma_1^H$ are given by Eqs. (30), (31) and (35)–(37) in [14], respectively. Using these expressions, as well as (14) and (20), after some algebraic exercise, we arrive at

$$\frac{d\sigma^{RC}}{dq^2} = \frac{\sigma(q^2)}{4E^2} \left(\frac{\alpha}{2\pi} \right)^2 [P_{2\theta}(z) L_0^2$$

$$+ P(z, L_0) H_1(l_\theta, z) + L_0 H_2(z) + H_3(z)], \qquad (22)$$

where $P_{2\theta}(z)$ is the well-known θ term of the second-order electron structure function in a nonsinglet channel caused by photonic corrections

$$P_{2\theta}(z) = 2 \frac{1 + z^2}{1 - z} \left(\ln \frac{(1-z)^2}{z} + \frac{3}{2} \right) + (1 + z) \ln z - 2 + 2z$$

and

$$H_1(l_\theta, z) = -l_\theta^2 - l_\theta(3 + 2\ln(1 - z)^2 z) - \frac{5}{2}$$

$$-4\ln\frac{1-z}{z} - \frac{1}{2}\ln^2 z + \frac{5\pi^2}{3} + 4Li_2(-\sqrt{z}) - 2Li_2(z),$$

$$H_2(z) = 2\sqrt{z} - \frac{1+z}{2} - \frac{9z}{1-z} + \frac{1+5z}{1-z}\ln z$$

$$-\frac{1+z}{4}\ln^2 z - 2(1-z)\ln(1+\sqrt{z})$$

$$-(1+z)\left(\frac{\pi^2}{6} + 2Li_2(1-z) + 2Li_2(-\sqrt{z})\right),$$

$$H_3(z) = -\frac{8}{3} + \frac{5}{3(1-z)} + \frac{3-18z+7z^2}{3(1-z)^2} \qquad (23)$$

$$+\frac{3-3z+3z^2-9z^3-2z^4}{6(1-z)^3}\ln^2 z + 2z\ln^2(1-z)$$

$$-2(1-z)\ln^2(1+\sqrt{z}) + \left(\frac{26}{3z} - 2 - \frac{1}{1-z}\right)\frac{\pi^2}{6}$$

$$+\left(4z - 2 + \frac{1}{1-z}\right)Li_2(z) + \frac{3+5z}{3}Li_2(1-z)$$

$$-4(1-z)Li_2\left(\frac{1-\sqrt{z}}{1+\sqrt{z}}\right)$$

$$+4(1-z)Li_2(1-\sqrt{z}) + 4zLi_2(-\sqrt{z}) + J(z).$$

The quantity $J(z)$ in H_3 is defined as

$$J = \int_0^{1-z}\left\{\frac{z^2+(1-x)^4}{x\lambda(1-x)^2}\left[\frac{1}{2}L_2^2(x,z) + Li_2\left(\frac{2xz}{h}\right)\right.\right.$$

$$\left.+ Li_2\left(-\frac{2x^2\lambda}{h}\right) + Li_2\left(-\frac{\lambda}{xz}\right)\right]$$

$$\left.+ \frac{z+x}{2(1-x)}L_1(x,z) + \frac{x\lambda-3z}{2(1-x)^2}L_2(x,z)\right\}dx,$$

where

$$h = \lambda(1-x)^2 + x(z-x\lambda) + (1-x)\sqrt{F(x,z)},$$

$$L_1(x,z) = \ln\frac{(x+z)\sqrt{F(x,z)} + \lambda(z-x\lambda) + x(x+z)^2}{2z\lambda},$$

$$L_2(x,z) = \ln\frac{(1-x)\sqrt{F(x,z)} + x(z-x\lambda) + \lambda(1-x)^2}{2\lambda(1-x)^2},$$

$$F(x,z) = \lambda^2(1-x)^2 + 2x\lambda(z-x\lambda) + 2x^2(x+z)^2.$$

In Fig. 1b, we show the quantity δ^{RC} (at two values of θ_0) defined in the same way as in Eq. (11), where

$\delta^{RC} = d\sigma^{RC}/d\sigma^B$ and now $d\sigma^{RC}$ is given by Eq. (22). Change of the limiting angle from 5° up to 10° increases the RC by about 1.5%. On the other hand, the curves on Figs. 1a and 1b at fixed angle θ_0 indicate that the use of restrictions (4) or (6) decreases the number of events by about 10% as compared with the considered case, without constraint on the lost invariant mass.

Both these effects can be understood very easily at the qualitative level because they are caused by an expansion of the real photon phase space, which provides an additional positive contribution into RC. Note that the loss in events due to use of restrictions (4) or (6) is rather small and is a very modest sacrifice for the 3-pion background that can be removed by them.

REFERENCES

1. S. Eidelman and F. Jegerlehner, Z. Phys. C **67**, 585 (1995).

2. R. Alemany, M. Davier, and A. Höcker, Eur. Phys. J. C **2**, 123 (1998).

3. M. Davier, S. Eidelman, A. Höcker, and Z. Zhang, hep-ph/0208177.

4. H. Burkhardt and B. Pietrzyk, LAPP-EXP, 2001-03; F. Jegerlehner, hep-ph/0104304; hep-ph/0105283.

5. Z. Zhao, G. Eigen, G. Burdman, *et al.*, hep-ex/0201047.

6. J. Gluza, A. Hoefer, S. Jadach, and F. Jegerlehner, hep-ph/0212386.

7. B. Valeriani *et al.* (KLOE Collaboration), hep-ex/0205046; A. G. Denig (KLOE Colaboration), hep-ex/0211024.

8. E. D. Solodov (BABAR Collaboration), hep-ex/0107027; N. Berger, hep-ex/0209062.

9. A. B. Arbuzov, E. A. Kuraev, N. P. Merenkov, and L. Trentadue, J. High Energy Phys. **12**, U148 (1999).

10. M. Konchatnij and N. P. Merenkov, JETP Lett. **69**, 811 (1999); V. A. Khoze, M. I. Konchatnij, N. P. Merenkov, *et al.*, Eur. Phys. J. C **18**, 481 (2001); M. I. Konchatnij and N. P. Merenkov, Zh. Éksp. Teor. Fiz. **122**, 33 (2002) [JETP **95**, 26 (2002)]; G. Rodrigo, H. Czyz, J. H. Kühn, and M. Szopa, Eur. Phys. J. C **24**, 71 (2002); G. Rodrigo and J. H. Kühn, Eur. Phys. J. C **25**, 215 (2002).

11. S. Binner, J. H. Kühn, and K. Melnikov, Phys. Lett. B **459**, 279 (1999); K. Melnikov, F. Nguyen, B. Valeriani, and G. Venanzoni, Phys. Lett. B **477**, 114 (2000); H. Czyz and J. H. Kühn, Eur. Phys. J. C **18**, 497 (2001); S. Spagnolo, Eur. Phys. J. C **6**, 637 (1999).

12. V. N. Baier, V. S. Fadin, and V. A. Khoze, Nucl. Phys. B **65**, 381 (1973).

13. G. Cataldi, A. Denig, W. Kluge, and G. Venanzoni, KLOE MEMO, No. 195 (1999).

14. V. A. Khoze, M. I. Konchatnij, N. P. Merenkov, *et al.*, Eur. Phys. J. C **25**, 199 (2002).

15. É. A. Kuraev, N. P. Merenkov, and V. S. Fadin, Yad. Fiz. **45**, 782 (1987) [Sov. J. Nucl. Phys. **45**, 486 (1987)].

Pseudoscalar Mesons and Their Radial Excitations from the Effective Chiral Lagrangian[¶]

S. M. Fedorov and Yu. A. Simonov

Institute of Theoretical and Experimental Physics, Moscow, 117218 Russia
e-mail: fedorov@heron.itep.ru, simonov@heron.itep.ru
Received June 25, 2003

The effective chiral Lagrangian is derived from QCD in the framework of the field correlator method. It contains the effects of both confinement and chiral symmetry breaking due to a special structure of the resulting quark mass operator. It is shown that this Lagrangian describes light pseudoscalar mesons, and Gell-Mann–Oakes–Renner relations for pions, eta and K mesons are reproduced. The spectrum of radial excitations of pions and K mesons is found and compared to experimentally known masses. © *2003 MAIK "Nauka/Interperiodica".*

PACS numbers: 12.39.Fe; 14.40.Aq; 12.38.Lg; 11.30.Rd; 11.15.Tk

1. QCD is known to possess two highly nontrivial features at low temperatures, namely, confinement and chiral symmetry breaking (CSB). At some critical temperature, phase transitions of deconfinement and chiral symmetry restoration occur. From lattice calculations, it is known that these two phase transitions take place at the same temperature [1, 2]. The fact that two critical temperatures coincide was not fully understood. This work is a continuation of a series of papers [3–5], where it is argued that CSB occurs due to confinement in a very nontrivial way.

It was shown in [3] that effective four-quark interaction leading to spontaneous chiral symmetry breaking occurs in QCD due to confinement and is associated with the QCD string. Thus, CSB is closely connected to confinement. In this approach, the effective chiral Lagrangian (ECL) containing fields of light pseudoscalar mesons is derived from the QCD Lagrangian. This is done by integrating out gluon fields and performing bosonization. At the same time, confinement is taken into account through the specific form of gluon-field correlators.

As a result, expanding in powers of (derivatives) of bosonic fields, one obtains the ECL similar to the celebrated Gasser–Leutwyler Lagrangian [6], but in the nonlocal form [3].

We expand ECL in powers of meson fields and reproduce the standard Gell-Mann–Oakes–Renner relations, while meson masses are zero in the chiral limit. It is shown that the vanishing of meson masses happens due to cancellation of two terms in the Green's functions of mesons. The poles of the Green's function corresponding to radial excitations of pseudoscalar mesons are displaced from the masses obtained in the

Hamiltonian approach without CSB effects (see, e.g., [7] and references therein) and are shifted down by less than 15%.

2. We consider a Euclidean partition function for quarks and gluons in the presence of external classical currents v_μ, a_μ, s, and p:

$$Z = \int DAD\overline{\psi}D\psi \exp[-(S_0 + S_1 + S_{int} + S_{g.f.} + S_{gh})],$$

$$S_0 = \frac{1}{4}\int d^4x (F^a_{\mu\nu})^2,$$

$$S_1 = -i\int d^4x \overline{\psi}^f (\hat{\partial} + \hat{v} + \gamma_5\hat{a} + s + i\gamma_5 p)^{fg}\psi^g,$$

$$S_{int} = -\int d^4x \overline{\psi}^f g\hat{A}^a t^a \psi^f. \tag{1}$$

Here, f, g = 1, 2, 3 are flavor indices, t^a are generators of color $SU(3)$ group, $\mathrm{tr}\, t^a t^b = \delta^{ab}/2$, $a = 1, ..., 8$. $S_{g.f.}$ and S_{gh} are gauge-fixing and ghost terms.

Next, we use the generalized contour gauge [8, 9]

$$A_\mu(x) = \int_0^1 ds \frac{\partial z_\nu(s, x)}{\partial s}\frac{\partial z_\rho(s, x)}{\partial x_\mu}F_{\nu\rho}(z(s)). \tag{2}$$

Here, $z_\nu(s, x)$ belongs to a set of contours with the properties $z_\nu(0, x) = x_0$, $z_\nu(1, x) = x_\nu$, and x_0 is a fixed point. In what follows, the exact position of contours is unimportant for our analytical results, while for numerical estimates we will assume that contours are chosen to minimize the spectrum (and area of the string world sheet), to be called the minimal set of contours.

The reason we use the contour gauge is that it allows us to express gauge field A_μ through field strength tensor $F_{\mu\nu}$. Now we are in position to integrate out gluon

---

[¶] This article was submitted by the authors in English.

field A_μ, expressing the result in terms of field correlators:

$$Z = \iint D\overline{\psi}D\psi\exp[-(S_1 + S_{\text{eff}})],$$

$$\exp[-S_{\text{eff}}] = \langle\exp[-S_{\text{int}}]\rangle_A. \tag{3}$$

We use the cluster expansion to evaluate this average over gluon fields

$$\langle\exp[-S_{\text{int}}]\rangle_A = \exp\left(\sum_n \frac{(-1)^n\langle\langle S_{\text{int}}^n\rangle\rangle}{n!}\right),$$

$$\langle\langle S_{\text{int}}\rangle\rangle = \langle S_{\text{int}}\rangle_A \equiv 0, \tag{4}$$

$$\langle\langle S_{\text{int}}^2\rangle\rangle = \langle S_{\text{int}}^2\rangle_A - \langle S_{\text{int}}\rangle_A^2 = \langle S_{\text{int}}^2\rangle_A,$$

....

It is clear that gauge-invariant quantities like the spectrum and the Green's functions computed with the help of S_{eff} do not depend on the chosen contours if all terms of cluster expansion are retained in (4). In what follows, we will use the Gaussian approximation and consider only the first two terms in the cluster expansion, $n = 1$, 2. As was shown in [10, 11], the Gaussian approximation on minimal surfaces is accurate to within a few percent. Thus, we have

$$S_{\text{eff}} = -\frac{1}{2}\int d^4x d^4y\, \overline{\psi}_{i\alpha}^f(x)\psi_{j\beta}^f(x)\overline{\psi}_{k\gamma}^g(y)\psi_{l\delta}^g(y)$$

$$\times\int_0^1 ds dt\frac{\partial z_\rho(s,x)}{\partial s}\frac{\partial z_\lambda(s,x)}{\partial x_\mu}\frac{\partial z_{\rho'}(t,y)}{\partial t}\frac{\partial z_{\lambda'}(t,y)}{\partial y_\nu} \tag{5}$$

$$\times\langle[F_{\rho\lambda}(z(s,x))]_{ij}[F_{\rho'\lambda'}(z(t,y))]_{kl}\rangle_A(\gamma^\mu)_{\alpha\beta}(\gamma^\nu)_{\gamma\delta}.$$

Here, i, j, k, l are color indices, $\alpha, \beta, \gamma, \delta$ are spinor indices. Inserting parallel transporters $\Phi(x, x_0)$ and $\Phi(y, x_0)$, which are identically equal to unity in the contour gauge, one finally gets an expression for effective action:

$$S_{\text{eff}} = -\frac{1}{2}\int d^4x d^4y\, \overline{\psi}_{i\alpha}^f(x)\psi_{j\beta}^f(x)\overline{\psi}_{k\gamma}^g(y)\psi_{l\delta}^g(y)$$

$$\times\left(\delta_{jk}\delta_{il} - \frac{1}{N_c}\delta_{ij}\delta_{kl}\right)J_{\alpha\beta\gamma\delta}(x,y),$$

$$J_{\alpha\beta\gamma\delta}(x,y) = (\gamma_\mu)_{\alpha\beta}(\gamma_\nu)_{\gamma\delta}J_{\mu\nu}(x,y),$$

$$J_{\mu\nu}(x,y) = \frac{1}{N_c^2 - 1} \tag{6}$$

$$\times\int_0^1 ds dt\frac{\partial z_\rho(s,x)}{\partial s}\frac{\partial z_\lambda(s,x)}{\partial x_\mu}\frac{\partial z_{\rho'}(t,y)}{\partial t}\frac{\partial z_{\lambda'}(t,y)}{\partial y_\nu}$$

$$\times\text{tr}\langle F_{\rho\lambda}(z(s,x),x_0)F_{\rho'\lambda'}(z(t,y),x_0)\rangle_A,$$

$$F(u,x_0) \equiv \Phi(x_0,u)F(u)\Phi(u,x_0).$$

Performing bosonization and keeping only scalar–isoscalar and pseudoscalar–isovector (corresponding to pions, K and η mesons) terms, one arrives at the quark–meson Lagrangian (see [4] for details):

$$Z = \int D\overline{\psi}D\psi DM_s D\phi_a\exp[-S_{\text{QM}}],$$

$$S_{\text{QM}} = -\int d^4x d^4y[\overline{\psi}_{i\alpha}^f(x)$$

$$\times(i(\hat{\partial} + \hat{v} + \gamma_5\hat{a} + s + i\gamma_5 p)_{\alpha\beta}^{fg}\delta^{(4)}(x-y)$$

$$+ iM_s(x,y)\hat{U}_{\alpha\beta}^{fg}(x,y))\psi_{i\beta}^g(y) \tag{7}$$

$$- 2N_f(J(x,y))^{-1}M_s^2(x,y)],$$

$$J(x,y) = J_{\mu\mu}(x,y),$$

$$\hat{U}_{\alpha\beta}^{fg}(x,y) = \exp(i\gamma_5 t_a\phi_a(x,y))_{\alpha\beta}^{fg}.$$

It is now straightforward to integrate out quark fields to obtain the effective chiral Lagrangian:

$$Z = \int DM_s D\phi_a\exp[-S_{\text{ECL}}],$$

$$S_{\text{ECL}} = 2N_f\int d^4x d^4y(J(x,y))^{-1}M_s^2(x,y) - W(\phi),$$

$$W(\phi) = N_c\text{tr}\ln[i(\hat{\partial} + \hat{v} + \gamma_5\hat{a} + s + i\gamma_5 p) \tag{8}$$

$$+ iM_s(x,y)e^{i\gamma_5 t_a\phi_a(x,y)}].$$

Here, tr refers to flavor and spinor indices and to space coordinates. M_s is the effective quark mass operator and ϕ_a are fields of pseudoscalar mesons (up to the dimensional factor $2/f$, f is the decay constant, $\phi_a = 2\pi_a/f$).

The classical equations of motion are given by

$$N_c\text{Tr}(-S_\phi(x,y)M_s(x,y)e^{i\gamma_5 t_a\phi_a(x,y)}\gamma_5 t_a) = 0,$$

$$N_c\text{Tr}(iS_\phi(x,y)e^{i\gamma_5 t_a\phi_a(x,y)})$$

$$- 4N_f(J(x,y))^{-1}M_s(x,y) = 0, \tag{9}$$

$$S_\phi(x,y) \equiv \langle x|\frac{1}{i\hat{\partial} + iM_s e^{i\gamma_5 t_a\phi_a}}|y\rangle.$$

This leads to solutions

$$\phi_a^{(0)}(x,y) = 0,$$

$$M_s^{(0)}(x,y) = \frac{N_c}{4N_f}J(x,y)\text{Tr}(S(x,y)), \tag{10}$$

$$S(x,y) \equiv S_\phi(x,y)|_{\phi=0}.$$

The second equation in (10) is a nonlinear equation for $M_s^{(0)}$, and the existence of a nontrivial solution is a manifestation of the chiral symmetry breaking, since $M_s^{(0)}$ is scalar. The system of equations (10) for $M_s^{(0)}$ and $S(x,y)$ was considered in [12] for the special case

of heavy–light mesons, and it was shown that it has a confining scalar solution for $M_s^{(0)}(x, y) \simeq \sigma|\mathbf{x} - \mathbf{x}_0|\delta^{(4)}(x - y)$ for large distance $|\mathbf{x} - \mathbf{x}_0|$ from the quark to the (heavy) antiquark at the point $\mathbf{x}_0$. It is clear that the same type of solution occurs at large interquark distances for light–light mesons, which means that confinement and CSB occur spontaneously and simultaneously from the nontrivial solution of the system (10).

3. We consider ECL (8), expanding it in powers of the field ϕ_a up to the second order, and we introduce current quark masses $\mathcal{M}_f \equiv \mathrm{diag}(m_u, m_d, m_s)$. Neglecting external currents, one obtains

$$W(\phi) = N_c \mathrm{tr}\ln[i(\hat{\partial} + \mathcal{M}_f + M_s e^{i\gamma_5 t_a \phi_a})]$$

$$= N_c \mathrm{tr}\ln\Big[i(\hat{\partial} + \mathcal{M}_f + M_s)$$

$$+ \Big(-M_s\gamma_5 t_a\phi_a - \frac{i}{2}M_s t_a t_b \phi_a \phi_b\Big)\Big], \quad (11)$$

$$W^{(2)}(\phi) = -\frac{N_c}{2}\mathrm{tr}[iS(M_s t_a t_b \phi_a \phi_b)$$

$$+ S(M_s t_a \phi_a)\gamma_5 S\gamma_5(M_s t_b \phi_b)].$$

Taking the trace in flavor indices (see [4] for details), one arrives at the following expression for the term quadratic in meson fields:

$$W^{(2)}(\phi) = -\int d^4x d^4y\Big[W_{\pi\pi}(x, y)\phi_\pi^*(x)\phi_\pi(y)$$

$$+ W_{KK}(x, y)\phi_K^*(x)\phi_K(y) + W_{K^0 K^0}(x, y)\phi_{K^0}^*(x)\phi_{K^0}(y) \quad (12)$$

$$+ \frac{1}{2}\sum_{i, j = 3, 8} W_{ij}(x, y)\phi_i(x)\phi_j(y)\Big],$$

where, for example,

$$W_{\pi\pi}(x, y) = \frac{N_c}{4}\mathrm{Tr}[S_u(x, y)M_s(y)\gamma_5 S_d(y, x)\gamma_5 M_s(x)$$

$$+ iS_u(x, x)M_s(x)\delta^4(x - y) + (u \longleftrightarrow d)]. \quad (13)$$

Here, S_u and S_d are quark propagators (10) with current mass of corresponding quark in the denominator. Here, we have taken the local limit of nonlocal operators $M_s(x, y) \longrightarrow M_s(x)\delta^4(x - y)$, $\phi(x, y) \longrightarrow \phi(x)$, which is obtained when the gluonic correlation length T_g in the correlator $\langle FF\rangle$ tends to zero.

The two terms in (13) correspond to connected and disconnected diagrams, which cancel each other in the zero momentum limit. This cancellation is exact in the

chiral limit. To be more precise, the quadratic term for zero momentum (i.e., when $\phi(x) = \mathrm{const}$) takes the form

$$W^{(2)}(\phi)\big|_{\text{zero momentum}} = \frac{N_c}{4}\int d^4x\Big[\frac{m_u + m_d}{2}$$

$$\times \mathrm{Tr}(-iS_u(x, x) - iS_d(x, x))\phi_\pi^*\phi_\pi + \dots\Big] + O(m^2). \quad (14)$$

Taking into account that

$$\langle\overline{\psi}\psi\rangle_M = -i\langle\overline{\psi}\psi\rangle_E$$

$$= -\frac{1}{Z}\frac{\delta Z[v, a, s, p]}{\delta s(x)} = -N_c\mathrm{Tr}(iS(x, x)), \quad (15)$$

where $\langle\overline{\psi}\psi\rangle_M$ and $\langle\overline{\psi}\psi\rangle_E$ denote a quark condensate in Minkowski and Euclidean space, respectively, and that $\phi_a = 2\pi_a/f$, where f is the decay constant and π_a are physical meson fields, one finds

$$f^2 M_{\pi^\pm}^2 = 2\hat{m}|\langle\overline{q}q\rangle| + O(m^4)$$

$$f^2 M_{\pi^0}^2 = 2\hat{m}|\langle\overline{q}q\rangle| - \varepsilon + O(\varepsilon^2) + O(m^2)$$

$$f^2 M_{K^\pm}^2 = (m_u + m_s)|\langle\overline{q}q\rangle| + O(m^2) \quad (16)$$

$$f^2 M_{K^0}^2 = (m_d + m_s)|\langle\overline{q}q\rangle| + O(m^2)$$

$$f^2 M_{\eta 8}^2 = \frac{2}{3}(\hat{m} + 2m_s)|\langle\overline{q}q\rangle| + \varepsilon + O(\varepsilon^2) + O(m^2).$$

Here, $\hat{m} = (m_u + m_d)/2$. We have neglected differences between quark condensates for different flavors, corrections are on the order of m_q^2. Small mixing of ϕ_3 and ϕ_8 states due to isospin symmetry breaking (proportional to $m_u - m_d$) yields a correction ε to pion and η meson masses:

$$\pi^0 \sim \cos(\delta)\phi_3 + \sin(\delta)\phi_8,$$

$$\eta_8 \sim -\sin(\delta)\phi_3 + \cos(\delta)\phi_8,$$

$$\tan(2\delta) = \sqrt{3}\frac{m_d - m_u}{2m_s - (m_u + m_d)}, \quad (17)$$

$$\varepsilon = \frac{|\langle\overline{q}q\rangle|(m_u - m_d)^2}{4m_s - 2(m_u + m_d)}, \quad \delta \simeq 0.6°.$$

Thus, ECL (8) leads to the correct Gell-Mann–Oakes–Renner relations for all light pseudoscalar mesons.

4. Let us now consider the Green's functions of mesons generated by the pseudoscalar currents:

$$\mathcal{G}_{ab}(x, y) = \langle J_a^5(x)J_b^5(y)\rangle = \frac{1}{Z}\frac{\delta^2 Z}{\delta p_a(x)\delta p_b(y)},$$

$$J_a^5(x) = \overline{\psi}(x)\gamma_5 t_a\psi(x), \quad (18)$$

$$p^{fg}(x) = p_a(x)t_a^{fg}.$$

From the ECL, one obtains

$$\mathfrak{G}_{ab}(x, y) = \frac{1}{Z}\int DM_s D\phi_a \exp[-S_{ECL}]$$

$$\times [N_c \mathrm{Tr}(S_\phi(x, y)\gamma_5 t_b S_\phi(y, x)\gamma_5 t_a)$$

$$- N_c^2 \mathrm{Tr}(S_\phi(x, x)\gamma_5 t_a)\mathrm{Tr}(S_\phi(y, y)\gamma_5 t_b)]. \tag{19}$$

Taking M_s at the stationary point (10) and expanding S_ϕ in terms of ϕ around $\phi_a^{(0)} = 0$, one finds

$$S_\phi(x, y) = S(x, y)$$

$$+ \int d^4 x S(x, z) M_s(z)\gamma_5 \phi_a(z) t_a S(z, y). \tag{20}$$

As argued in [4], the coupling constant $g_{\pi q\bar{q}}$ is on the order of $N_c^{-1/2}$, and, thus, in large N_c limit, pion exchanges are suppressed. This allows us to neglect pion fields in connected terms (the first term in equation (19)) and consider only one pion exchange in the disconnected term. The resulting expression will contain two terms, both on the order of N_c.

Taking into account that $S(x, y) = \mathrm{diag}(S_u(x, y), S_d(x, y), S_s(x, y))$ is diagonal in flavor, one finds

$$\mathfrak{G}_{\pi^+\pi^+}(x, y) = \frac{N_c}{2}\mathrm{Tr}(S_d(x, y)\gamma_5 S_u(y, x)\gamma_5)$$

$$- \frac{N_c^2}{4}\int d^4 z_1 d^4 z_2 \mathrm{Tr}(S_u(x, z_1)M_s(z_1)\gamma_5 S_d(z_1, x)\gamma_5) \tag{21}$$

$$\times \mathrm{Tr}(S_d(y, z_2)M_s(z_2)\gamma_5 S_u(z_2, y)\gamma_5)G^\phi_{\pi\pi}(z_1, z_2).$$

Other Green's functions differ only in flavor indices. Here, $G^\phi_{\pi\pi}(z_1, z_2) = \langle \phi_\pi^*(z_1)\phi_\pi(z_2)\rangle$ is the propagator of the pion field. This formula can be illustrated with the Feynman diagram:

$$\mathfrak{G}_{\pi^+\pi^+}(x, y) = \frac{N_c}{2}\overset{d}{\underset{u}{\bigcirc}} - \frac{N_c^2}{4}\overset{d}{\underset{u}{\bigcirc}}\cdots_{\pi^+}\overset{d}{\underset{u}{\bigcirc}}. \tag{22}$$

To find the pion propagator, one should consider equations (12), (13):

$$(G^\phi_{\pi\pi}(x, y))^{-1} = W_{\pi\pi}(x, y)$$

$$= \frac{N_c}{4}\mathrm{Tr}[2S_d(x, y)M_s(y)\gamma_5 S_u(y, x)M_s(x)\gamma_5 \tag{23}$$

$$+ i(S_d(x, x)M_s(x) + S_u(y, y)M_s(y))\delta^4(x - y)].$$

Going over to the momentum space $\mathfrak{G}(x, y) = \int d^4 k /(2\pi)^4 \exp(ik(x - y))\mathfrak{G}(k)$, where we have also taken into account that the Green's function is translationally invariant, i.e., depends only on $(x - y)$, one has

$$\mathfrak{G}_{\pi^+\pi^+}(k) = \frac{N_c}{2}G^{(0)}_{\pi^+\pi^+}(k)$$

$$- \frac{N_c^2}{4}G^{(0, M)}_{\pi^+\pi^+}(k)G^\phi_{\pi^+\pi^+}(k)G^{(0, M)}_{\pi^+\pi^+}(k), \tag{24}$$

$$G^{(0)}_{\pi^+\pi^+}(x, y) \equiv \mathrm{Tr}(S_d(x, y)\gamma_5 S_u(y, x)\gamma_5),$$

$$G^{(0, M)}_{\pi^+\pi^+}(x, y) \equiv \mathrm{Tr}(S_u(x, y)M_s(y)\gamma_5 S_d(y, x)\gamma_5).$$

Due to Eqs. (14)–(16), the pion propagator (23) has a pole at $k^2 = -M^2_{\pi^\pm}$ and can be rewritten as

$$G^\phi_{\pi^+\pi^+}(k) = \frac{2}{N_c}\frac{1}{G^{(0, MM)}_{\pi^+\pi^+}(k) - G^{(0, MM)}_{\pi^+\pi^+}(k^2 = -M^2_{\pi^\pm})}, \tag{25}$$

$$G^{(0, MM)}_{\pi^+\pi^+}(x, y) \equiv \mathrm{Tr}(S_u(x, y)M_s(y)\gamma_5 S_d(y, x)M_s(x)\gamma_5).$$

As argued in [4], all three Green's functions $G^{(0)}_{\pi^+\pi^+}$, $G^{(0, M)}_{\pi^+\pi^+}$, and $G^{(0, MM)}_{\pi^+\pi^+}$ have the same set of poles, which are poles of the quark model (i.e., confined $\bar{q}q$ system without chiral symmetry breaking) in pseudoscalar channel, and can be represented as

$$G^{(0)}_{\pi^+\pi^+}(k) = -\sum_{n=0}^{\infty}\frac{c_n^2}{k^2 + m_n^2},$$

$$G^{(0, M)}_{\pi^+\pi^+}(k) = -\sum_{n=0}^{\infty}\frac{c_n c_n^{(M)}}{k^2 + m_n^2}, \tag{26}$$

$$G^{(0, MM)}_{\pi^+\pi^+}(k) = -\sum_{n=0}^{\infty}\frac{(c_n^{(M)})^2}{k^2 + m_n^2},$$

where

$$c_n = \sqrt{\frac{m_n}{2}}\varphi_n(0),$$

$$c_n^{(M)} = \sqrt{\frac{m_n}{2}}M(0)\varphi_n(0), \tag{27}$$

$\varphi_n(\mathbf{r})$ is the 3D spin-singlet wave function of $\bar{q}q$ system, and $M(0)$ is a constant related to the mass operator M_s, evaluated in [5] through $\sigma = 0.18$ GeV^2 and

$T_g = 1$ GeV^{-1} to be $M(0) = 148$ MeV. Thus, one has for the pion Green's function

$$\mathfrak{G}_{\pi^+\pi^+}(k) = -\frac{N_c}{2}\frac{\Psi(k)}{(k^2 + M_{\pi^\pm}^2)\Phi(k)},$$

$$\Psi(k) = \sum_{n,m=0}^{\infty}\frac{c_n^2(c_m^{(M)})^2}{(k^2 + m_n^2)(m_m^2 - M_\pi^2)},\qquad (28)$$

$$\Phi(k) = \sum_{n=0}^{\infty}\frac{(c_n^{(M)})^2}{(k^2 + m_n^2)(m_n^2 - M_\pi^2)}.$$

Clearly, the Green's function (28) has pole at $k^2 = -M_{\pi^\pm}^2$, and all poles of the quark model are cancelled, since the same set of poles appears in functions $\Psi(k)$ and $\Phi(k)$. The radial excitations of the $\pi^\pm$ meson are given by zeros of the function $\Phi(k)$. In the first approximation, it reads

$$k^2 = -m_1^2(1 + \delta_1),$$

$$\delta_1 = -\frac{1}{m_1^2}\frac{c_1^2(m_1^2 - m_0^2)(m_0^2 - M_{\pi^\pm}^2)}{c_1^2(m_0^2 - M_{\pi^\pm}^2) + c_0^2(m_1^2 - M_{\pi^\pm}^2)}.\qquad (29)$$

The masses of K^0 and $\overline{K}^0$ radial excitations can be found from (29) by replacing π meson mass and reference spectrum with those for K mesons. Numerical results for masses of radial excited states are presented in the next section.

It should be mentioned that the η meson requires separate consideration because of its mixing with isoscalar state η', which is different for mesons and their radial excitations. Study of the η-meson spectrum and mixings is planned for a future work.

5. Masses and wave functions of the reference spectrum can be obtained from the QCD string Hamiltonian (first derived in [13–15] and improved to take into account quark self-energy in [16]), where we have put $L = 0$:

$$H = \frac{m_1^2}{2\mu_1} + \frac{m_2^2}{2\mu_2} + \frac{\mu_1 + \mu_2}{2} + \frac{p_r^2}{2\tilde{\mu}} + \sigma r - \frac{4}{3}\frac{\alpha_s}{r}.\qquad (30)$$

Here, m_1 and m_2 are current masses of quarks, μ_1 and μ_2 are einbein parameters, to be found from the eigenvalues of Hamiltonian (30) via $\partial\overline{M}_n(\mu_1, \mu_2)/\partial\mu_1 = 0$, $\partial\overline{M}_n(\mu_1, \mu_2)/\partial\mu_2 = 0$; $\tilde{\mu} = \mu_1\mu_2/(\mu_1 + \mu_2)$, and p_r is the radial component of momentum. This Hamiltonian allows one to find spin-averaged masses and wave func-

tions. Spin–spin interaction can then be taken into account as a perturbation:

$$M_n = \overline{M}_n(\mu_1, \mu_2) + \frac{32\pi\alpha_s \mathbf{s}_1\mathbf{s}_2}{9\mu_1\mu_2}|\varphi_n(0)|^2$$

$$+ \frac{4}{3}\left\langle\frac{\alpha_s}{r^3}\right\rangle\frac{\langle 3(\mathbf{s}_1\mathbf{n})(\mathbf{s}_2\mathbf{n}) - \mathbf{s}_1\mathbf{s}_2\rangle}{\mu_1\mu_2} + \Delta_{SE},\qquad (31)$$

$$\Delta_{SE} = -\frac{2\sigma}{\pi}\left(\frac{1}{\mu_1} + \frac{1}{\mu_2}\right)\eta;\quad \eta \sim 0.9\text{–}1.$$

Here, Δ_{SE} is the quark self-energy term due to field correlators. The factor η is a calculable function of current quark masses but is close to 1 when quark masses are small.

Next, we plug in numbers:

$$m_u = 0.005 \text{ GeV},\quad m_d = 0.009 \text{ GeV},$$
$$m_s = 0.17 \text{ GeV},\quad \sigma = 0.18 \text{ GeV}^2,\quad \alpha_s = 0.3.\qquad (32)$$

Taking into account that the lowest state is shifted exactly to the physical value of meson mass (due to the Gell-Mann–Oakes–Renner relations), we finally get the following chiral shift of reference (quark model) spectra:

pions:

$\pi(1S)$ 0.51 GeV $\longrightarrow$ 0.14 GeV (exact),

$\pi(2S)$ 1.51 GeV $\longrightarrow$ 1.25 GeV (exp : 1.3 GeV),

$\pi(3S)$ 2.18 GeV $\longrightarrow$ 1.98 GeV (exp : 1.8 GeV);

K mesons:

$K(1S)$ 0.63 GeV $\longrightarrow$ 0.49 GeV (exact),

$K(2S)$ 1.57 GeV $\longrightarrow$ 1.43 GeV (exp : 1.46 GeV),

$K(3S)$ 2.21 GeV $\longrightarrow$ 2.1 GeV (exp : 1.83 GeV).

It can be seen that masses of radial excitations are shifted by less than 15%, and the shifts are small for high excitations. Moreover, one can estimate that $\delta M/M(4S) \simeq 0.05$ for pions and $\delta M/M(4S) \simeq 0.04$ for K mesons. Also, one can see that masses of higher excitations and the slope of the radial Regge trajectory differ from the experimental. The reason is that Hamiltonian (30) does not take into account effects of string breaking, which are important for highly excited states, since they have a large spatial extent. Our consideration can be refined by including these effects, which has been done for mesons without chiral effects in [17].

6. Effective chiral Lagrangian (8) is derived directly from the QCD Lagrangian in the framework of vacuum correlators method. This Lagrangian correctly describes light pseudoscalar mesons, which are massless in the chiral limit and satisfy the Gell-Mann–Oakes–Renner relations when quark masses are nonzero.

The poles of the quark model Green's function are shifted by less than 15%, and the shift is small for highly excited states.

REFERENCES

1. F. Karsch, hep-lat/9903031.

2. J. M. Carmona, M. D'Elia, L. Del Debbio, *et al.*, Nucl. Phys. B, Proc. Suppl. **106**, 607 (2002); hep-lat/0110058.

3. Yu. A. Simonov, Phys. Rev. D **65**, 094018 (2002); hep-ph/0201170.

4. Yu. A. Simonov, hep-ph/0302090.

5. Yu. A. Simonov, hep-ph/0305281.

6. J. Gasser and H. Leutwyler, Ann. Phys. (N.Y.) **158**, 142 (1984); J. Gasser and H. Leutwyler, Nucl. Phys. B **250**, 465 (1985); for a review see H. Leutwyler, hep-ph/9406283.

7. Yu. A. Simonov, hep-ph/9911237.

8. S. V. Ivanov and G. P. Korchemsky, Phys. Lett. B **154**, 197 (1985); S. V. Ivanov, G. P. Korchemsky, and A. V. Radyushkin, Yad. Fiz. **44**, 230 (1986) [Sov. J. Nucl. Phys. **44**, 145 (1986)].

9. V. I. Shevchenko and Yu. A. Simonov, Phys. Lett. B **437**, 146 (1998); hep-th/9807157.

10. V. I. Shevchenko and Yu. A. Simonov, Phys. Rev. Lett. **85**, 1811 (2000); hep-ph/0001299.

11. A. Di Giacomo, H. G. Dosch, V. I. Shevchenko, and Yu. A. Simonov, Phys. Rep. **372**, 319 (2002); hep-ph/0007223.

12. Yu. A. Simonov, Few-Body Syst. **25**, 45 (1998); hep-ph/9712248.

13. Yu. A. Simonov, Phys. Lett. B **226**, 151 (1989).

14. A. Yu. Dubin, A. B. Kaidalov, and Yu. A. Simonov, Phys. Lett. B **323**, 41 (1994).

15. A. Yu. Dubin, A. B. Kaidalov, and Yu. A. Simonov, Yad. Fiz. **56** (12), 213 (1993) [Phys. At. Nucl. **56**, 1745 (1993)]; hep-ph/9311344.

16. Yu. A. Simonov, Phys. Lett. B **515**, 137 (2001); hep-ph/0105141.

17. A. M. Badalian, B. L. Bakker, and Yu. A. Simonov, Phys. Rev. D **66**, 034026 (2002); hep-ph/0204088.

Optical Orientation of Atoms in Spontaneous Raman Scattering of Elliptically Polarized Light

A. V. Taĭchenachev, A. M. Tumaĭkin, and V. I. Yudin

Novosibirsk State University, Novosibirsk, Russia
e-mail: llf@admin.nsu.ru
Institute of Laser Physics of the Siberian Division of the Russian Academy of Sciences, Novosibirsk, 630090 Russia
Received May 6, 2003

A general approach to the problem of spontaneous transfer of light-induced anisotropy in the scheme of Raman scattering of resonance elliptically polarized light is developed. Depending on the type of the field-excited $(a) \longleftrightarrow (b)$ transition, the stationary distribution of atoms over the sublevels of the final level (c) coupled with the excited level only by the $(b) \longrightarrow (c)$ spontaneous transition is either isotropic and does not depend on field parameters or anisotropic. In the latter case, the anisotropy is determined by both field polarization and (at fairly large level momentum values) field detuning and intensity. © 2003 MAIK "Nauka/Interperiodica".

PACS numbers: 32.80.-t

1. The anisotropy of internal atomic states, which arises as a result of resonance interaction between polarized light and levels degenerate with respect to angular momentum projections, plays an important role in the explanation of many superhigh-resolution polarization spectroscopy results [1], the stability of polarization modes of gas laser generation [2], atomic laser cooling [3], the formation of optical lattices [4], polarization resonance fluorescence [5], etc.

The general statement of the problem of the resonance interaction between polarized light and atoms includes closed and open optical transitions. In closed transitions, the total occupancy of the working levels remains unchanged, and the optical ordering effect reduces to the redistribution of atoms over the Zeeman sublevels of the ground and excited states as a result of induced and spontaneous processes. Nonzero multipole moments are formed on the atomic level in the stationary state, which means the formation of a macroscopic anisotropy in the atomic ensemble. The theory of the resonance interaction between elliptically polarized light and atoms was developed for closed transitions in a series of our works [6]. Most of the optical transitions are, however, open; that is, atoms excited by a resonance field from the ground state through at the $(a) \longleftrightarrow (b)$ transition can experience transitions to other lower levels $(b) \longrightarrow (c)$, as in spontaneous Raman scattering [7]. We should then expect spontaneous decay to transfer not only the occupancy but also light-induced anisotropy created by the field in the excited state (b) to the (c) level. If this final level is long-lived (metastable or ground, as, for instance, when both levels (a) and (c) are hyperfine structure components), light-induced anisotropy is accumulated at it with time.

The statement of the problem of spontaneous decay of a state excited by stationary external polarized light goes back to the classical problems of polarization resonance fluorescence of atoms [5] and spontaneous Raman scattering [7], where it is also necessary to know how the final atomic levels are polarized. However, the final, integral in time, result of spontaneous decay to atomic levels in an open system of transitions has not been analyzed. Neither has the question been discussed of the information (memory) about the pumping field that such a process retains. More specifically, this is the question of the occupancy and anisotropy of open transition levels that are formed in stationary interaction with polarized light and of their dependence on external field parameters. Such questions arise in studying the problem of optically pumping atoms between hyperfine structure components by polarized light in the problem of laser frequency stabilization and in several other problems, where the state of atomic level anisotropy (multipole moments) should be controlled and the dependence of this state on light field polarization should be known. Precisely this aspect of the problem of interaction between polarized light and atoms at open optical transitions is considered below.

We stress once more that the interaction scheme under consideration is virtually equivalent to the scheme of spontaneous Raman scattering, but our ultimate goal is the determination of the anisotropic stationary distribution of atoms over magnetic sublevels rather than obtaining information about the spectral, angular, and polarization dependences of spontaneous radiation.

2. The simplest open transition model is a three-level atom (see figure), whose two lower levels (a) and
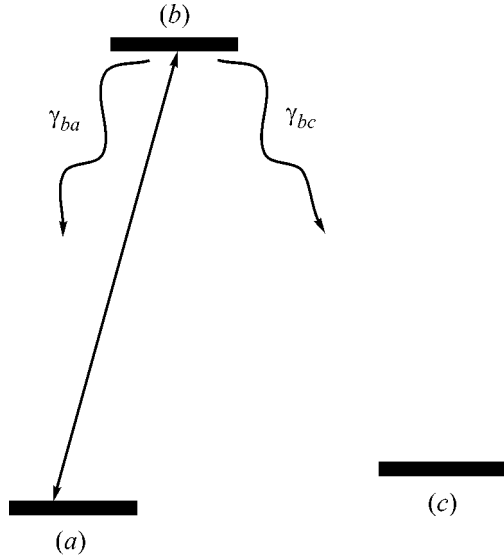
Scheme illustrating problem statement: a polarized field is in resonance with the (*a*) ←——→ (*b*)optical transition, and spontaneous pumping over from the (*b*) to the (*c*) level occurs. The distribution over magnetic sublevels in the (*c*) state is studied.

(*c*) are ground-state levels (for instance, these may be two hyperfine components) coupled with the excited state (*b*) by allowed electric dipole transitions. An external monochromatic light field with frequency ω and arbitrary elliptical polarization is in resonance with the (*a*) ←——→ (*b*) transition,

$$\mathbf{E}(t) = E\mathbf{e}\exp(-i\omega t) + \text{c.c.}, \tag{1}$$

where E is the complex field amplitude. The unit complex vector of elliptical polarization **e** is defined in the coordinate system in which the z axis is perpendicular to the plane of the ellipse and the x and y axes are directed along its principal axes,

$$\begin{aligned}
\mathbf{e} &= \cos\varepsilon\mathbf{e}_x + i\sin\varepsilon\mathbf{e}_y \\
&= \cos(\varepsilon + \pi/4)\mathbf{e}_{-1} - \cos(\varepsilon - \pi/4)\mathbf{e}_{+1}.
\end{aligned} \tag{2}$$

Here, the light ellipticity parameter ε is defined in the interval $-\pi/4 \le \varepsilon \le +\pi/4$ by setting the ratio between the small and large ellipse semiaxis lengths equal to $|\tan(\varepsilon)|$. The sign of ε determines the direction of light field polarization vector rotations.

The action of the light field described by (1) causes light-induced transitions between levels (*a*) and (*b*), whereas spontaneous decay from the excited state (*b*) redistributes atoms between the lower (*a*) and (*c*) states, including redistribution over their Zeeman sublevels. We assume that the (*c*) ←——→ (*b*) transition is far from resonance with the external field; that is, the (*c*) level is only related to (*b*) by spontaneous radiation. The radiation width of the excited level $\gamma_b = \gamma_{ba} + \gamma_{bc}$ is the sum of the partial spontaneous decay rates in the channels (*b*) —→ (*a*) and (*b*) —→ (*c*), and the relative arrange-

ment of the low-level energies is unimportant in the problem under consideration.

The evolution of atomic internal states is described by a linear dynamic equation for the density matrix $\hat{\rho}$. In the most general form, this equation can be written as

$$\frac{d}{dt}\hat{\rho} = \hat{L}\{\hat{\rho}\}, \tag{3}$$

where $\hat{L}$ is the Liouville operator including both light-induced and spontaneous processes. The action of $\hat{L}$ on the density matrix in the model of purely radiation relaxation can be written in the form

$$\begin{aligned}
\hat{L}\{\hat{\rho}\} = -i(\hat{H}\hat{\rho} - \hat{\rho}\hat{H}^\dagger) + \gamma_{ba}\sum_{q=0,\pm1}\hat{D}_q^\dagger(ba)\hat{\rho}\hat{D}_q(ba) \\
+ \gamma_{bc}\sum_{q=0,\pm1}\hat{D}_q^\dagger(bc)\hat{\rho}\hat{D}_q(bc),
\end{aligned} \tag{4}$$

where the irreducible tensor part of the dipole moment operator $\hat{D}_q(ba)$ is expressed through Clebsch–Gordan coefficients,

$$\hat{D}_q(ba) = \sum_{m_b, m_a} |F_b, m_b\rangle C_{F_a, m_a; 1, q}^{F_b, m_b}\langle F_a, m_a| \tag{5}$$

($\hat{D}_q(bc)$ can be written similarly). The effective Hamiltonian

$$\hat{H} = -(\delta + i\gamma_b/2)\hat{\Pi}_b + (\Omega\hat{V} + \text{h.c.}) \tag{6}$$

is the sum of the Hamiltonian of the free atom taking into account (*b*) level damping ($\delta = \omega - \omega_{ba}$ is the detuning from the resonance, $\hat{\Pi}_b = \sum_{m_b}|F_b, m_b\rangle\langle F_b, m_b|$ and the Hamiltonian of resonance interaction ($\hat{V} = \mathbf{e} \cdot \hat{\mathbf{D}}(ba)$ and Ω is the Rabi frequency).

Clearly, the stationary density matrix of atoms should satisfy the equation

$$\hat{L}\{\hat{\rho}(+\infty)\} = 0 \tag{7}$$

as $t \longrightarrow +\infty$. However, generally, this equation does not determine the stationary state unambiguously, because the zero subspace of the superoperator $\hat{L}$ can be degenerate. Such a situation is, in particular, characteristic of open transitions, whose special feature is the existence of states uncoupled with the field; that is, states in which the atom ceases to absorb light. Generally, two types of such states exist in the three-level system under consideration. The first type corresponds to the complete pumping over of atoms from the (*a*) to the (*c*) level, which does not participate in resonance interaction. The second type is related to the effect of coherent population trapping at the level (*a*), that is, to a possibility of the existence of a coherent superposition of

Zeeman sublevels that does not interact with the field (dark or coherent population trapping states) at the level (*a*) [6]. In the presence of both types of such states, some atoms are trapped at the level (*a*), and the rest, at the level (*c*). The distribution of atoms over the set of unbound states cannot be determined by Eq. (7) alone. There are many methods that allow the stationary distribution $\hat{\rho}(+\infty)$ to be unambiguously related to the initial distribution $\hat{\rho}(0)$ using evolution equation (3). For our purposes, the following variant is the most suitable. The integration of (3) in time from $t = 0$ to $t = +\infty$ yields the algebraic equation

$$\hat{\rho}(+\infty) - \hat{\rho}(0) = \hat{L}\{\hat{\tau}\}. \tag{8}$$

This equation relates $\hat{\rho}(+\infty)$ and $\hat{\rho}(0)$ to the matrix $\hat{\tau}$, which determines the characteristic times of ordering of atoms over internal degrees of freedom (generalized relaxation times),

$$\hat{\tau} = \int_{0}^{+\infty} (\hat{\rho}(t) - \hat{\rho}(+\infty))dt. \tag{9}$$

Given the initial matrix $\hat{\rho}(0)$, a solution to system (7), (8) unambiguously determines the stationary density matrix $\hat{\rho}(+\infty)$. As concerns the initial conditions, we assume that, at $t = 0$, the atoms are at level (*a*) with an isotropic distribution over sublevels; that is, $\hat{\rho}_a(0) = \hat{\Pi}_a/(2F_a + 1)$. Further, we will be interested in the stationary distribution at the final level (*c*) (at $F_c \neq 0$), which, according to (8), (4), is expressed for the given initial conditions through the operator of the relaxation time of the excited level (*b*) as

$$\hat{\rho}_c(+\infty) = \gamma_{bc} \sum_{q = 0, \pm 1} \hat{D}_q^\dagger(bc)\hat{\tau}_b\hat{D}_q(bc). \tag{10}$$

Note that, generally, at arbitrary angular momentum values, system (7), (8) of operator equations is fairly complex, and, as with closed transitions, its solutions are fundamentally different depending on the relative angular momenta of the levels F_a and F_b (which are related by the selection rules $F_b - F_a = 0, \pm 1$) and the presence or absence of the coherent population trapping effect for the $F_a \longleftrightarrow F_b$ transition excited by the field.

3. Briefly consider the principal results that follow from our analysis of system (7), (8).

First, if the spectrum of the $\hat{V}\hat{V}^\dagger$ operator does not contain zero eigenvalues, that is, if states uncoupled with the field are absent at the excited level (*b*), the stationary distribution on the (*c*) level is isotropic and does not depend on the polarization, intensity, or detuning of the pumping field. This most contraintuitive result characterizes all transitions with $F_b - F_a = -1$ at an arbitrary elliptical field polarization,

$$\hat{\rho}_c(+\infty) = \frac{\hat{\Pi}_c}{2F_c + 1} \frac{(2F_b + 1)\gamma_{bc}}{(2F_a + 1)\gamma_b - (2F_b + 1)\gamma_{ba}}, \tag{11}$$

and for the $F_b - F_a = 0$ transitions at half-integer momentum values and polarizations different from circular ($\varepsilon \neq \pm\pi/4$),

$$\hat{\rho}_c(+\infty) = \hat{\Pi}_c/(2F_c + 1). \tag{12}$$

Note that resonance fluorescence, integral in time, is then completely isotropic and nonpolarized, because $\hat{\tau}_b \propto \hat{\Pi}_b$. The distribution over the excited state (*b*) sublevels is, however, anisotropic at any fixed finite time *t*, which presupposes some angular and polarization dependence of scattered light. In addition, the characteristic time of attaining stationary state (12) for the $F_b - F_a = 0$ transitions with half-integer momentum values substantially depends on the ellipticity and tends to infinity as $\varepsilon \longrightarrow \pm\pi/4$.

The situation is quite different for the other transitions, that is, the $F_b - F_a = 1$ transitions and the $F_b - F_a = 0$ transitions with integer momentum values. For these transitions, there are always states uncoupled with the field at the excited (*b*) level [6]. For this reason, the $\hat{\tau}_b$ matrix cannot be isotropic. As a result, the stationary distribution at the (*c*) level is anisotropic and depends on the pumping field polarization. In the limiting cases of linear ($\varepsilon = 0$) and circular ($\varepsilon = \pm\pi/4$) polarizations, a solution can be obtained for arbitrary momentum values [8]. Without reproducing this solution, note that $\hat{\rho}_c(+\infty)$ then does not depend on the detuning δ and Rabi frequency Ω. In the general case of arbitrary ellipticity values, we found a solution to the problem for comparatively small level momenta ($F_a = 0$, 1/2, and 1). For $F_a = 0$ and 1/2 and $F_a = F_b = 1$, the stationary distribution at the (*c*) level was as previously independent of δ and Ω (naturally, the distribution depended on the ellipticity parameter ε). For instance, for the configuration of the levels $F_a = 0 \longleftarrow F_b = 1 \longrightarrow F_c = 1$, the nonzero components of orientation $\rho_{1q}^{(c)}$ and alignment $\rho_{2q}^{(c)}$, which characterize the stationary anisotropy at the (*c*) level, have the form

$$\rho_{10}^{(c)} = \frac{\sin(2\varepsilon)}{\sqrt{2}}; \quad \rho_{20}^{(c)} = -\frac{1}{2\sqrt{6}};$$

$$\rho_{2\pm2}^{(c)} = -\frac{1}{4}\cos2\varepsilon. \tag{13}$$

However, even for the $F_a = 1 \longleftrightarrow F_b = 2$ open transition, the $\hat{\rho}_c(+\infty)$ density matrix depends on all pumping field parameters, that is, ε, δ, and Ω. In particular, at $F_c = 2$ and in the weak field limit $\Omega \ll \gamma_b$, the stationary multipole moments for the (*c*) level are functions of the detuning δ and ellipticity ε,

$$\rho_{10}^{(c)} = \frac{2\sqrt{10}\sin(2\varepsilon)(11+c^2)(-9+(-25+22c^2)\tilde{\delta}^2)}{9(-11(9+25\tilde{\delta}^2)+c^4(1+92\tilde{\delta}^2)+c^2(-34+161\tilde{\delta}^2))},$$

$$\rho_{20}^{(c)} = \frac{2\sqrt{\frac{2}{7}}(-9-25\tilde{\delta}^2-c^2(16+31\tilde{\delta}^2)+c^4(1+52\tilde{\delta}^2))}{-11(9+25\tilde{\delta}^2)+c^4(1+92\tilde{\delta}^2)+c^2(-34+161\tilde{\delta}^2)}, \tag{14}$$

$$\rho_{2\pm2}^{(c)} = \frac{-2c(11+c^2)(-6\mp i\sin(2\varepsilon)\tilde{\delta}+(-15+14c^2)\tilde{\delta}^2)}{\sqrt{21}(-11(9+25\tilde{\delta}^2)+c^4(1+92\tilde{\delta}^2)+c^2(-34+161\tilde{\delta}^2))}$$

where, for brevity, we used the notation $\tilde{\delta} = \delta/\gamma_b$ and $c = \cos(2\varepsilon)$ and assumed the equality of the partial decay rates $\gamma_{ba} = \gamma_{bc}$. One can see that, at a field polarization different from linear and circular, the anisotropy of the (c) level substantially depends on δ (for instance, the change in orientation caused by the retuning $0 < \delta < 5\gamma_b$ may amount to dozens percent). It appears that this tendency should also be characteristic of levels with larger momentum values.

4. Note in conclusion that the theoretical results obtained in this work can be checked in sub-Doppler polarization spectroscopy experiments, in a scheme with a strong pumping field and a weak probe field tuned in resonance to some transition from the (c) level. The isotropy of the $\hat{\rho}_c(+\infty)$ density matrix would then mean the absence of the signal of polarization plane rotation for the probe field. As concerns the specific dependence on the detuning given by (14), it results in a selective velocity dependence of the elements of the $\hat{\rho}_c(+\infty)$ density matrix in an elliptically polarized field taking into account the Doppler frequency shift kv for moving particles. This should in turn manifest itself by narrow ($\sim\gamma_b$ wide) resonances in the rotation signal at long interaction times $\bar{t}\Omega^2/\gamma_b \gg 1$ ($\bar{t}$ is the mean flight time of the interaction of the atoms with the field), when usual sub-Doppler resonances experience considerable broadening. The first attempts at performing such experiments in rubidium vapor were reported in [9].

REFERENCES

1. C. Wieman and T. Hänsch, Phys. Rev. Lett. **36**, 1170 (1976).

2. D. Lenstra, Phys. Rep. **59**, 3 (1980).

3. J. Dalibard and C. Cohen-Tannoudji, J. Opt. Soc. Am. B **6**, 2023 (1989).

4. P. S. Jessen and I. H. Deutsch, in *Advances in Atomic, Molecular and Optical Physics*, Ed. by B. Bederson and H. Walter (1996), Vol. 37.

5. P. P. Feofilov, *The Physical Basis of Polarized Emission: Polarized Luminescence of Atoms, Molecules, and Crystals* (Fizmatgiz, Moscow, 1959; Consultants Bureau, New York, 1961).

6. V. S. Smirnov, A. M. Tumaĭkin, and V. I. Yudin, Zh. Éksp. Teor. Fiz. **96**, 1613 (1989) [Sov. Phys. JETP **69**, 913 (1989)]; A. V. Taĭchenachev, A. M. Tumaĭkin, V. I. Yudin, and G. Nienhuis, Zh. Éksp. Teor. Fiz. **108**, 415 (1995) [JETP **81**, 224 (1995)]; A. V. Taĭchenachev, A. M. Tumaĭkin, and V. I. Yudin, Zh. Éksp. Teor. Fiz. **110**, 1727 (1996) [JETP **83**, 949 (1996)]; G. Nienhuis, A. V. Taichenachev, A. M. Tumaikin, and V. I. Yudin, Europhys. Lett. **44**, 20 (1998); A. V. Taĭchenachev, A. M. Tumaĭkin, and V. I. Yudin, Zh. Éksp. Teor. Fiz. **118**, 77 (2000) [JETP **91**, 67 (2000)].

7. N. B. Delone and V. P. Kraĭnov, *Atom in a Strong Light Field* (Atomizdat, Moscow, 1978; Springer, Berlin, 1985).

8. V. S. Smirnov, Doctoral Dissertation in Physics and Mathematics (Tomsk, 1983).

9. V. M. Entin, I. I. Ryabtsev, A. E. Boguslavsky, and Yu. V. Brzhazovsky, Opt. Commun. **207**, 201 (2002).

Translated by V. Sipachev

Heterolaser Frequency Tuning
under the Action of Ultrasonic Waves

L. A. Kulakova* and I. S. Tarasov

Ioffe Physicotechnical Institute, Russian Academy of Sciences, St. Petersburg, 194021 Russia
*e-mail: L.Kulakova@mail.ioffe.ru
Received June 9, 2003

A new principle of the diode laser frequency tuning has been developed and implemented. According to this, the laser frequency is tuned by alternating strain in the active region of an InGaAsP/InP laser heterostructure emitting in a wavelength range of 1.3–1.8 μm. The strain is induced through the excitation of bulk ultrasonic waves in these heterostructures by means of a specially developed technique. Data on the influence of the alternating strain, induced by the bulk ultrasonic waves, on the spectral characteristics of laser radiation are presented. Estimates based on these data show that the frequency tuning range amounts to $\Delta F \approx 110$ GHz for an acoustic wave with the frequency $f = 6.5$ MHz and a power of about 1 W. © *2003 MAIK "Nauka/Interperiodica".*

PACS numbers: 42.60.Fc; 78.20.Hp

The processes determining the spectral characteristics of heterolasers have been extensively studied. Of most interest are the investigations devoted to studying the possibilities to control the laser radiation frequency. A simple and reliable method is offered by the wavelength tuning through variation of the pumping current in multistage lasers [1]. Frequency tuning in diode lasers for high-resolution laser spectrometers is usually achieved by using thermal effects [2] or by varying the working current [3].

It is known that elastic strain modifies the deformation potential, thus affecting the electron subsystem (in particular, the bandgap width [4]) and changing the dielectric permittivity [5] of semiconductors. We may expect that the strain-induced variation of the bandgap width will modify the generation conditions in laser heterostructures, which has to be manifested in a change of the spectral characteristics of radiation, in particular, the radiation frequency. A change in the refractive index of the laser resonator in the presence of strain will also modify the radiation spectrum.

This paper presents the first results of our investigation of the straining action of bulk ultrasonic waves on the InGaAsP/InP laser heterostructures and the related changes in the radiation characteristics.

EXPERIMENTAL

We have studied InGaAsP/InP laser heterostructures of separate confinement with two strained quantum wells (Fig. 1). The heterostructures were grown by metalorganic vapor phase epitaxy (MOVPE) on *n*-InP substrates. Neither the active region nor the waveguide layers were intentionally doped. The doping profile of the wide-bandgap emitters and the contact layer is presented in Fig. 1. The MOVPE-grown heterostructures were coated with insulating SiO$_2$ layers, in which 100-μm-wide mesastrips were formed by photolithography. Then, SiO$_2$ mirrors (with a reflection coefficient of $R > 0.95$) and antireflecting layers ($R < 0.04$) were deposited onto the resonator edges. Finally, the laser diodes were fixed on copper heat exchangers with the aid of indium-based solder.
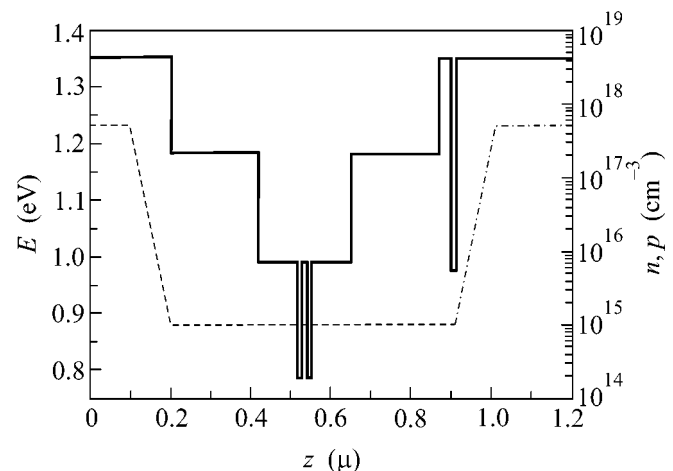

Fig. 1. A schematic energy band diagram of InGaAsP/InP laser heterostructures of separate confinement (KR-1168 type emitting at $\lambda = 1.58$ μm (solid curve). Dash and dot–dash curves show the calculated doping profile for silicon (donor) and zinc (acceptor), respectively (z is the structure growth coordinate).
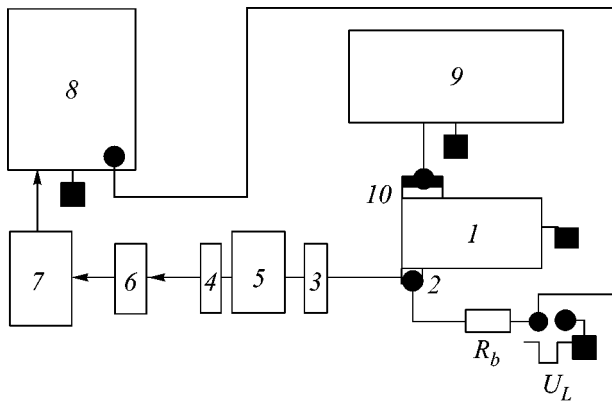
Fig. 2. A schematic diagram of the experimental setup: (*1*) metal substrate; (*2*) laser heterostructure; (*3*, *4*) focusing lenses; (*5*) Fabry–Perot etalon; (*6*) photodiode; (*7*) amplifier; (*8*) oscillograph; (*9*) microwave oscillator; (*10*) piezoelectric ceramic transducer.
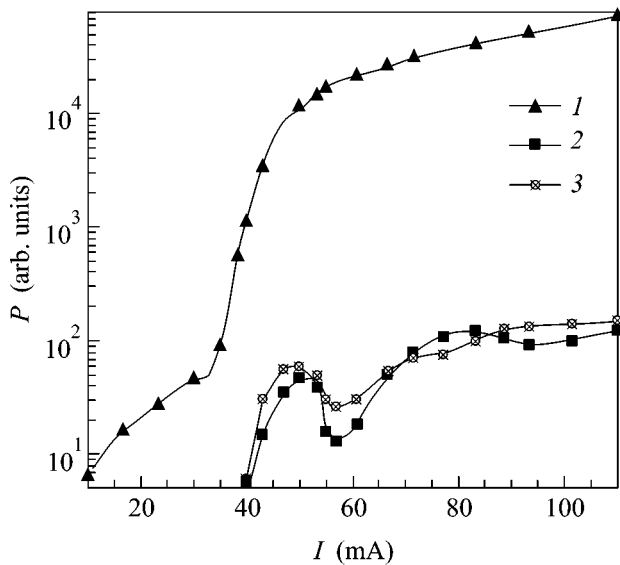

Fig. 3. Plots of the photodiode response signal intensity versus working current of a laser diode: (*1*) direct detection; (*2*) dispersion curve at the FPE output; (*3*) FPE output signal in the presence of an ultrasonic wave ($f = 6.5$ MHz).

The experiments were performed with laser heterostructures operating at room temperature in the pulsed regime with a pulse duration up to 3 μs at a wavelength of 1.48 μm. The threshold current was ~35 mA; the working current was varied from this threshold up to three times this value. The radiation spectrum halfwidth was 0.25–0.4 nm.

The investigation was conducted using a specially designed experimental setup, schematically depicted in Fig. 2. A collimated and focused beam of laser radiation was detected by fast-response photodiodes with different photocurrent buildup times τ_d (5 or 60 ns) using one

of the two schemes. In the first case, the focused radiation beam was directly detected by a photodiode. In the second case, the collimated beam was passed through a Fabry–Perot etalon (FPE) and then focused and detected by a photodiode in the focal plane. This scheme employed an optical etalon with deposited metal mirrors and an 0.6-mm-wide air gap. According to calculations, the dynamic dispersion range of this etalon at a wavelength of 1.48 μm was 18.25 Å. Measurements using the FPE scheme allow changes in the spectral characteristics of laser radiation to be analyzed.

The output signal of a photodiode was amplified by an amplifier with a bandwidth of up to 5 MHz and was displayed on a wideband (100 MHz) oscillograph. The signal modulated with a frequency of the ultrasound was measured using an amplifier with a bandwidth of 400 MHz.

In order to study the effect of elastic straining on the laser generation regime and the radiation characteristics, we have developed a method of exciting bulk acoustic waves in laser heterostructures in a frequency range from 6.5 to 200 MHz. The bulk longitudinal ultrasonic waves with an intensity of up to 100 W/cm^2 were excited using piezoelectric ceramic resonator plates in a frequency interval of 6.5–10 MHz (Fig. 2).

RESULTS AND DISCUSSION

Investigation of the laser radiation intensity as a function of the working current gave the following results (Fig. 3). Direct detection of the radiation (curve *1*) showed a normal threshold character of the process, with a slower monotonic increase in the intensity at a current above the threshold (the working current was varied from this threshold up to a threefold value). Measurements using the FPE scheme revealed oscillating variation of the signal level with the working current (curve *2*). Since the FPE transmission depends on the signal frequency, this signal behavior is evidence that variation of the working current is accompanied by a change in the laser radiation frequency. Indeed, independent spectroscopic measurements of the laser radiation wavelength in the regime of variable working current revealed a shift of the laser emission line (Fig. 4). Thus, the position of the laser frequency on the dispersion curve of the FPE transmission can be controlled by varying the working current.

The effect of the acoustic-wave-induced straining was studied in two experimental configurations. The first configuration, employing a photodiode detector with a relatively slow response ($\tau_d \approx 60$ ns) and an amplifier with a relatively narrow bandwidth (~5 MHz), ensured increased dynamic range and was used for "rough" measurements. The second configuration with a fast-response photodiode ($\tau_d \approx 5$ ns) and a wideband amplifier (~400 MHz) revealed a frequency-

modulated component related to the ultrasound-induced straining.

In the first configuration, ultrasonic excitation of the laser heterostructure led to the following effects. In the regime of minimum transmission, the ultrasonic wave caused an increase in the FPE transmission, whereby the photodiode response increased by a factor of 1.5–2 (Fig. 3, curve *3*). At the maximum of the dispersion curve, the ultrasound produced a reverse effect and decreased the FPE transmission. Both these effects possessed an integral character: the signal increment was virtually constant during the laser pulse ($\tau_L = 2.5$–3 μs) and the acoustic pulse.

Let us qualitatively analyze the obtained results. An elastic wave is essentially an alternating strain. If strains with opposite signs lead to corresponding shifts of the light frequency ($\pm\Delta F$) or changes in the emission direction, introduction of an acoustic wave in the regime of minimum FPE transmission would drive the system away from the minimum and, hence, increase the transmission. By the same token, the system occurring at the maximum of the dispersion curve will exhibit the reverse effect, whereby a change in the emission frequency or direction under the action of an acoustic wave will cause a decrease in the FPE transmission—in agreement with what was observed in experiment.

Thus, the observed effects may result from changes in both frequency and direction of the heterolaser emission. However, we have established that the latter factor is insignificant. Taking into account that the acoustic wavelength in our experiments was about 400 μm and the optical resonator aperture in the wave propagation direction was about 1 μm, it can be readily shown that the laser beam deviations caused by the refractive index gradient do not exceed 20″, which is beyond the sensitivity limits of our experimental setup. This conclusion is experimentally confirmed by the fact that the position of the signal maximum in the focal plane of the lens was the same for the acoustic generator switched on and off. As for the first factor (frequency shift), the possible mechanisms can be related to changes in both electron parameters of the heterostructure and the optical properties of the laser resonator. Determination of the absolute and relative magnitudes of these contributions requires further experimental and theoretical investigations.

Using the dispersion curve of the etalon transmission (Fig. 3, curve *2*) and the experimental data on variations of the laser radiation intensity (Fig. 3, curve *3*) in response to the acoustic wave introduction ($f = 6.5$ MHz), we have estimated the change in the laser wavelength $\Delta\lambda$ under the action of bulk ultrasonic waves. For an acoustic power of ~1 W (at an intensity of ~100 W/cm^2), $\Delta\lambda/2 \approx 3.5$–$4$ Å per half period (or 7–8 Å per period), which corresponds to a frequency shift of $\Delta F \approx 110$ GHz.
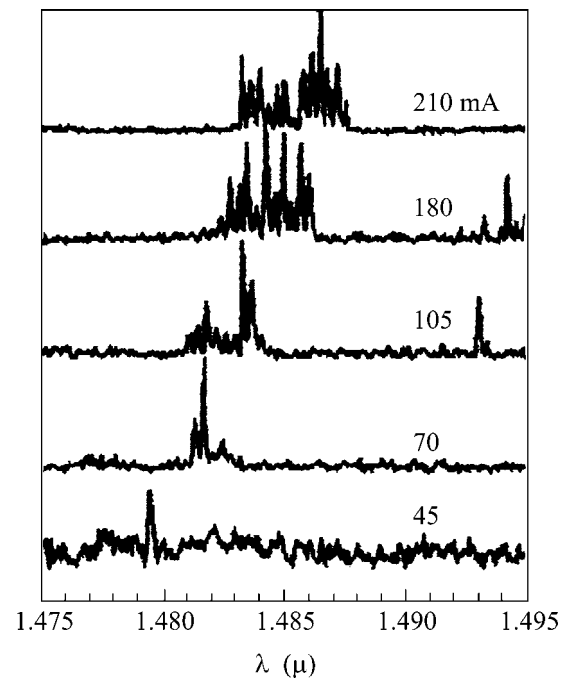

Fig. 4. Heterolaser spectra measured for various working currents.

As was noted above, the optical signal increment was virtually constant during the laser pulse and the acoustic pulse, although we might expect the FPE transmission to be modulated by the ultrasound frequency. We believe that the main possible factors which could explain the observed behavior are (i) unsatisfactory frequency characteristics of the detection channel and (ii) too large a radiative recombination time (T_L) of the laser heterostructure as compared to the acoustic wave period T_s. However, the latter reason is invalid, since both published data and our measurements show that $\tau_L \ll T_s$.

In order to visualize the anticipated modulation of the laser radiation frequency by the ultrasonic wave, we have performed fine measurements in the aforementioned configuration with reduced dynamic range and improved frequency characteristics of the detection channel. The results of these measurements are presented by oscillograms in Fig. 5. The upper sweep represents the working current pulse. The lower sweep shows laser radiation pulses measured for a working current amplitude slightly above the threshold ($I_1 \approx 1.4 I_{th}$). In the absence of the acoustic wave, the radiation pulse has a nearly rectangular shape (Fig. 5a) to within a pulse top ringing caused by thermal fluctuations of the FPE tuning. Switching on the ultrasound (Fig. 5b) leads to an almost 100% modulation of the laser pulse amplitude with a frequency equal to that of the acoustic wave. An increase in the ultrasound frequency leads to a corresponding decrease in the modulation period (Fig. 5c). Obviously, the observed output
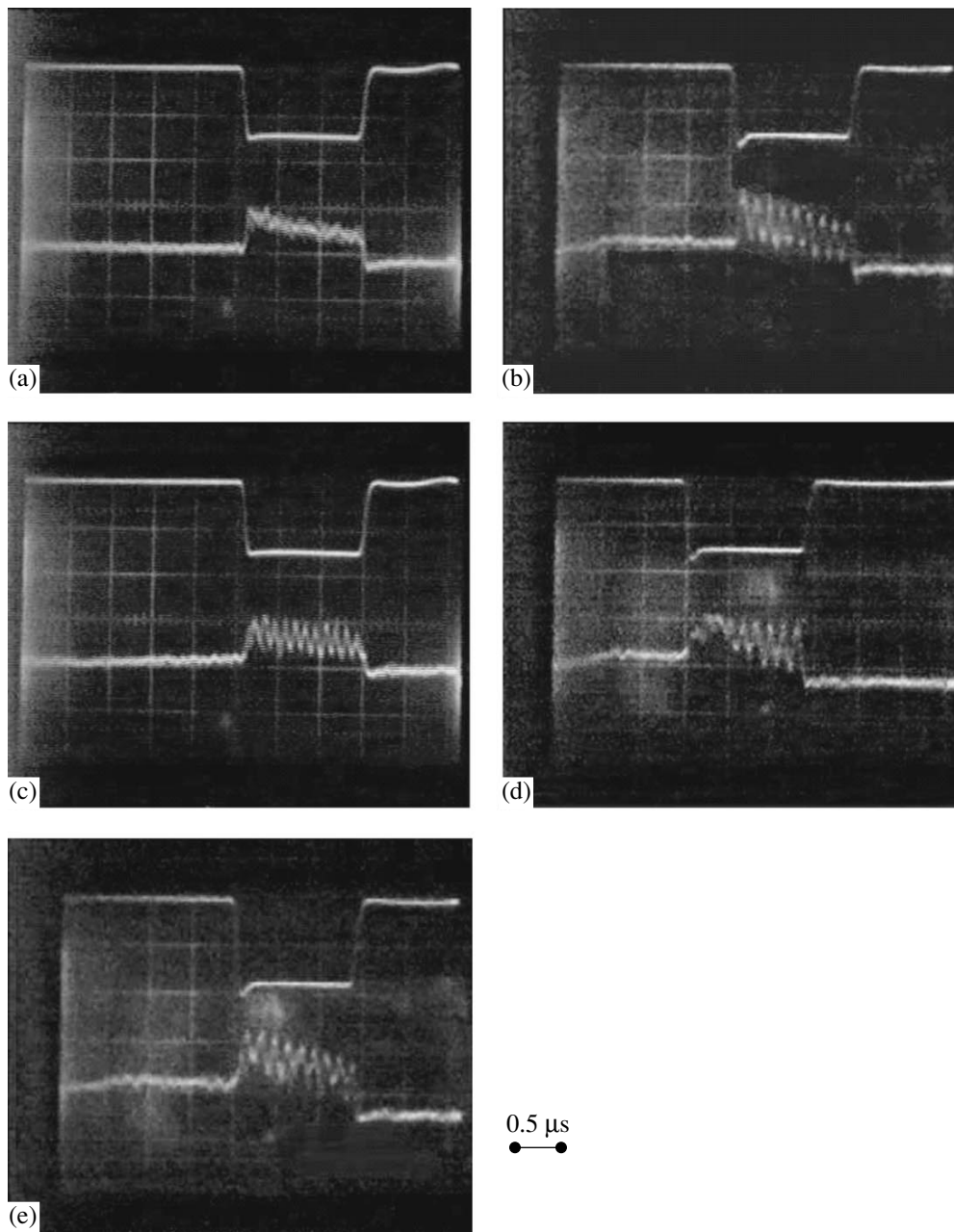
Fig. 5. Oscillograms showing the working current pulse (top, 33 mA/div) and the laser radiation pulses (bottom) measured with the acoustic wave (a) switched off and (b–e) switched on, for the ultrasound frequency $f = 6.5$ (b, d, e) and 8 MHz (c).

signal modulation reflects changes in the FPE transmission in response to the frequency modulation of the transmitted laser radiation. The ultrasound pulse coincides with the working current pulse. On decreasing the current pulse delay, which leads to a partial overlap of these pulses, we observe the corresponding partial modulation of the laser pulse (Fig. 5d).

As was noted above, an increase in the working current is accompanied by a growth of the laser linewidth (Fig. 4). In our opinion, this circumstance, together with thermal fluctuations of the FPE tuning, accounts

for a decrease in the stability of modulation of the FPE transmission observed upon an increase in the working current (Fig. 5e). This implies that laser structures with a narrower linewidth should be used in order to observe the modulation effects in a wider range of working currents.

To summarize, we have developed and implemented a new method for the investigation of laser radiation characteristics, with which one can study optical processes with a characteristic variation time as small as 5 ns. We have also developed a special technique for

exciting bulk acoustic waves in laser heterostructures in a frequency range from 6.5 to 200 MHz. Using this technique, InGaAsP/InP laser heterostructures were excited by ultrasound in a frequency range from 6.5 to 10 MHz.

We have studied changes in the laser radiation characteristics under the action of alternating strain induced by bulk ultrasonic waves with an intensity of up to 100 W/cm^2. It is unambiguously established that an ultrasonic wave introduced into a laser heterostructure produces modulation of the laser frequency with a period equal to that of the acoustic wave. Estimates based on the experimental data show that the change in the radiation wavelength amounts to $\Delta\lambda \approx 7$–8 Å, which corresponds to a frequency tuning range of $\Delta F \approx$ 110 GHz.

The authors are grateful to I.A. Andreev for kindly providing a fast-response photodiode (λ = 1.15–2.3 μm), to A.V. Lyutetskii for providing laser diodes for the experiments, and to A.M. D'yakonov for useful methodological discussions.

REFERENCES

1. H. Hillmer, A. Grabmaier, S. Hansmann, *et al.*, IEEE J. Sel. Top. Quantum Electron. **1**, 356 (1995); N. A. Pikhtin, A. Yu. Leshko, A. V. Lyutetskiĭ, *et al.*, Pis'ma Zh. Tekh. Fiz. **23** (6), 10 (1997) [Tech. Phys. Lett. **23**, 214 (1997)].

2. L. A. Kulakova, B. A. Matveev, and B. T. Melekh, J. Non-Cryst. Solids **266–269**, 969 (2000).

3. A. N. Imenkov, N. M. Kolchanova, P. Kubat, *et al.*, Fiz. Tekh. Poluprovodn. (St. Petersburg) **35**, 375 (2001) [Semiconductors **35**, 360 (2001)].

4. Yu. V. Ilisavskiĭ and L. A. Kulakova, Fiz. Tverd. Tela (Leningrad) **23**, 3299 (1981) [Sov. Phys. Solid State **23**, 1916 (1981)].

5. N. S. Averkiev, Yu. V. Ilisavskiĭ, and L. A. Kulakova, Fiz. Tverd. Tela (St. Petersburg) **38**, 3556 (1996) [Phys. Solid State **38**, 1938 (1996)].

Translated by P. Pozdeev

Effect of Hydrostatic Pressure on the Superconductivity in Fluorinated $Hg_{0.8}Ba_2Ca_2Cu_{3.2}O_{8+\delta}$

E. S. Itskevich and I. V. Morozov

Institute of High-Pressure Physics, Russian Academy of Sciences, Troitsk, Moscow region, 142190 Russia
Received June 19, 2003

The effect of hydrostatic pressure on the superconducting transition temperature was measured for the Hg-1223 phase of a fluorinated mercury cuprate high-temperature superconductor with $T_{c(optim)} = 138$ K. The value of the T_c derivative with respect to pressure was found to be rather high (11.0 K/GPa); at $P = 1.5$ GPa, $T_c = 153.5$ K. The results obtained are discussed in connection with works on the synthesis of such samples. © *2003 MAIK "Nauka/Interperiodica"*.

PACS numbers: 74.62.Fj

The members of the homologous series of layered mercury cuprate high-temperature superconductors (HTSCs) have the highest T_c due to the nonstoichiometric oxygen in the Hg–O layers, providing the necessary concentration of charge carriers in the Cu–O layers. The length of the Cu–O bond in the layer (parameter **a**) is very sensitive to the nonstoichiometric oxygen content. Mercury HTSCs have layers with minor distortions (Cu–O bond angle is close to 180°).

The temperature T_c (here and below, we take the maximum value of T_c for a particular member of the series for which the value of δ is an optimum) depends on the number **n** of layers. The highest $T_c = 135$ K is attained for **n** = 3.

Interest in fluorinated cuprates was aroused in connection with the work [1], in which it was shown that their T_c is 3–4 K higher than in oxide cuprates and their lattice parameters were studied in detail. The valence of fluorine is lower than that of oxygen, so that a greater amount of fluorine should be introduced to attain the same carrier concentration. In addition, there is a slight difference in the radii. These factors lead to a change in the length of the apical bond Cu–O upon fluorination of the Hg-1201 phase but have no effect on T_c and on the length of the Cu–O bond in the layer [2]. The fluorination of the 1223 phase, which has a high anion concentration, reduces the Cu–O bond length without changing the bond angle and increases T_c by approximately 4 K [1], which shows that the increase in T_c is correlated with the decrease in the Cu–O bond length in the layer.

The dependences $T_c(\mathbf{a})$ for fluorinated and oxide Hg-1223 samples were also studied in [1]. The difference between the dependences is clear: for the oxide Hg-1223 sample there is a pronounced peak with $T_{c(optim)} = 134–135$ K; for the fluorinated sample, the peak is less pronounced, and the corresponding parameter **a** is smaller. Compression shortens the Cu–O bond:

$\Delta\mathbf{a} = 0.0023$ Å corresponds to an increase in T_c ($\Delta T = 4$ K). It is noted that the stresses occurring in the CuO_2 layer are due to the chemical modification of the crystal structure, i.e., to fluorination.

Pressure, as an additional way of changing the parameter **a**, extends the capabilities for the investigation of mercury cuprates. In particular, $T_c = 160$ K was attained for the Hg-1223 phase under quasi-hydrostatic compression up to 30 GPa [3]. The members of the homologous series with **n** from 1 to 5 were studied under hydrostatic pressure. The optimal (i.e., providing optimal **a**) T_c varied with the derivative dT_c/dP from 2 to 4 K/GPa; for the 1223 phase $dT_c/dP = 4.0$ K/GPa. These works are reviewed in [4]. The effect of pressure on T_c is smaller than the effect of doping because compression is accompanied with a decrease in the Cu–O bond angle.

The parameters of fluorinated Hg-1223 samples should be sensitive to pressure, as is the case with oxide cuprates.

We measured the effect of high hydrostatic pressure (up to 1.5 GPa) on the critical temperature T_c for the fluorinated mercury cuprate $Hg_{0.8}Ba_2Ca_2Cu_{3.2}O_{8+\delta}$. An unexpectedly rapid increase in the temperature T_c was observed (from $T_c = 138$ K at $P = 0$ to $T_c = 153.5$ K at $P = 1.5$ GPa).

1. EXPERIMENT

Ceramic samples were synthesized in the laboratory of E.V. Antipov at the Chemical Faculty, Moscow State University. The best fluorinated sample had the following lattice parameters: **a** = 3.8501 Å, **c** = 15.773 Å (see [1]). These parameters are smaller than in the initial oxide structure Hg-1223 of the same crystal structure with $T_c = 134$ K, **a** = 3.8524 Å, and **c** = 15.819 Å. The processes of synthesis and measurement of the crystal

structure parameters and the superconducting transition temperature are described in detail in [1].

The magnetic susceptibility was measured under hydrostatic pressure using a pair of coils wound on the same fluoroplastic form mounted on the obturator of a low-temperature high hydrostatic pressure chamber (HPC). The sample was placed in the receiving coil. A modulation coil (modulation frequency, 2000 Hz) was wound on the form with coils, and a manganin pressure gage also used as a heater was placed above it.

A mixture of 40% pentane and 60% dry transformer oil was used as a pressure transmission medium. The pressure was determined from the resistance of the manganin pressure gage.

Two methods were used for measuring T_c. The first method used the manganin heater to increase the HPC temperature. The manganin heater made it possible to vary the heating rate. To reach a temperature below 100 K, the HPC was immersed in liquid nitrogen. Then, the HPC was lifted above the level of liquid nitrogen, and heating began. The temperature was measured with a (Cu + 0.1% Fe)–Cu thermocouple with the junction glued to the sample inside the receiving coil. The dependence $T_c(P)$ was measured at pressures up to 1.4 GPa. The pressure coefficient (PC) was found to be very high. However, the corresponding values of T_c at $P = 0$ were underestimated. In our opinion, this can be explained by a possible temperature gradient in the working cavity of the HPC filled with a dielectric medium for pressure transmission.

Measurements by another method, which does not use the manganin heater, were performed to avoid errors. The HPC was cooled to liquid nitrogen temperature and heated up to room temperature at a constant rate through the walls of an inner soft helium Dewar vessel placed in an outer rigid nitrogen Dewar vessel. The temperature of the sample was measured with a copper–constantan thermocouple with the hot junction soft-soldered to the HPC to improve the thermal contact. In the temperature range under consideration, the HPC had good thermostatic properties, because it was made of beryllium bronze including copper as its main component. Measurements gave the correct value $T_c(0) = 138$ K at $P = 0$; the obtained value of the PC was virtually equal to that measured in the preceding experiment.

The obtained experimental data are shown in Fig. 1. To correct the values of $T_{c(optim)}$ measured by the first method (internal heating), they are increased by the difference in the values of T_c at $P = 0$ measured by the two methods.

At $P = 1.5$ GPa, $T_c = 153.5 + 1.2$ K. Although the superconducting transition was rather wide, ΔT could be measured from the shift of the parallel segments of the curves. Upon fluorination, the PC (dT_c/dP) was $11.0 + 0.5$ K/GPa, i.e., almost three times greater than
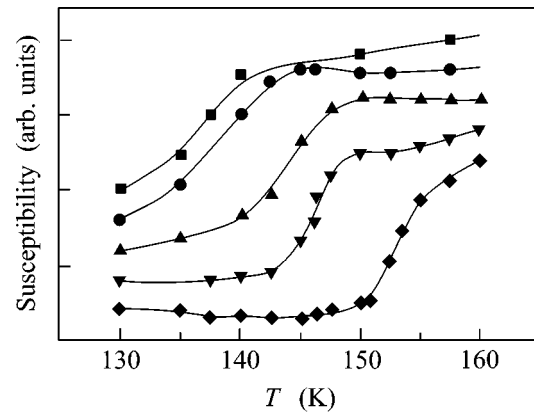
Fig. 1. Magnetic susceptibility of a fluorinated Hg-1223 sample under high hydrostatic pressure; the values of T_c for calculating dT_c/dP were determined from the maximal rate of variation of the signal $\chi(P)$: ■, 0.15; ●, 0.42; ▲, 0.85; ▼, 0.91; and ◆, 1.5 GPa.
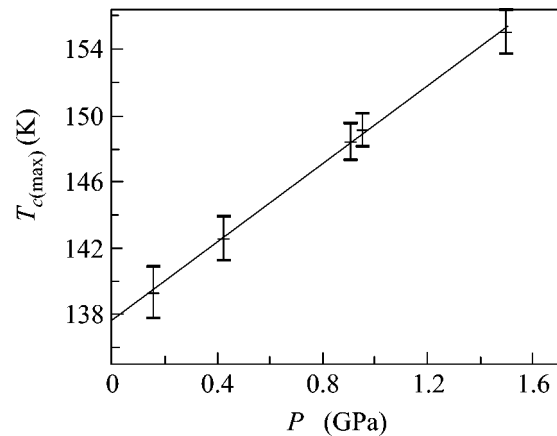

Fig. 2. Pressure dependence of the superconducting transition temperature $T_{c(max)}$ for Hg-1223 + F.

upon oxidation [4]. The dependence $T_c(P)$ is shown in Fig. 2.

2. DISCUSSION

According to [1], upon fluorination, the compression of the CuO_2 layer without its bending results in a considerable increase in T_c due to chemical compression, although the compressibility proper is low ($\Delta \mathbf{a} = 0.0023$ Å). The increase in T_c with decreasing $\mathbf{a}$ is found to be linear for the series Hg-1201–Hg-1223 + F, $dT_c/dP = -1.35 \times 10^3$ K/Å. The layer bending angle remains small and virtually invariant (177°–178°). External pressure has a far greater effect on the bending angle (175° at $P = 2$ GPa [1]). It is also noted in [1] that a change in the anion composition leads to compression of the Hg–O layer, as does external pressure. We

believe that this can result in an additional increase in T_c. It is significant that fluorination does not lead to a considerable change in the structural environment of the CuO$_2$ layer [1].

Using the data reported in [1, 4], the results of our experiments, and the data on the relationship between **a** and P [5], we found that $dT_c/d\mathbf{a}$ for the fluorinated 1223 phase is equal to -0.92×10^3 K/A. This result shows that the chemical compression efficiency in fluorinated Hg-1223 is slightly increased.

In our opinion, the effect of pressure on the CuO$_2$ layer bending, the apical distance Cu–O, and the Hg–O layer in the complex system under consideration can be indicative of the existence of several mechanisms of the pressure effect. Different mechanisms can be responsible for the sharp increase in $T_{c\,\mathrm{max}}(\mathbf{a})$ upon fluorination and the decrease in $T_c(\mathbf{a})$ upon super- and suboxidation observed in all the members of the homologous series of mercury cuprates, as well as for the sharp increase in the derivative dT_c/dP upon fluorination.

The conclusion made in [1] that the chemical modification of the structure upon fluorination of the Hg-1223 phase is the major factor leading to the increase in $T_{c(\mathrm{optim})}$ seems to be convincing. However, the questions concerning the considerable (almost 5-fold) difference in the relative changes in the lattice parameters (anisotropy) of fluorinated and oxidized samples remain open. There is also no quantitative explanation for the increase in T_c of the Hg-1223 phase from 134–135 to 138 K.

The main conclusion from the experimental data obtained is that the anomalously high value of dT_c/dP for the maximum T_c of the Hg-1223 phase upon fluorination and the increase in T_c are indicative of a considerable effect of fluorine introduced into the phase $Hg_{0.8}Ba_2Ca_2Cu_{3.2}O_{8+\delta}$.

REFERENCES

1. E. V. Antipov, A. M. Abakumov, K. A. Lokshin, *et al.*, Physica C (Amsterdam) **141–148**, 579 (2000); K. A. Lokshin, D. A. Pavlov, and S. N. Putilin, Phys. Rev. B **63**, 064511 (2001).

2. A. M. Abakumov, V. I. Aksenov, V. A. Aleyshin, *et al.*, Phys. Rev. Lett. **80**, 385 (1998).

3. V. V. Struzhkin, Yu. A. Timofeev, R. T. Downs, *et al.*, in *Proceedings of Joint XV AIRAPT and XXXIII EHPRG International Conference, Warsaw, Poland* (1995).

4. E. S. Itskevich, Low Temp. Phys. **25**, 509 (1999).

5. A. R. Armstrong, W. I. F. David, I. Gameson, *et al.*, Phys. Rev. B **52**, 15551 (1995).

Translated by K. Chamorovskiǐ

Phonon Autoecho in Bismuth and Antimony Single Crystals

O. V. Misochko*, M. Hase**, and M. Kitajima**

* Institute of Solid-State Physics, Russian Academy of Sciences, Chernogolovka, Moscow region, 142432 Russia
e-mail: misochko@issp.ac.ru
** National Institute for Materials Science, 305-0047, Tsukuba, Japan
Received June 20, 2003

Phonon autoecho is observed upon pumping Bi and Sb semimetals with ultrashort high-energy laser pulses. The autoecho is manifested as a revival of reflection oscillations generated by an A_{1g} coherent phonon after their complete disappearance. The phenomenon of phonon autoecho offers decisive evidence of the nonclassical character of the state of the crystal lattice that is accomplished in pumping–probing experiments by femtosecond laser pulses. © *2003 MAIK "Nauka/Interperiodica"*.

PACS numbers: 79.20.Ds; 63.20.-e; 78.47.+p

In the last decade, great interest has been shown in studying the response of condensed media to the action of an ultrashort laser pulse, in which energy is concentrated in a small time, space, and spectral range. This is in many ways due to the success of laser technology, which allowed the laser pulse duration to be reduced down to the subpicosecond range and thus opened the way of studying lattice dynamics in real time. The access to ultrafast lattice dynamics was provided by the observation of coherent phonons that appear as oscillations of light reflection (or transmission) after exposure of the crystal to an ultrashort laser pulse [1]. The attainment of a stable phase, which serves as the basis for calling phonons coherent, is possible because the duration of the exciting pulse Δt is shorter than the inverse frequency of the phonon mode Ω^{-1}, $\Delta t < \Omega^{-1}$. The oscillation period of coherent phonons, as a rule, coincides with the inverse frequency of Raman active phonons of the medium, which allows the mechanism of their generation to be associated with the phenomenon of stimulated Raman scattering [1, 2]. The majority of experiments of the pump–probe type were carried out with the use of low-energy pulses, so that the variation of reflection did not exceed 10^{-4}–10^{-5}. However, in recent years, the trend has been toward studying the photoinduced response using high-energy pulses [3–5]. These experiments revealed an interesting feature of oscillations: as the energy density of the exciting pulse increases, the oscillation amplitude increases nonlinearly, manifesting a tendency toward saturation, whereas the decay time sharply decreases. Attempts at explaining this feature within the framework of the model of energy relaxation in a classical oscillator have not been successful [6]. In order to reveal the processes that are responsible for the decay of oscillations and thus elucidate the nature of the coherent phonon, we carried out time-resolved investigations with the use of high-energy

pulses, exciting coherent phonons at low (helium) temperatures.

The measurements of relaxation lattice dynamics were carried out with the use of high-energy laser pulses. To do this, the radiation of a Ti : sapphire laser ($\lambda = 800$ nm) was converted by a regenerative solid-state amplifier, at whose output the energy of pulses was equal to 5 nJ, their duration was 150 fs, and their repetition frequency was 100 kHz. The polarizations of the exciting and probing pulses were orthogonal, and the optical response was studied for the plane perpendicular to the trigonal axis of Bi and Sb single crystals. The crystals were placed in an optical helium cryostat, which allowed measurements to be performed at a temperature of 10 K. The ratio between the intensities of the exciting and probing laser pulses was maintained equal to 10 : 1. The exciting and probing laser beams were focused on the sample surface with a lens with a focal length of 10 cm. The excitation channel was modulated with an optical chopper with a frequency of 2 kHz, and detection was performed using synchronous detection of signals measured by photodiodes. In the experiment, the normalized differential reflection of the excited and nonexcited crystal

$$\frac{\Delta R}{R_0} = \frac{R(t) - R_0(t < 0)}{R_0(t < 0)} \qquad (1)$$

was measured as a function of the time interval t between pumping and probing.

A typical optical response observed upon excitation followed by probing of the bismuth single crystal with femtosecond pulses of different energies is shown in Fig. 1. The difference in the energy density at which the oscillations shown in the upper and lower panels of Fig. 1 were obtained comprises three orders of magnitude. In both cases, the excited electronic state of the system relaxes to an equilibrium state for times of the
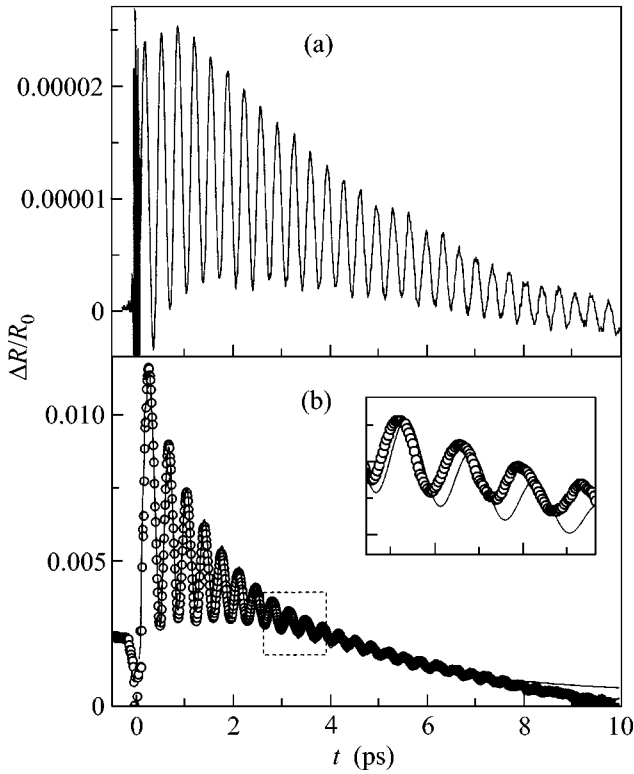
Fig. 1. Time-resolved normalized differential reflection $\Delta R/R_0$ of a Bi single crystal obtained at room temperature and a laser-pulse energy density of (a) 0.5 $\mu J/cm^2$ and (b) 5 mJ/cm^2. The inset displays magnified oscillations at longer time delays and the results of fitting with the use of Eq. (2).

order of picoseconds and fast oscillations induced by a coherent phonon are imposed on this electronic relaxation [1–4]. The distinctions are the magnitude of the photoinduced signal and the ratio between the oscillating and nonoscillating components of the signal. Moreover, the oscillation frequency, which does not depend on the pumping pulse energy in the case of low-energy pulses and coincides with the frequency of thermal phonons observed by spontaneous Raman light scattering, depends on the pulse energy density in the case of intense pumping [4, 5]. The oscillation frequency shift toward the red spectral region with increasing excitation energy was connected with the anharmonicity of the potential, which increases with increasing oscillation amplitude [5].

An attempt at fitting the relaxation response with the function

$$\Delta R/R_0 = A_e \exp(-t/\tau_e)$$
$$+ A_p \exp(-t/\tau_p)\sin(\Omega t - \varphi) \tag{2}$$

leads to a satisfactory result only in the case of low-energy pulses. For high-energy pulses, this function works well only for short delay times, whereas the fitting function and experimental data do not coincide for

longer times (see the inset in Fig. 1b). This indicates that the frequency varies with time, which can be approximated in the first approximation by a linear chirp $\Omega = \Omega_0 + \alpha t$. The phonons whose instant frequency is a function of time can be appropriately called chirped. The asymmetry of the phonon line in the Fourier transformed signal, see Fig. 2, can be considered a manifestation of the chirp. An analysis of the Fourier transformed signals performed for short and long delay times indicates that the decay of oscillations is nonexponential (the half-width of the phonon peak is a function of the delay time). This is evidence of the non-Markovian character of the process, in which the phase "memory" plays an important part.

Whereas a decrease in temperature in the case of low-intensity pulses leads to an insignificant change in the oscillation frequency, which approximately coincides with the frequency shift of thermal phonons measured with the use of spontaneous Raman light scattering [7], the character of the relaxation response changes radically in the case of high-intensity pulses. Because we are interested only in crystal lattice dynamics, it is appropriate to eliminate the nonoscillating electronic response, for which it is sufficient to differentiate the signal. It is evident in Fig. 3 that oscillations at low temperatures initially die out, reaching a certain minimum magnitude, which we will subsequently call oscillation collapse. However, after the collapse, whose occurrence time depends on the energy density of the exciting pulse, the oscillations demonstrate a revival. The phenomenon of oscillation collapse and revival is manifested as phonon autoecho [8]. This name is justified by the fact that a comparison of the oscillation phases before and after the collapse points to their shift by π. In the terminology of Averbukh and Perel'man [9], the observed revival is a fractional revival of the order of 1/2 and represents the oscillation decay process reversed in time up to the instant of collapse. The difference of the phonon autoecho from the photon or spin echo should be specially emphasized [10]. In the latter phenomena, echo is induced by the second pulse, whose role is reduced to the excitation of oscillations in an anharmonic potential whose phases are developed in time in the opposite direction.

A comparison of the Fourier transformed signals for times before and after the collapse indicates that the totally symmetric phonon makes the major contribution to oscillations. Nevertheless, the frequency of this phonon is shifted toward the red spectral region for short delay times, and its chirp is proportional to the phonon line asymmetry and is larger for short delay times than for longer times. It should also be noted that the collapse occurrence time is a sufficiently strong function of the laser pulse intensity; that is, for pulses of the same power differing in their duration, collapse occurs earlier at a shorter duration of the laser pulse. In order to obtain more comprehensive information on the phonon autoecho in semimetals, experiments similar to those described above were performed for an antimony
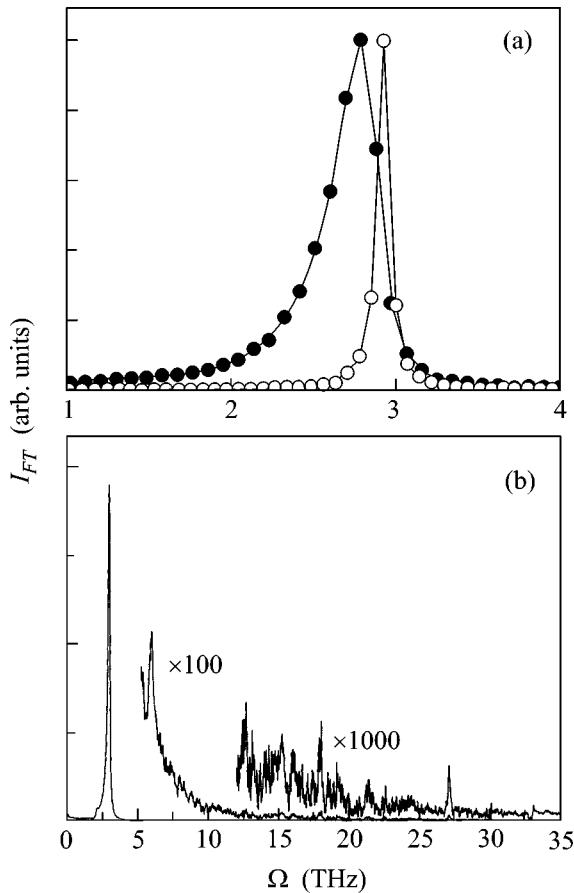
Fig. 2. (a) Normalized Fourier transforms of oscillations of a Bi single crystal for pulses with high (black symbols) and low (light symbols) energy densities. (b) Fourier transforms of oscillations of a Bi single crystal for pulses with high energy densities demonstrating the presence of higher harmonics.

Fig. 3. Reflection oscillations of a Bi single crystal at the temperature $T = 10$ K and a laser-pulse energy density of 9 mJ/cm^2.

single crystal. Because the condition of the effective excitation of coherent phonons ($2\Omega \geq \Delta t^{-1}$) is hardly fulfilled for the totally symmetric mode of Sb at the laser pulse duration used in this work ($\Delta t = 150$ fs), the amplitude of coherent oscillations turns out to be smaller than that for the case of Bi and the nonoscillating contribution dominates in the relaxation signal. Nevertheless, it follows from the data presented in Fig. 3 that oscillations are reliably detected at least for short times of the delay between pumping and probing. This is demonstrated by the fact that the Fourier transform shown in Fig. 4 contains a spectral peak at the frequency of the totally symmetric phonon. From the character of the signal at different delay times, it follows that phonon autoecho also occurs in the case of totally symmetric phonons of antimony.

The phenomenon of collapse and revival of oscillations is a purely quantum-mechanical effect, which has no classical analogue [8–11]. In fact, a classical oscillator described by the equations of Newtonian mechanics is unable to restore oscillations after attaining an equi-
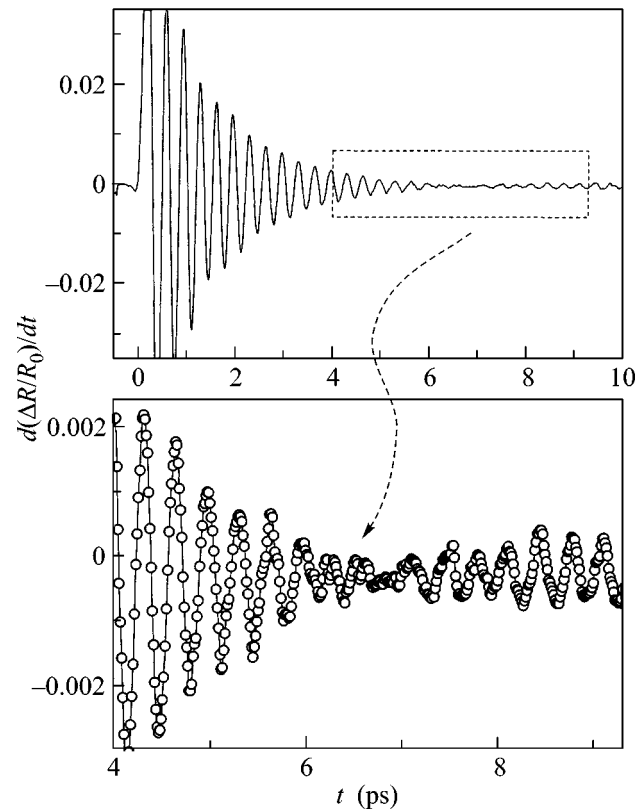
librium position. To date, the effect of collapse and revival has been observed for high-lying atomic electronic states, molecular vibrations, and atoms in a laser resonator, that is, for excitations of single-particle character [9]. Recently, the phenomenon of collapse and revival was observed for a Bose condensed gas of rearearth atoms [12]. An attempt at explaining the phenomenon of the collapse and revival of coherent phonons as beatings of two coupled classical oscillators cannot lead to success, because the major contribution in oscillations in our case is made by the single totally symmetric mode at the Γ point of the Brillouin zone [2].

The mechanism of the occurrence of phonon autoecho in semimetals can be described as follows. A pumping pulse by stimulated Raman light scattering excites phonons whose frequencies fall in the range limited by the spectral width of the laser pulse. Because the frequencies of phonons are different in the case of an anharmonic potential, their phases, being coincident (synchronized) at the instant of exposure to the pumping pulse, are randomized with time, which leads to the disappearance of the signal. However, because the system retains coherence (lattice oscillations continue), the phases become again coincident at a certain time interval, which is manifested as a revival of the signal or the appearance of phonon autoecho. Thus, it is evi-
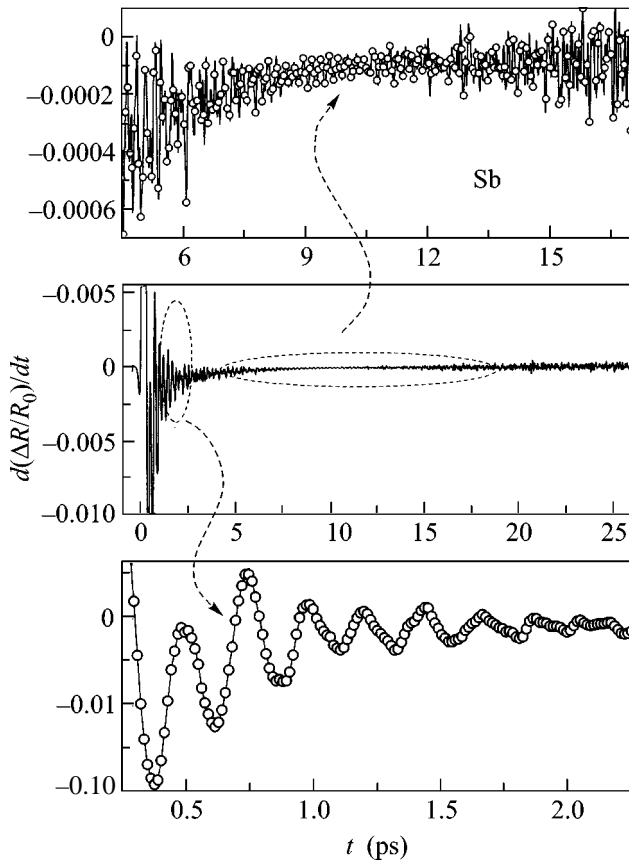
Fig. 4. Reflection oscillations of a Sb single crystal at the temperature $T = 10$ K and a laser-pulse energy density of 12 mJ/cm^2.
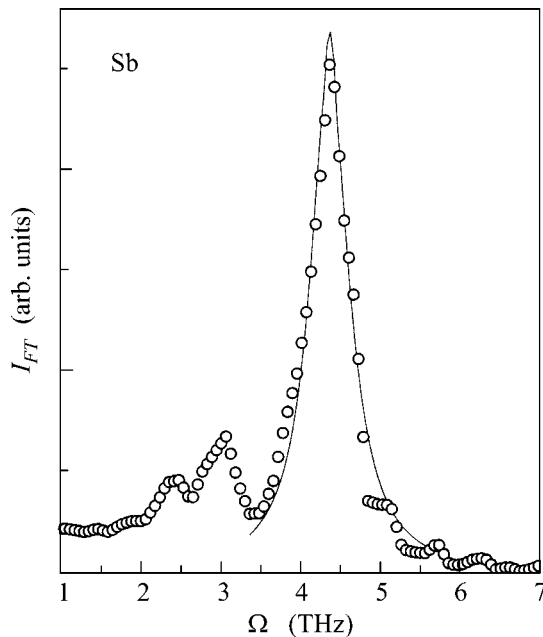

Fig. 5. Fourier transforms of the oscillations of a Sb single crystal shown in Fig. 4.

dent that oscillations occur because of light-induced lattice coherence (maintaining of certain phase ratios between various phonon states) rather than as a result of a change in the population of phonon modes. Correspondingly, the decay time of oscillations observed in a conventional experiment must be determined by the dephasing time of components of the wave packet formed by a superposition of stationary states rather than energy relaxation, which is irreversible. It is the absence of true irreversibility in the system with a discrete spectrum [9, 10] that leads to the restoration of the initial state after a lapse of time.

The generation of coherent phonons is determined by the nonlinear susceptibility of the crystal induced by the power pumping pulse. Under exposure to ultrashort light pulses, not only single-phonon states are excited, which leads to the fact that the lattice excitation by its nature represents a wave packet formed by a set of stationary states. Actually, the Fourier transformed response of the bismuth single crystal presented in Fig. 2 contains higher harmonics along with the classical (fundamental) frequency [13]. The wave packets (as well as coherent states) are at the boundary between the classical and quantum-mechanical description of the objects. Localization, the distinctive feature of a wave packet, is accomplished through a coherent superposition of many stationary states with large quantum numbers. In this case, a great number of states are required in order to select one maximum of the wave function by means of quantum interference, whereas large quantum numbers are required in order that the selected maximum have a small extension in space. Even though a wave packet demonstrates dynamic evolution similar to the evolution of a classical object, it nevertheless is a quantum object and, correspondingly, its behavior is much more complex. As was shown above, a wave packet in the case of an anharmonic potential can again become localized once it has been delocalized. Moreover, the extension of a wave packet in space and time can periodically depend on its location in the phase space, which occurs for so-called squeezed states, which are detected for semimetals [2, 14, 15]. All these features of the wave packet are conditioned by the discrete character of the spectrum and have no analogues in classical physics. The fact of phonon autoecho found in this work gives conclusive evidence that the state created by high-intensity femtosecond pulses cannot be described within the framework of Newtonian mechanics. Leaving for the future the elucidation of the particular class of nonclassical states to which the state obtained in semimetals by ultrashort laser pulses belongs, we note that this state likely obeys the criteria of Bose–Einstein condensation [16, 17]. Among these criteria are the coherence and the degenerate character of the ground state, the dependence of the collective mode frequency on the amplitude [11], the occurrence of the collapse and revival of oscillations of the condensate [11, 12], and off-diagonal long-range order.

It should specially be noted that the observation of phonon autoecho not only gives conclusive evidence of the quantum nature of the state created by ultrashort pulses but also allows us to understand why it was sufficient in the majority of cases to use a classical model for the description of coherent phonons. Actually, by virtue of the fact that the collapse of oscillations at low-energy laser pulses comes at times considerably longer than $\tau_c \approx 20$ ps, the "post-classical" evolution of the excitation of the lattice system occurs only for $t > \tau_c$ [9], that is, in the range of times in which the signal-to-noise ratio is too small to be measured. This is due to the fact that "post-classical" evolution is controlled by the oscillator anharmonicity $\tau_r = \dfrac{2}{\Omega}\left(h\left|\dfrac{\partial\Omega}{\partial E}\right|\right)^{-1}$ (E is the oscillator energy, and h is the Planck constant), which is too small in the case of low-energy pulses. According to the correspondence principle, the evolution of excitation at shorter times $t < \tau_r$ is identical for the quantum-mechanical and classical descriptions, because a wave packet composed of stationary states performs motion by the laws of geometrical optics [9]. The latter becomes possible by virtue of the fact that the spatial size of the wave packet is considerably smaller than the size of the classical trajectory.

In conclusion, we may say that the phenomenon of phonon autoecho was observed in semimetals with the use of the pump–probe method with high-energy laser pulses. Phonon autoecho, which is manifested as the collapse and revival of coherent phonons, conclusively points to the nonclassical nature of the crystal lattice state obtained under exposure to ultrashort laser pulses.

REFERENCES

1. R. Merlin, Solid State Commun. **102**, 207 (1997).
2. O. V. Misochko, Zh. Éksp. Teor. Fiz. **119**, 285 (2001) [JETP **92**, 246 (2001)].
3. S. Hunsche, K. Wienecke, T. Dekorsy, and H. Kurz, Phys. Rev. Lett. **75**, 1815 (1995).
4. M. F. DeCamp, D. A. Reis, P. H. Bucksbaum, and R. Merlin, Phys. Rev. B **64**, 092301 (2001).
5. M. Hase, M. Kitajima, S. Nakashima, and K. Mizoguchi, Phys. Rev. Lett. **88**, 067401 (2002).
6. P. Tangney and S. Fahy, Phys. Rev. B **65**, 054302 (2002).
7. M. Hase, K. Mizoguchi, H. Harima, *et al.*, Phys. Rev. B **58**, 5448 (1998).
8. N. N. Bogolyubov, Jr., B. I. Sadovnikov, and A. S. Shumovskiĭ, *Mathematical Methods in Statistical Mechanics of Model Systems* (Nauka, Moscow, 1989).
9. I. Sh. Averbukh and N. F. Perel'man, Usp. Fiz. Nauk **161** (7), 41 (1991) [Sov. Phys. Usp. **34**, 572 (1991)].
10. P. Meystre and M. Sargent III, *Elements of Quantum Optics* (Springer, Berlin, 1991).
11. L. P. Pitaevskiĭ, Usp. Fiz. Nauk **168**, 641 (1998) [Phys. Usp. **41**, 569 (1998)].
12. M. Greiner, O. Mandel, T. W. Hansch, and I. Bloch, Nature **419**, 51 (2002).
13. Presence of second harmonic in spectrum provides an additional evidence on realization of fractional regeneration of the order of 1/2, see M. J. J. Vrakking, D. M. Villeneuve, and A. Stolow, Phys. Rev. A **54**, R37 (1996).
14. O. V. Misochko, K. Kisoda, K. Sakai, and S. Nakashima, Appl. Phys. Lett. **76**, 961 (2000).
15. O. V. Misochko, K. Sakai, and S. Nakashima, Phys. Rev. B **61**, 11 225 (2000).
16. A. V. Kuznetzov and C. J. Stanton, Phys. Rev. Lett. **73**, 3243 (1994).
17. O. V. Misochko, M. Tani, K. Sakai, *et al.*, Phys. Rev. B **58**, 12789 (1998).

Translated by A. Bagatur'yants

Increase in the Superconducting Transition Temperature in Zr–Hf Alloys Due To *s–d* Electron Transfer under Pressure

I. O. Bashkin*, M. V. Nefedova, E. G. Ponyatovsky, and V. G. Tissen

Institute of Solid-State Physics, Russian Academy of Sciences, Chernogolovka, Moscow region, 142432 Russia
*e-mail: bashkin@issp.ac.ru
Received June 23, 2003

The superconducting transition temperatures T_c of Zr–Hf alloys are measured as a function of pressure up to 47.4 GPa. It is found that the value of T_c experiences jumps due to the transition of the hexagonal ω phase to the bcc β phase: T_c of the $Zr_{80}Hf_{20}$ alloy increases from 3.2 to 11 K at $P = 35.0$ GPa, and a jump in T_c from 3.4 to 10 K is observed for the $Zr_{67}Hf_{33}$ alloy at $P = 40.9$ GPa. The isobars of the concentration dependence $T_c(c)$ of the bcc Zr–Hf alloys are qualitatively similar to the $T_c(c)$ curves for the bcc phases in the systems of V*b*–IV*b* subgroup elements at $P = 1$ atm. The data obtained indicate that, because of the *s–d* electron transition, the IV*b* subgroup metals become similar in their crystal structure and superconducting properties to the V*b* subgroup metals. © 2003 MAIK "Nauka/Interperiodica".

PACS numbers: 74.62.Fj; 64.70.Kb

1. INTRODUCTION

The development of methods for band-structure calculations of metals in the last three decades has opened the way for the estimation of the stability of crystal structures as a function of their electronic configuration and volume (see, for example, [1–3]). For the metals located early in the periods of the periodic table, it was shown [2] that *s* electrons must be transferred to the *d* band upon compression, because the narrow *d* band is displaced with respect to the bottom of the *sp* band. Hexagonal ω to bcc β phase transitions in Zr and Hf at high pressures due to an increase in the stability of the bcc structure with increasing *d*-band occupancy were predicted theoretically virtually simultaneously with their experimental discovery [5–9]. The agreement between calculation and experiment stimulated interest in the problem of *s–d* electron transitions under pressure. The pressure of the ω⟶β transformation at 20°C equals ~30 GPa for Zr and ~71 GPa for Hf. Titanium at room temperature transforms to phases with the orthorhombic structure only under pressures of 116–140 GPa, and the β phase does not form up to 220 GPa [10–12]. As the accuracy of calculations increased, it became possible to theoretically describe the entire sequence of α⟶ω⟶β phase transformations in Zr and Hf under pressure, starting from the hcp α phase stable at $P = 1$ atm [13–15]. Thus, Zr and Hf at high pressures become analogous in the occupancy of the *d* band and in their crystal structures to the V*b* group metals (Nb and Ta).

Akahama *et al.* [7, 8] extended this analogy to superconducting properties as well, finding that bcc Zr at $P = 30$ GPa has approximately the same T_c as bcc Nb at atmospheric pressure, whereas the starting hcp Zr and Hf phases have low superconducting transition temperatures T_c equal to 0.7 and 0.35 K, respectively. On the other hand, bcc Ta and Nb are characterized by significantly higher values of T_c (5.4 and 9.25 K, respectively).

The change in the electronic configuration and resemblance of the Ti subgroup metals to the V*b* group metals must lead to bright effects under pressure and in their alloys, because doping itself is a factor that affects the mutual arrangement of the Fermi level and the *d*-band features [1]. Upon doping vanadium, niobium, and tantalum with IV*b* group metals, the values of T_c appreciably increase. It should be expected that the concentration dependence of T_c in IV*b*–Zr alloys will also be similar in shape after transition to the β phase under pressure. However, the studies of phase transitions and superconductivity in binary IV*b*–IV*b* alloys under pressure are restricted to the Ti–Zr system. For Ti–Zr alloys, it was shown that the parameters of the triple α⟶ω⟶β equilibrium point in the *T–P* diagram strongly decrease as compared to the pure metals [16] and, after the transition of the alloys to the β phase, the superconducting transition temperature increases with increasing concentration of titanium, reaching 15 K in the TiZr alloy of equiatomic composition at 47 GPa [17].
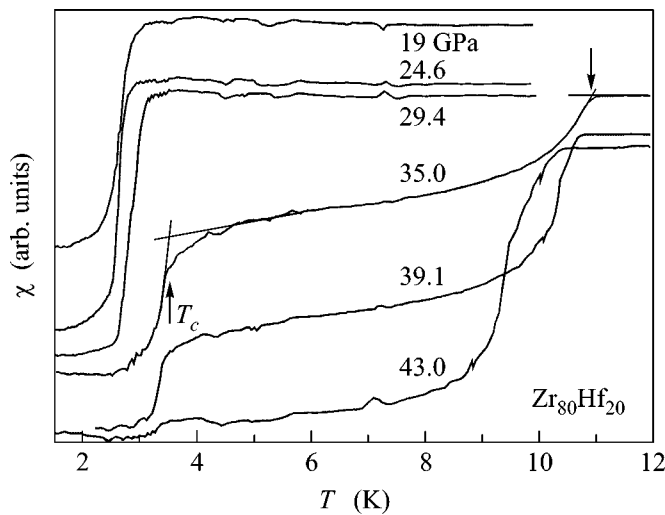
Fig. 1. Curves of the magnetic susceptibility $\chi(T)$ of the $Zr_{80}Hf_{20}$ alloy measured in the process of heating at the indicated values of pressure. The graphical determination of T_c is explained using the isobar at 35 GPa as an example.

Fig. 2. Pressure effect on the superconducting transition temperature in Zr [17], $Zr_{80}Hf_{20}$, and $Zr_{67}Hf_{33}$.

The behavior of the structure and superconducting properties of Zr–Hf alloys under pressure is of special interest. Because both elements are prone to a change in their electronic configuration, it might be expected from the phenomenological point of view that, as the pressure grows, a transition from the IVb–IVb system to an analogue of the IVb–Vb system will take place after the electronic and structural rearrangement in zirconium and further to an analogue of the Vb–Vb system after the rearrangement in hafnium. This work is devoted to an experimental investigation into the superconductivity of Zr–Hf alloys containing up to 33 at % Hf at pressures of up to 47 GPa to the point of their transition to the β phase.

2. PROCEDURE

The alloys to be studied were prepared from rods of iodide Zr and Hf remelted in a vacuum by zone melting. The purity of the starting metals was higher than 99.95 at %, including interstitial impurities. Chips cut from the starting metals were mechanically mixed in the required proportions and were pressed in the form of cylinders. Rods composed of ten separate cylinders were subjected to repeated remeltings in a vacuum. The final composition of the alloys was determined with the use of a JXA-5 local x-ray microanalyzer and comprised 20.6 ± 0.5 and 33.6 ± 0.2 at % Hf.

Superconducting transitions were detected as anomalies in the temperature dependence of the magnetic susceptibility $\chi(T)$ measured by an alternate current. The press was made of nonmagnetic materials and was equipped with diamond anvils. As well as other details of measurements, it was described previously [17]. In order to exclude the effects of the mechanical relax-
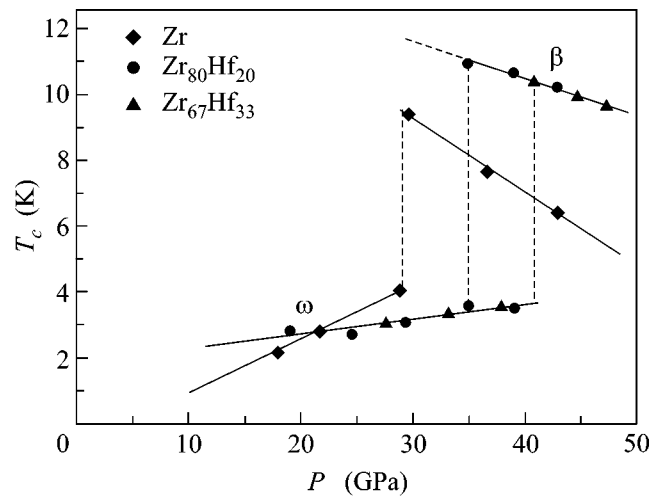
ation of the press upon cooling, the pressure was determined by the shift of the ruby luminescence line after heating the press up to room temperature at the end of a cycle of cooling and heating.

3. RESULTS

The isobaric curves $\chi(T)$ for the $Zr_{80}Hf_{20}$ alloy measured on heating the samples are shown in Fig. 1. The $\chi(T)$ curves for pure Zr and the $Zr_{67}Hf_{33}$ alloy are of the same shape. Jumps in the $\chi(T)$ curves are due to superconducting transitions in the ω phase ($2.5 < T_c < 3.5$ K) and in the β phase ($T_c > 9$ K). The jumps in the isobars at 19.0, 24.6, and 29.4 GPa for the single-phase states of the alloy with the ω structure are steep. The jumps corresponding to the two-phase $\omega + \beta$ states of the alloy at pressures of 35.0, 39.1, and 43.0 GPa are more diffuse because of microstresses and the proximity effect. The values of T_c were determined as the points of intersection between the tangent to the segment of the steep drop in the $\chi(T)$ curve and the extension of its high-temperature horizontal portion, as shown by arrows in Fig. 1.

The pressure dependences of T_c for the ω and β phases of pure Zr and the $Zr_{80}Hf_{20}$ and $Zr_{67}Hf_{33}$ alloys are shown in Fig. 2. As for zirconium, the lower segment of the $T_c(P)$ curve before the jump corresponds to the ω phase and the upper part corresponds to the β phase. This was determined by structural measurements *in situ*, whose results will be published later. It is evident in Fig. 2 that the superconducting transition temperatures of the ω and β phases of both the alloys studied in this work coincide within the limits of the experimental error. The $T_c(P)$ lines are straight with the

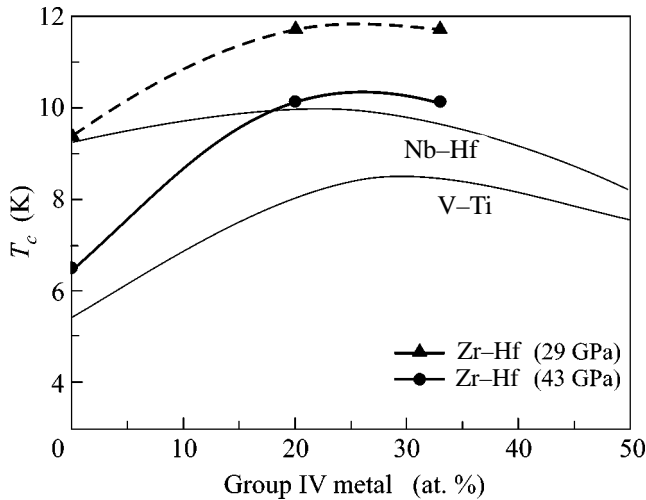**Fig. 3.** Dependence of the values of T_c on the Hf or Ti content for the β phases of Zr–Hf alloys at pressures of 29 and 43 GPa and Nb–Hf and V–Ti alloys [18] at atmospheric pressure.

slopes to the pressure axis dT_c/dP equal to +0.042 K/GPa for the ω phase and –0.122 K/GPa for the β phase. The pressures at the beginning of the ω⟶β phase transition, which were assigned to the appearance of the jumps in $\chi(T)$ corresponding to the β phase, comprise 29 GPa for pure Zr, 35 GPa for the $Zr_{80}Hf_{20}$ alloy, and 40.9 GPa for the $Zr_{67}Hf_{33}$ alloy. Assuming that the pressure of the ω⟶β transition in the Zr–Hf system is a linear function of concentration and extrapolating this function to pure Hf, we obtain a value of ~65 GPa, which is close to the published value of 71 GPa [9].

Figure 3 displays the isobaric concentration dependences of T_c at two pressures for the β phase of the Zr–Hf alloys studied in this work. Analogous dependences of T_c for two solid β solutions of V*b* and IV*b* group elements, namely, Nb–Hf and V–Ti alloys [18], are plotted in the figure for comparison. The isobaric curve for $P = 43$ GPa is constructed by the experimental dependence $T_c(P)$ shown in Fig. 2 and is depicted by a solid line. The isobaric curve for $P = 29$ GPa is constructed by the experimental value of T_c for pure zirconium and the points obtained by a linear extrapolation of the experimental lines $T_c(P)$ for the $Zr_{80}Hf_{20}$ and $Zr_{67}Hf_{33}$ alloys. It is shown by a dashed line. Note that T_c for β-Zr at $P = 29$ GPa virtually coincides with T_c for pure niobium at atmospheric pressure.

Figure 3 demonstrates that all four curves of the isobaric dependence of T_c on the concentration of the IV*b* group metal (Hf or Ti, respectively) are qualitatively similar. Both in bcc solid solutions of IV*b*–V*b* systems at atmospheric pressure and in solid β solutions of the Zr–Hf system (that is, IV*b*–IV*b*) at high pressures, T_c first increases and then passes through a shallow maxi-

mum as the concentration of the IV*b* group element (Hf for the Zr–Hf system) increases. At the chosen values of pressure (29 and 43 GPa), all the four curves are similar not only in shape but also in the position of the maximum located in the concentration range 25–30 at % Hf or Ti.

Because no direct methods are available for determining the degree of band occupancy under pressure, the occupancy can be judged only in an indirect way by experimental data. The experimental data obtained for alloys clearly confirm the ideas of *s*–*d* electron transition in Zr and Hf under the action of pressure. The isobaric curves $T_c(c)$ for the bcc phase at high pressure in the system in hand are close in shape to the analogous curves for the IV*b*–V*b* system (for example, Ti–V or Zr–Nb) at atmospheric pressure. That is, Zr–Hf alloys under pressures above the formation of the bcc phase, with which *s*–*d* electron transition is associated, behave as though they transform from IV*b*–IV*b* alloys to IV*b*–V*b* alloys. It is essential that the total number of *s* + *d* valence electrons remains unchanged and only their redistribution among subbands takes place. This fact clearly indicates that it is the degree of *d*-band occupancy rather than the total number of valence electrons that plays a determining role in the formation of the crystal structure and superconducting properties of metals of the IV*b* and V*b* subgroups of the periodic system of elements.

REFERENCES

1. I. V. Svechkarev and A. S. Panfilov, Phys. Status Solidi B **63**, 11 (1974).
2. C. Duthie and D. G. Pettifor, Phys. Rev. Lett. **38**, 564 (1977).
3. H. L. Skriver, Phys. Rev. B **31**, 1909 (1985).
4. J. S. Gyanchandani, S. C. Gupta, S. K. Sikka, and R. Chidambaram, J. Phys.: Condens. Matter **2**, 6457 (1990).
5. H. Xia, S. J. Duclos, A. L. Ruoff, and Y. K. Vohra, Phys. Rev. Lett. **64**, 204 (1990).
6. H. Xia, A. L. Ruoff, and Y. K. Vohra, Phys. Rev. B **44**, 10374 (1991).
7. Y. Akahama, M. Kobayashi, and H. Kawamura, J. Phys. Soc. Jpn. **60**, 3211 (1991).
8. Y. Akahama, M. Kobayashi, and H. Kawamura, J. Phys. Soc. Jpn. **59**, 3843 (1990).
9. H. Xia, G. Parthasarathy, H. Luo, *et al.*, Phys. Rev. B **42**, 6736 (1990).
10. Y. Akahama, H. Kawamura, and T. LeBihan, J. Phys.: Condens. Matter **14**, 10583 (2002).

11. Y. Akahama, K. Nakano, S. Umemoto, *et al.*, Phys. Rev. Lett. **87**, 275503 (2001).

12. Y. K. Vohra and P. T. Spencer, Phys. Rev. Lett. **86**, 3068 (2001).

13. R. Ahuja, J. M. Wills, B. Johansson, and O. Eriksson, Phys. Rev. B **48**, 16269 (1993).

14. S. A. Ostanin and V. Yu. Trubitsin, Phys. Rev. B **57**, 13485 (1993).

15. K. D. Joshi, G. Jyoti, S. C. Gupta, and S. K. Sikka, J. Phys.: Condens. Matter **14**, 10921 (2002).

16. I. O. Bashkin, A. Yu. Pagnuev, A. F. Gurov, *et al.*, Fiz. Tverd. Tela (St. Petersburg) **42**, 163 (2000) [Phys. Solid State **42**, 170 (2000)].

17. I. O. Bashkin, V. G. Tissen, M. V. Nefedova, *et al.*, Pis'ma Zh. Éksp. Teor. Fiz. **73**, 80 (2001) [JETP Lett. **73**, 75 (2001)].

18. *Superconducting Materials*, Ed. by E. M. Savitskiĭ, Yu. V. Efimov, N. D. Kozlova, *et al.* (Metallurgiya, Moscow, 1976).

Translated by A. Bagatur'yants

Anomalous Behavior of the Velocity of Hypersonic Acoustic Phonons in $(NH_4)_3H(SO_4)_2$ Crystals

S. G. Lushnikov[1],*, A. I. Fedoseev[1], L. A. Shuvalov[2], and H. Schmidt[3]

[1]Ioffe Physicotechnical Institute, Russian Academy of Sciences, St. Petersburg, 194021 Russia
[2]Shubnikov Institute of Crystallography, Russian Academy of Sciences, Moscow, 117333 Russia
[3]Montana State University, Bozeman, Montana, USA
*e-mail: sergey.lushnikov@mail.ioffe.ru

The velocity of quasi-longitudinal acoustic (QLA) phonons in $(NH_4)_3H(SO_4)_2$ (TAHS) crystals was studied by Brillouin scattering in the temperature range from 295 to 430 K. It was found that the QLA phonon velocity in the vicinity of a superionic ferroelastic phase transition ($T_c = 413$ K) exhibits anomalous temperature dependence. At $T < T_c$, an additional contribution is separated from the temperature dependence of the hypersound velocity, the behavior of which is correlated with variations of the conductivity of a TAHS crystal. Based on an analysis of the experimental data, a thermoactivation mechanism explaining the anomalous behavior of the QLA phonon velocity is proposed and the corresponding activation energy is estimated. © *2003 MAIK "Nauka/Interperiodica".*

PACS numbers: 63.20.–e; 64.70.Kb; 78.35.+c

The crystal lattice dynamics related to disordering in one of the sublattices is a subject of extensive investigation in the physics of condensed media [1]. Model objects for such investigations are offered by crystals possessing superionic conductivity, in which the disorder is introduced by melting the conducting subsystem [2]. The most promising compounds for investigations of the effect of a partial disorder on the acoustical properties are crystals with the general formula $Me_zH_y(AO_4)_{(z+y)/2} \cdot xH_2O$ (Me = Cs, Rb, NH_4; A = S, Se; $0 \le x \le 1$), known to possess proton conductivity. All crystals of this class are characterized by a common superionic conductivity mechanism involving a dynamically disordered network of hydrogen bonds [3], for which reason these crystals are referred to as superprotonic.

A characteristic feature of most compounds of the class under consideration is a structural phase transition from a paraelastic superionic state to a low-conducting ferroelastic state. The appearance of a spontaneous deformation with a simultaneous change in the conductivity give hopes for a direct observation of the effects related to the interaction of acoustic phonons with the conducting subsystem of a crystal in the course of ultrasonic and hypersonic measurements. Indeed, the ultrasonic experiments showed evidence of an anomalous behavior of the velocity and damping of acoustic phonons in some compounds of the aforementioned class of superprotonic crystals [4, 5], which was explained in terms of the acoustoionic interaction.

A principally different pattern was observed in the experiments involving measurements of the Brillouin scattering in these crystals [6, 7]. Here, the behavior of the hypersonic acoustic phonons was determined, at first glance, only by interaction between the order parameter and the deformation, which is typical of the ferroelastic structural phase transitions in the vicinity of T_c. This behavior agrees with the model notions about a frequency-dependent acoustic response in superionic crystals [8].

At the same time, a thorough analysis of the Brillouin scattering data suggests that there is an additional contribution from the conducting subsystem at hypersonic frequencies. For example, it was found that the jumps of elastic constants at $T = T_c$ in $Rb_3H(SeO_4)_2$ (TRHSe) crystals, as revealed by the experiments, contradict a phenomenological model of the ferroelastic phase transition based on the Landau theory (the observed anomalies in elastic constants could not be described using expansions of the thermodynamic potential retaining terms up to the sixth order) [9]. Another characteristic feature is a nontrivial dispersion of the sound velocity revealed by the temperature dependence of the QLA phonon velocity in the vicinity of T_c of a TRHSe [10]. All these data suggested that the acoustoionic interaction modifies the acoustic response of a crystal even in the region of hypersonic frequencies.

Here we report the results of investigations of the temperature dependence of the QLA phonon velocity by Brillouin scattering spectroscopy and present evidence for the existence of the acoustoionic contribution to this dependence at hypersonic frequencies in a superprotonic $(NH_4)_3H(SO_4)_2$ TAHS crystal.

The single crystals of $(NH_4)_3H(SO_4)_2$ were grown at the Institute of Crystallography (Moscow) by evaporation from an aqueous solution. At room temperature, TAHS crystals possess a monoclinic symmetry (C_{2h}^6) with the unit cell parameters a $a_m = 10.153(3)$ Å, $b_m = 5.854(2)$ Å, $c_m = 15.410(6)$ Å, $\beta_m = 101.76(2)°$ [11]. The improper ferroelastic phase transition at $T_c = 413$ K is accompanied by a jump in the conductivity, after which it acquires the value $\sigma \approx 10^{-2}\ \Omega^{-1}\ cm^{-1}$ [12]. The measurements were performed using crystal plates with dimensions $5 \times 5.8 \times 2.8$ mm cut from a TAHS single crystal. The sample orientation was determined by X-ray crystal diffraction.

The incident beam was produced by an argon laser operating at $\lambda = 488$ or 514 nm. The scattered light was analyzed by piezoscanning, three- and five-pass Fabry–Perot interferometers in a $180°$ scattering geometry. The free spectral range (FSR) of the interferometer was varied from 45 to 22 GHz. The finesse of the interferometer tuning was not less than 60.

Figure 1 shows examples of the experimental scattering spectra of a TAHS crystal measured at various temperatures. The spectra display well-pronounced peaks of the elastic (Rayleigh) scattering (at a zero frequency shift) and three doublets, corresponding to the Stokes and anti-Stokes components of scattering on the acoustic phonons (one quasi-longitudinal and two quasi-transverse). An increase in the temperature modifies the spectra, which is manifested by changes in the frequency position, width, and intensity of the inelastic scattering components. These changes are clearly revealed by comparison of the spectra recorded at various temperatures (Fig. 1).

In this paper, the consideration is restricted to the shift $\Delta\nu$ in the QLA phonon frequency, which is directly proportional to the velocity of propagation of this phonon: $V = \Delta\nu\lambda/2n$, where n is the refractive index. Thus, considering the frequency shift, we in fact study the behavior of the QLA phonon velocity (provided that the temperature dependence of the refractive index can be ignored). It should be noted that the QLA phonon velocity in crystals possessing the monoclinic symmetry is determined by a linear combination of several elastic constants, except for the case when the phonon wavevector is parallel to the second-order axis ($\mathbf{q}_{ph} \parallel C_2$) [13].

The experimental scattering spectra were processed by least squares, using Lorentz functions for fitting to the inelastic scattering doublets. An example of such treatment is given in Fig. 1.

Figure 2 shows plots of the frequency shift versus temperature for the QLA phonons propagating in the ($a_m b_m$) plane. As can be seen, the curves can be divided into three characteristic regions. The first region, extending from room temperature up to about 340 K, is well described by a linear temperature dependence. This linear decrease in the QLA phonon velocity is
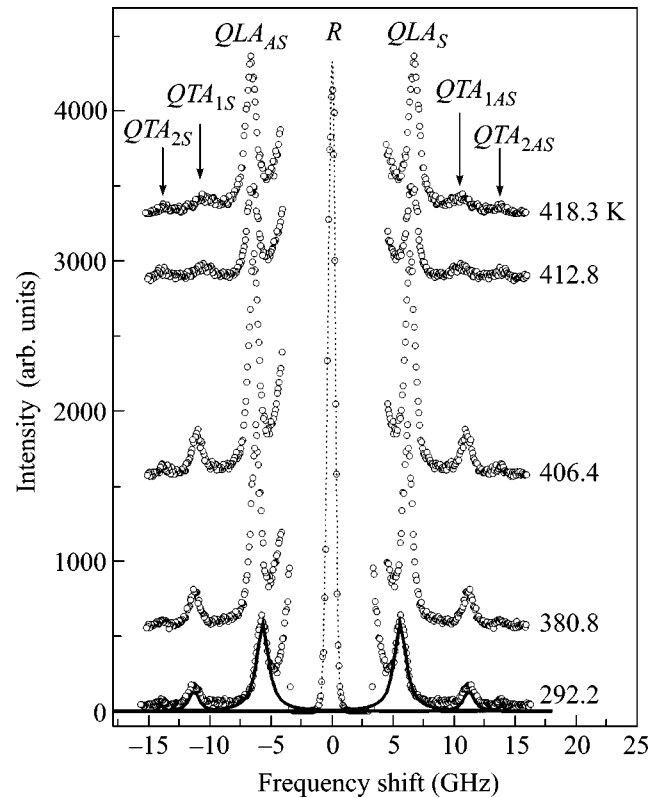

Fig. 1. The Brillouin scattering spectra of a TAHS crystal measured at various temperatures, showing the Rayleigh scattering component (R) and three doublets corresponding to the quasi-longitudinal (QLA) and quasi-transverse (QTA) acoustic phonons. The FSR of the Fabry–Perot interferometer was 21 GHz. Dashed curve shows the results of deconvolution of the phonon peaks in the room-temperature spectrum using a procedure described in the text.

explained by the anharmonicity of the crystal lattice. The second region shows "softening" of the frequency shift, which declines from the linear behavior in the vicinity of 340 K. This behavior is observed up to a temperature of 413 K (Fig. 2), where the $\Delta\nu$ value exhibits a jump. The observed anomaly in the QLA phonon velocity at the point of the improper ferroelastic phase transition does not correspond to the $\eta^2 u$ invariant (η is the order parameter and u is the strain) in the expansion of the thermodynamic potential [14]. A more thorough and correct analysis of the anomalous behavior of the QLA phonon velocity in the vicinity of T_c within the framework of a phenomenological model developed in [15] is hardly possible, since data appeared about the existence of a high-temperature intermediate phase in TAHS crystals [16].

Let us return to the analysis of the frequency shift "softening" observed for the hypersonic phonons in the temperature interval from 340 to 413 K. For an adequate description of the behavior of the phonon velocity, we have to take into account two processes manifested in the temperature dependences of $\Delta\nu$: (i) a linear
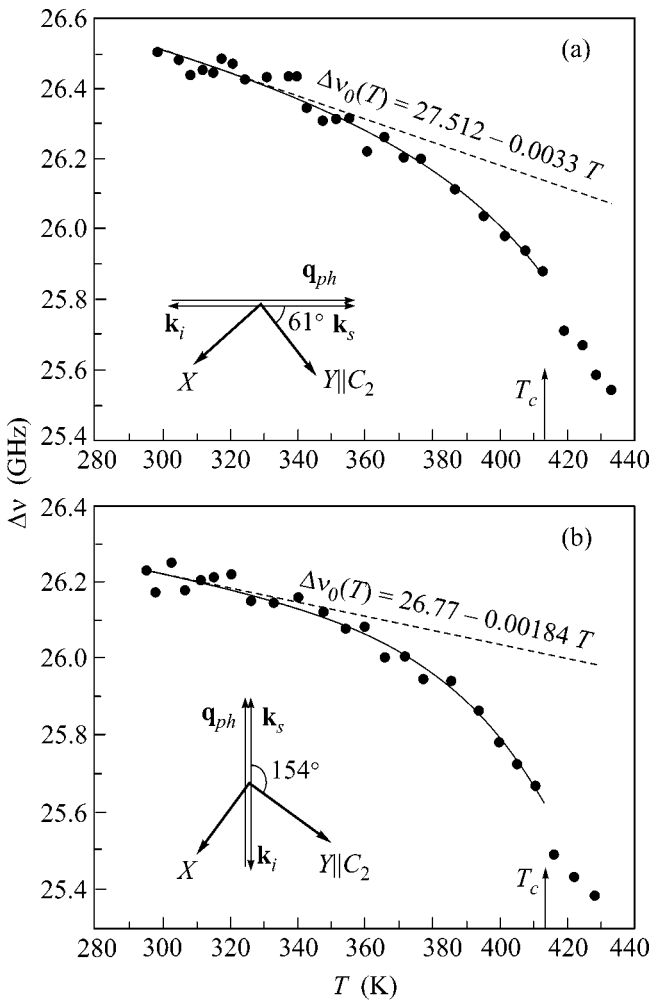
Fig. 2. Temperature variation of the frequency shift of the QLA phonon propagating in a TAHS crystal in a plane perpendicular to the pseudohexagonal axis $\tilde{Z}$, at an angle of (a) 61° or (b) 154.33° relative to the $C_2 \parallel Y_m \parallel \tilde{Y}$ axis. Insets show the experimental geometry. Dashed line shows the contribution to $\Delta v(T)$ related to anharmonicity of the crystal lattice; solid curve is calculated by formula (2) with allowance for the crystal anharmonicity.
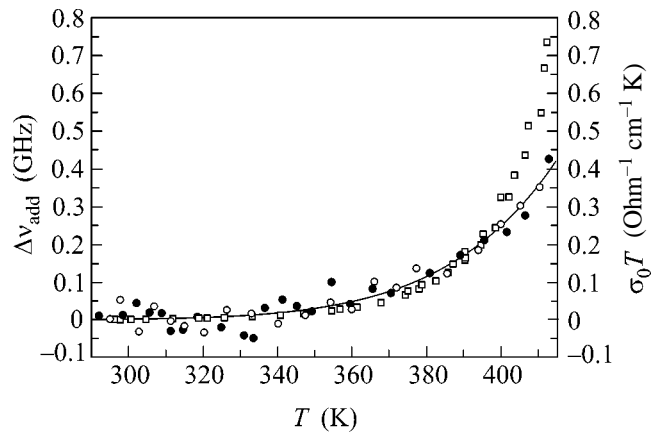

Fig. 3. Temperature variation of the additional contribution (separated as described in the text) to the QLA phonon velocity in a TAHS crystal for the experimental geometry indicated in Figs. 2a (●) and 2b (○). Symbols (□) present the temperature dependence of the conductivity plotted in a comparable scale (data from [12]); solid curve is calculated by formula (2).

contribution to the phonon velocity determined by the anharmonicity (Δv_{anh}) and (ii) an additional nonlinear contribution (Δv_{add}) of unknown nature. In the subsequent analysis of the temperature dependence of the QLA phonon velocity, we use the following procedure for separating the latter additional contribution. The linear portion of the temperature dependence of Δv was approximated by least squares in the 300–340 K interval and then extrapolated to the 340–413 K range. The nonlinear contribution, determined by subtracting experimental values from this calculated linear dependence, is plotted in Fig. 3.

There are two most probable reasons for the observed "softening" of the hypersonic phonon velocity in the temperature interval under consideration:

(a) the proximity of the improper ferroelastic phase transition to the tricritical point and (b) manifestations of the acoustoionic interaction. In the former case, the temperature variation of the QLA phonon frequency shift is determined by the square of the order parameter, which (taking into account that ($\eta \sim (T - T_c)^{1/4}$) does not agree with the observed behavior. Therefore, the above assumption that the QLA phonon velocity "softening" is related to the proximity of the improper ferroelastic phase transition to the tricritical point is not justified.

Let us consider the possibility that the acoustoionic interaction contributes to the velocity of hypersonic acoustic phonons. The temperature dependence of the conductivity of a TAHS crystal presented in Fig. 3 is well correlated with the behavior of the additional contribution Δv_{add} to the hypersonic phonon velocity on approaching T_c. This agreement between the temperature variation of the conductivity and the QLA phonon velocity suggests that these changes are determined by the same process.

As is known, the conductivity of TAHS obeys the Arrhenius relation [12]

$$\sigma T = A/T \exp(-H_a/kT), \qquad (1)$$

where A is a preexponential factor, H_a is the enthalpy of activation, and k is the Boltzmann. We may suggest that $\Delta v_{\mathrm{add}}(T)$ in the temperature interval under consideration is also described by a law of this type. In order to verify this hypothesis, we approximated the obtained $\Delta v_{\mathrm{add}}(T)$ curve by the empirical function

$$\Delta v_{\mathrm{add}}(T) = C^* \exp(-H_a/kT), \qquad (2)$$

where C^* is a proportionality coefficient with a dimensionality of reciprocal time. As can be seen from Fig. 3, the experimental temperature dependence of the

phonon frequency shift is well described by the proposed function. Apparently, the change of the Δv_{add} with the temperature is also related to a thermoactivated process and can be described by the Arrhenius law. The value of the enthalpy of activation obtained for this law ($H_a = 0.51$ eV) agrees well with the experimental data on the conductivity of TAHS crystals [12]. It should be noted that an analysis of the temperature dependences of the velocity of hypersonic phonons propagating in various directions of the ($a_m b_m$) plane yielded (as well as the conductivity measurements) close values of the activation energy, which corresponds to the isotropy of conductivity in this plane.

A more complicated situation takes place in the vicinity of T_c. As can be seen from the data in Fig. 3, the temperature variation of the conductivity changes above 400 K, which is probably related to the appearance of a critical contribution to the conductivity. No such critical contribution in the vicinity of T_c is observed in the behavior of the hypersonic acoustic phonons.

Thus, we may conclude that the behavior of the hypersonic acoustic phonons in the vicinity of the phase transition in TAHS is determined by disordering of the proton subsystem. The interaction of hypersonic waves with the dynamic network of hydrogen bonds significantly modifies the behavior of acoustic phonons in the experiments with the Brillouin scattering. The results of our investigation provide direct evidence for the existence of the acoustoionic interaction in crystals featuring no piezoelectric effect at hypersonic frequencies.

REFERENCES

1. U. T. Hochli, K. Knorr, and A. Loidl, Adv. Phys. **51**, 589 (2002).

2. D. A. Keen, J. Phys.: Condens. Matter **14**, R819 (2002).

3. B. V. Merinov, Solid State Ionics **84**, 89 (1996).

4. B. V. Shchepetil'nikov, A. I. Baranov, L. A. Shuvalov, and V. A. Dolbinina, Fiz. Tverd. Tela (Leningrad) **32**, 254 (1990) [Sov. Phys. Solid State **32**, 142 (1990)].

5. B. V. Shchepetil'nikov, A. I. Baranov, L. A. Shuvalov, and N. M. Shchagina, Fiz. Tverd. Tela (Leningrad) **32**, 2885 (1990) [Sov. Phys. Solid State **32**, 1676 (1990)].

6. Y. Luspin, Y. Vallis, and G. Hauret, Solid State Ionics **80**, 277 (1995).

7. Y. Luspin, D. De Sousa Meneses, P. Simona, and G. Hauret, Eur. Phys. J. B **10**, 215 (1999).

8. J. B. Boyce and B. A. Huberman, Phys. Rep. **51**, 189 (1979).

9. S. G. Lushnikov and I. G. Siny, Ferroelectrics **106**, 1073 (1990).

10. S. G. Lushnikov and L. A. Shuvalov, Ferroelectrics **124**, 409 (1991).

11. S. Suzuki and Y. Makita, Acta Crystallogr. B **34**, 732 (1978).

12. L. Schwalowsky, V. Vinnichenko, A. Baranov, *et al.*, J. Phys.: Condens. Matter **10**, 3019 (1998).

13. S. G. Lushnikov, S. D. Prokhorova, I. G. Siniĭ, and G. A. Smolenskiĭ, Fiz. Tverd. Tela (Leningrad) **29**, 496 (1987) [Sov. Phys. Solid State **29**, 280 (1987)].

14. W. Rehwald, Adv. Phys. **22**, 721 (1973).

15. N. M. Plakida and W. Salejda, Phys. Status Solidi B **148**, 473 (1988).

16. T. Fukami, K. Tobaru, K. Kaneda, *et al.*, J. Phys. Soc. Jpn. **63**, 2006 (1996).

Translated by P. Pozdeev

Magnetic and Magneto-Lattice Dynamics in GdMn$_2$O$_5$

E. I. Golovenchits* and V. A. Sanina

Ioffe Physicotechnical Institute, Russian Academy of Sciences, Politekhnicheskaya ul. 26, St. Petersburg, 194021 Russia

*e-mail: e.golovenchits@mail.ioffe.ru

The dynamics of magnetoelectric RMn$_2$O$_5$ crystals (R = Eu and Gd) was studied in the frequency and temperature ranges 20–300 GHz and 5–50 K, respectively. The crystals possessed magnetic and ferroelectric long-range order and had close transition temperatures, $T_{N, C} \simeq 36$ and 30 K for R= Eu and Gd, respectively. Mixed magneto-lattice excitations were observed in GdMn$_2$O$_5$; the excitations were most intense near the transition temperature $T \simeq 30$ K at frequencies close to the antiferromagnetic resonance frequencies of the Mn subsystem. Along with the antiferromagnetic resonance of the Mn subsystem, the ferromagnetic resonance of the Gd subsystem was observed in GdMn$_2$O$_5$ in an external magnetic field. No such dynamics was characteristic of EuMn$_2$O$_5$. © 2003 MAIK "Nauka/Interperiodica".

PACS numbers: 76.50.+g; 75.47.Lx; 77.80.-e

RMn$_2$O$_5$ crystals, where R stands for rare-earth metal ions from Pr to Lu, Y, or Bi, are magnetoelectric substances that simultaneously possess antiferromagnetic and ferroelectric long-range order with close Neel and Curie temperatures $T_{N, C} \simeq 30$–40 K (space group *Pbam* at room temperature). The magnetic, dielectric, and magnetoelectric properties of several crystals with different R ions were studied in [1–6]; the neutron diffraction data can be found in [7, 8]. An incommensurate magnetic structure with the propagation vector $\mathbf{k} = (\mathbf{1/2, 0, z})$ is usually formed in RMn$_2$O$_5$ at $T \leq T_N$; the $z \simeq$ 0.3–0.38 value depends on the type of the R ion. One more phase transition with changes in magnetic and structural properties occurs in these crystals close to 15–20 K.

This work presents the results of a study of the dynamic properties of RMn$_2$O$_5$ with the Eu^{3+} ion, which is nonmagnetic in the ground state $^7F_0$, and the Gd^{3+} ion ($^8S_{7/2}$), whose spin moment is maximum among the R ions. The dynamics of crystals with R = Eu and Gd is substantially different. We also report the results of magnetic and dielectric studies of GdMn$_2$O$_5$.

EuMn$_2$O$_5$ forms an incommensurate antiferromagnetic structure with ferroelectric ordering and has close Neel and Curie temperatures $T_{N, C} \simeq 36$ K [3, 8]. Antiferromagnetic ordering in GdMn$_2$O$_5$ arises in the Mn subsystem at a temperature close to the T_N temperature for EuMn$_2$O$_5$. An additional phase transition, however, occurs close to $T \simeq 30$ K [6]. As follows from the results of this work, the low-temperature ($T \leq 30$ K) GdMn$_2$O$_5$ phase is characterized by uniform magnetic (antiferromagnetic and ferromagnetic in the Mn and Gd subsystems, respectively) and ferroelectric orderings.

The dynamic studies were performed on a quasi-optical spectrometer using the transmission scheme. The source of radiation was backward-wave tubes, and the receivers were InSb-based detectors cooled with liquid helium. The single crystals were grown by the method of spontaneous crystallization described in [2] in the form of well-faceted parallelepipeds of dimensions $5 \times 4 \times 4$ mm. Plates ~0.5 mm thick were cut normally to crystal axes **a**, **b**, and **c**. The plates were oriented normally to the direction of electromagnetic wave propagation by their developed surfaces. Variable electric and magnetic (**e** and **h**, respectively) fields were oriented in the plane of the sample. A constant magnetic field H_0 of up to 2 T was also applied in the plane of the sample. The magnetic field dependences of the relative absorption coefficient $\Gamma_{F, T} = 1 - P(H)P_{\max}$ were studied at fixed frequencies and temperatures. Here, $P(H)$ and $P_{\max}$ are the microwave signal powers transmitted through the sample at the current field value and the field value corresponding to maximum transmission, respectively. In addition, we studied the temperature dependences of the relative absorption coefficient $\Gamma_F = 1 - P(T)P_{\max}$ in the absence of a magnetic field at fixed frequencies. The $\Gamma_{F, T}(H_0)$ and $\Gamma_F(T)$ dependences were used to construct the frequency and field dependences of the absorption coefficient at fixed temperatures (magnetic resonance spectra).

Sweeping the magnetic field caused the appearance of resonance absorption only for GdMn$_2$O$_5$ and only at the $H_0 \parallel$ **a** orientation (see Fig. 1). Two characteristic signals with gaps of 150 (I) and 100 GHz (II), which depended linearly on the field, were observed. It follows from the inset in Fig. 1 that the gap in spectrum I decreased to 130 GHz as temperature increased to $T \simeq$
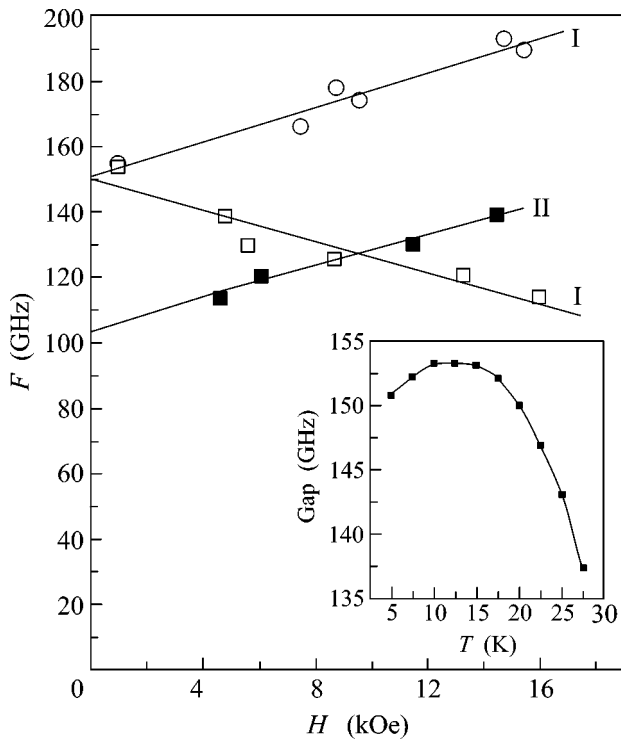
Fig. 1. Dependences of the frequencies of magnetic resonances on external magnetic field H_0 oriented along the **a** axis of a GdMn$_2$O$_5$ plate with the developed plane **ac** (sample *2* according to the classification of Fig. 2); **h** ∥ **c**, $T = 5$ K. Shown in the inset is the temperature dependence of the gap in spectrum I.

Fig. 2. Temperature dependences of the relative absorption coefficient Γ at $H_0 = 0$ for GdMn$_2$O$_5$ samples: (*1*) the developed plane **ab**, **e** ∥ **a**, frequency $F = 137$ GHz; (*2*) the developed plane **ac**, **e** ∥ **a**, frequency $F = 129.9$ GHz; (*3*) the developed plane **ab**, **e** ∥ **b**, frequency $F = 135.1$ GHz; and (*4*) the developed plane **bc**, **e** ∥ **c**, frequency $F = 132.1$ GHz. Shown in the inset are the frequency dependences of Γ at the maximum of the absorption line near the $T = 30$ K temperature for samples *1*, *2*, and *3*.

30 K. Note that the temperature dependences of the intensities of signals I and II were different. The intensity of signal I changed with the temperature as the order parameter with a critical temperature of ~40 K. That of signal II decreased much more sharply as temperature increased and tended to zero at $T \simeq 30$ K.

Unlike the magnetic resonances, whose intensities decreased as the temperature approached ~30 K, absorption lines observed in the absence of a magnetic field had temperature dependences with maxima at $T \simeq 30$ K. The shape of the $\Gamma(T)$ dependences was determined by the orientation of the variable electric field with respect to crystal axes **a**, **b**, and **c** (see Fig. 2). These lines were likely caused by the dynamics of the lattice near the phase transition at $T \simeq 30$ K and were excited largely by the alternating electric field. A temperature hysteresis was observed for the absorption lines near $T \simeq 30$ K. The intensity of the lines depended on the frequency and was maximum near 130 GHz (see the inset in Fig. 2). It is noteworthy that this frequency is close to the gap value for the magnetic resonances (signals I) at $T \simeq 30$ K (see the inset in Fig. 1). The external magnetic field also influenced the lines of an electric nature with absorption maxima at $T \simeq 30$ K (see
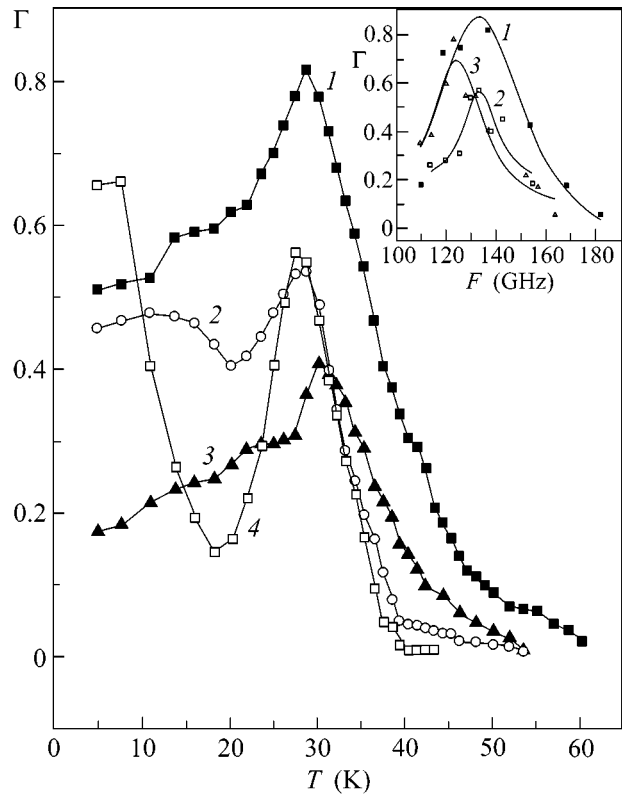
Fig. 3). This influence was most pronounced for the $H_0 \parallel$ **a** orientation. The absorption maximum then shifted to the frequency corresponding to the frequency of signal I at the given magnetic field value.

The closeness of the magnetic resonance I frequencies and the frequencies of the absorption lines of an electric nature and the influence of magnetic field H_0 on them are evidence that these lines have a mixed magneto-lattice character. It follows from Fig. 2 that, at low temperatures too, the lines with maximum absorption near 30 K are not completely resolved from the magnetic resonance lines. This leads us to conclude that low-temperature excitations also have a mixed character to a certain degree.

Low-intensity absorption signals were observed in EuMn$_2$O$_5$ in a wide frequency range of 30 to 300 GHz. The absorption was maximum at temperatures close to 36–40 K, which corresponded to the phase transition to the incommensurate magnetic and ferroelectric states. These absorption lines were virtually independent of the magnetic field and frequency.
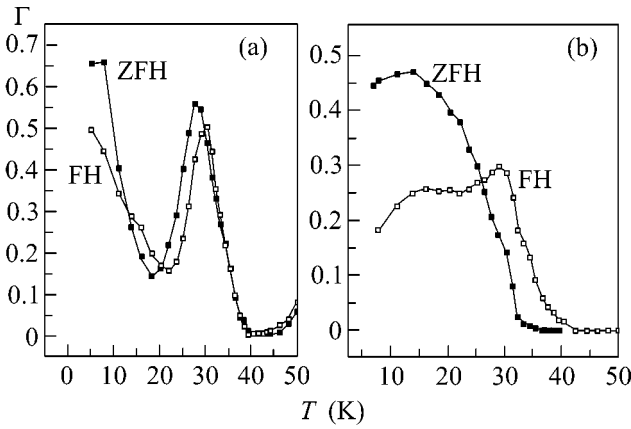
Fig. 3. The same dependences as in Fig. 2 for samples (a) *4* and (b) *1* recorded at $H_0 = 0$ under the conditions of slow heating to $T = 5$ K (ZFH) after preliminary slow cooling to $T \simeq 5$ K and under slow heating in a nonzero magnetic field $H_0 \neq 0$ (FH). The magnetic field was applied at $T = 5$ K. For sample *4*: $H_0 = 1.6$ T, $H_0 \parallel \mathbf{c}$, frequency $F = 132.1$ GHz; for sample *1*: $H_0 = 1.86$ T, $H_0 \parallel \mathbf{a}$, frequency $F = 168.5$ GHz.
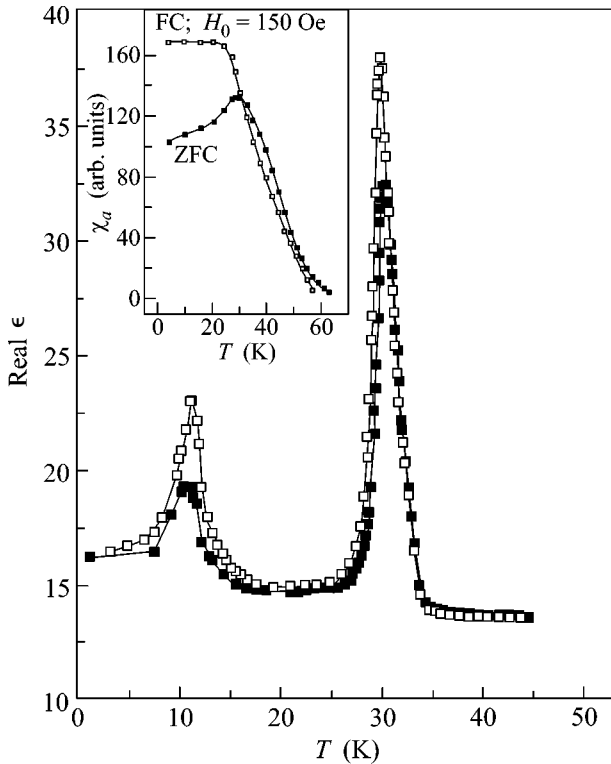

Fig. 4. Temperature dependences of the real permittivity part for $GdMn_2O_5$ at a 10 kHz frequency at the $\mathbf{e} \parallel \mathbf{b}$ orientation. The solid and open symbols were recorded in heating and cooling the sample, respectively. Shown in the inset are the temperature dependences of magnetic susceptibility (in arbitrary units) for $GdMn_2O_5$; frequency 10 kHz, $\mathbf{h} \parallel \mathbf{a}$, $h \simeq$ 4 Oe. The curves were recorded under sample cooling in the absence of an external magnetic field (ZFC) and in an $H_0 \simeq$ 40 Oe field, $H_0 \parallel \mathbf{a}$ (FC).

The results obtained in the magnetic and dielectric studies of $GdMn_2O_5$ (Fig. 4) show that, near 30 K, the real part of permittivity (Real ϵ) has a maximum similar to that recorded for $EuMn_2O_5$ near 36 K [2, 3]. This, together with the data on magnetoelectric susceptibility and pyrocurrent [4], leads us to conclude that the observed dielectric susceptibility anomaly characterizes the transition to the ferroelectric state with polarization along the **b** axis. The maximum of Real ϵ at $T \simeq$ 30 K was observed for $GdMn_2O_5$ when *e* was oriented along all crystal principal axes; the jump value was, however, two times larger at $\mathbf{e} \parallel \mathbf{b}$. The magnetic susceptibility of $GdMn_2O_5$ recorded by the induction method is shown in Fig. 4, according to which the temperature dependence of susceptibility is ferromagnetic in character for the $\mathbf{h} \parallel \mathbf{a}$ orientation. The susceptibility is saturated in a weak magnetic field and decreases starting with ~30 K, but its tail extends to the higher temperatures. We believe this susceptibility to characterize the Gd subsystem in the magnetizing field of the Mn subsystem.

Next, consider the data on the dynamics of the systems. Note that the shape of magnetic resonance spectra I in Fig. 1 is characteristic of the antiferromagnetic resonance of antiferromagnets with anisotropy of the easy axis type when the magnetic field is parallel to this axis (here, **a** axis of the crystal). The magnetic field dependence of antiferromagnetic resonance frequencies then has the form $\omega_{1,2} = \sqrt{2H_E H_A} \pm \gamma H_0$, where H_E and H_A are the exchange and anisotropy fields, respectively, and γ is the gyromagnetic ratio. For spectrum I, $\gamma \simeq 2.75 \pm 0.15$ and corresponds to a *g*-factor close to 2. These signals can naturally be assigned to the antiferromagnetic subsystem of Mn ions. For signals II, the $\omega(H_0)$ dependence has the form $\omega = \Delta\omega + \gamma H_0$. Its linear slope is the same as for spectrum I corresponding to a $g \simeq 2$ spin value. We assign this spectrum to the subsystem of Gd ions. The $\Delta\omega$ gap is likely to be induced by the effective exchange field of Mn–Gd interactions. Taking into account the magnetic susceptibility data and the high intensity of signals II, we assign them to the ferromagnetic resonance of the Gd subsystem. The character of the observed antiferromagnetic and ferromagnetic resonances is evidence that the magnetic state of $GdMn_2O_5$ crystals at $T \leq 30$ K is homogeneous. Recall that incommensurate magnetic structures are usually formed in RMn_2O_5 crystals with other R ions.

The neutron study of $EuMn_2O_5$ [8] shows that an additional phase transition occurs in this compound at $T \simeq 30$ K. This is the transition from the incommensurate to the commensurate spatially modulated magnetic structure with the vector $\mathbf{k} = (1/2, 0, 1/3)$. The phase transition from the spatially modulated to the homogeneous antiferromagnetic structure was observed in $EuMn_2O_5$ near $T \simeq 30$ K in a strong magnetic field $H_0 \simeq 20$ T oriented along the **c** axis. This transition was

accompanied by a polarization jump and the appearance of the linear magnetoelectric effect [9].

We believe homogeneous magnetic ordering to arise in $GdMn_2O_5$ near 28–30 K as a result of Gd–Mn–Gd polarization exchange [10]. The Mn subsystem is then under the action of the effective homogeneous field created by the Gd subsystem. The maximum contribution to polarization exchange is isotropic [10], and the component of this field along the **c** axis of the crystal may be responsible for the homogeneous antiferromagnetic state of the Mn subsystem (this is similar to the transition in $EuMn_2O_5$ in a strong external field [9]). Note that the structural phase transition (the arising of ferroelectric ordering) in $GdMn_2O_5$ is displaced along the temperature axis toward lower temperatures compared with RMn_2O_5 crystals containing other R ions. The transition occurs simultaneously with the formation of the homogeneous magnetic states of the Mn and Gd subsystems. Because of the homogeneous magnetic state of $GdMn_2O_5$, the compound is characterized by a strong linear magnetoelectric effect [6] and a strong coupling between magnetic and structural states resulting in the mixed dynamics observed and studied in this work.

To summarize, the presence of magnetic R ions with fairly strong R–Mn–R exchange interactions in RMn_2O_5 manganite crystals substantially influences the magnetic, magnetoelectric, and structural properties of these systems.

REFERENCES

1. S. C. Abrahams and J. L. Burnstein, Phys. Rev. **46**, 3776 (1967).
2. V. A. Sanina, L. M. Sapozhnikova, E. I. Golovenchits, *et al.*, Fiz. Tverd. Tela (Leningrad) **30**, 3015 (1988) [Sov. Phys. Solid State **30**, 1736 (1988)].
3. E. I. Golovenchits, V. A. Sanina, and A. V. Babinskiǐ, Zh. Éksp. Teor. Fiz. **112**, 284 (1997) [JETP **85**, 156 (1997)].
4. T. Doi and K. Kohn, Phase Transit. **38**, 273 (1992).
5. A. Inomata and K. Kohn, J. Phys.: Condens. Matter **8**, 2673 (1996).
6. H. Tsujino and K. Kohn, Solid State Commun. **83**, 639 (1992).
7. C. Wilkinson, F. Sinclair, P. Gardner, *et al.*, J. Phys. C: Solid State Phys. **14**, 1671 (1981).
8. V. Polyakov, V. Plakhty, M. Bonnet, *et al.*, Physica B (Amsterdam) **297**, 208 (2001).
9. Yu. F. Popov, A. M. Kadomtseva, G. P. Vorob'ev, *et al.*, J. Magn. Magn. Mater. **188**, 237 (1998).
10. E. I. Golovenchits and V. A. Sanina, Fiz. Tverd. Tela (Leningrad) **26**, 1640 (1984) [Sov. Phys. Solid State **26**, 996 (1984)].

Translated by V. Sipachev

Quantum Interactions in a Stochastic Representation and Two-Level Systems

Yu. E. Kuzovlev

Donetsk Physicotechnical Institute, National Academy of Sciences of Ukraine, Donetsk, 83114 Ukraine
e-mail: kuzovlev@kinetic.ac.donetsk.ua

The interaction between two quantum systems is formulated using a stochastic representation that allows one of them to be replaced by equivalent commutative random sources. The proposed method is applied to two-level systems in contact with a thermal bath. Strong-coupling effects and long-lived fluctuations of the total response of two systems in a common thermal bath are discussed. © 2003 MAIK "Nauka/Interperiodica".

PACS numbers: 05.30.–d; 05.60.Gg; 05.40.–a

1. The problems on the interaction between a certain microscopic dynamical system (DS) and its macroscopic environment (thermal bath) are typical for pure and applied quantum statistical physics. The interaction Hamiltonian is usually described by a bilinear form (or reduces to it), i.e.,

$$H_{int} = \sum_j B_j * D_j, \qquad (1)$$

where the operators D_j and B_j act in different linear (Hilbert) spaces D and B (DS and bath, respectively). In the Heisenberg representation, $B_j(t) \equiv \exp(iH_b t)B_j\exp(-iH_b t)$ (H_b is the Hamiltonian of the autonomous bath) serve as sources of random perturbations of the DS. However, as distinct from classical Langevin sources, these quantities are operator-valued and noncommutative and describe the evolution of the DS in the direct product $D \otimes B$ of the spaces.

The problem can be simplified by replacing $B_j(t)$ with equivalent (from the viewpoint of the results) commutative random sources, so that the evolution of the DS formally remains in D. Equivalence means the exact reproduction of the role of the thermostat temperature and the effects of the DS self-action through the thermostat, including dissipation.

A variant of such a replacement was proposed in [1]. Let $H_d(t)$ be the Hamiltonian of the autonomous DS

$$H(B, t) = H_d(t) + \sum_j B_j(t)D_j \qquad (2)$$

and certain observables J_k of the DS be measured. Then, the statistical operator $R(t)$ of the total system "DS (observed from the outside) plus bath" satisfies the equation

$$\dot{R} = v(t)J \circ R + i\{RH(B, t) - H(B, t)R\}, \qquad (3)$$

where $v(t)J \equiv \sum v_k(t)J_k$, $v_k(t)$ are test functions of measurement, and $\circ$ means symmetrized product. For $v_k(t) = 0$, it is the usual Neumann equation for the total density matrix. Otherwise, the trace of $R(t)$ in $D \otimes B$ yields [1] the characteristic functional $\Xi(t, v)$ of observables:

$$\text{Tr}_D\text{Tr}_B R = \text{Tr}_D\text{Tr}_B \overrightarrow{\exp}\left[\frac{1}{2}\int v(t')J(t')dt'\right]$$
$$\times \overleftarrow{\exp}\left[\frac{1}{2}\int v(t')J(t')dt'\right]R_{in} = \Xi(t, v). \qquad (4)$$

Here, $J_k(t)$ are operators in the Heisenberg representation, left (right) arrow means chronological (antichronological) ordering, integrals are calculated with respect to $t' < t$ (t is the current time), and $R_{in} = R(-\infty)$. Let us replace the operators $B(t)$ in Hamiltonian (2) with commutative (similar to C numbers) variables $\xi(t) = x(t) + iy(t)/2$ or $\eta(t) = x(t) - iy(t)/2$ and consider the equation

$$\dot{\rho}(t) = v(t)J \circ \rho(t) + L(t)\rho(t), \qquad (5)$$

where

$$L(t)\rho \equiv i\{\rho H(\eta, t) - H(\xi, t)\rho\}$$
$$= \sum_j y_j(t)D_j \circ \rho + i[\rho, H(x, t)], \qquad (6)$$

instead of Eq. (3), treating $\eta(t)$, $\xi(t)$, $x(t)$, and $y(t)$ as random processes reflecting the bath effect. Let R_{in} be factorized as $R_{in} = \rho(-\infty)\rho_b$, where $\rho_b = \text{Tr}_D R(-\infty)$ is the statistical operator of the bath. We specify the charac-

teristic functional of random sources $x(t)$ and $y(t)$ by the relation

$$\left\langle \exp\int [g(t)x(t) + f(t)y(t)]dt \right\rangle$$

$$= \mathrm{Tr}_B \overrightarrow{\exp}\left\{\frac{1}{2}\int g(t)B(t,f)dt\right\}\overleftarrow{\exp}\left\{\frac{1}{2}\int g(t)B(t,f)dt\right\}\rho_b,$$

(7)

where indices are omitted for brevity and the operators $B_j(t,f)$ are defined as

$$B_j(t,f) = U^+(t,f)B_jU(t,f),$$

$$\dot{U}(t,f) = -i\left\{H_b + \sum_j f_j(t)B_j\right\}U(t,f),$$

(8)

i.e., these operators characterize the nonautonomous behavior of the bath. On the left-hand side of Eq. (7), $g(t)$ and $f(t)$ are test functions for the sources $x(t)$ and $y(t)$, respectively. According to Eqs. (7) and (8), $g(t)$ on the right-hand side of Eq. (7) are test functions for the bath observables $B(t)$, while $f_j(t)$ are $B_j(t)$-conjugate classical forces perturbing the thermostat.

As was shown in [1], if the statistics of random sources in Eqs. (5) and (6) are determined by Eqs. (7) and (8), they exactly simulate the quantum bath; i.e.,

$$\langle\rho(t)\rangle = \mathrm{Tr}_B R(t),$$ (9)

$$\mathrm{Tr}_D \langle\rho(t)\rangle = \Xi(t,v),$$ (10)

where angular brackets mean averaging over $x(t)$ and $y(t)$ [or $\eta(t)$ and $\xi(t)$] according to Eqs. (7) and (8). The desired replacement is achieved at the cost of the doubling of the number of sources: one real observable (Hermitian operator) $B_j(t)$ is replaced with a pair of formally real variables $x_j(t)$ and $y_j(t)$ or a pair of complex conjugate variables η_j and $\xi_j = \eta_j^*$.

According to Eqs. (5) and (6), $x_j(t)$ serve as random forces (potentials), whereas $y_j(t)$ present the test functions of observation (measurement) of the DS by the bath [similar to $v_k(t)$ in Eq. (3)]. Under the action of only random pumping $x_j(t)$ [in the absence of $y_j(t)$], the entropy and energy of the DS would increase as far as possible. However, as in any measurement process, the terms with $y_j(t)$ in the stochastic Liouville operator (6) violate the unitarity of the evolution of the operator $\rho(t)$ and thereby decrease the phase-space volume (entropy) of the DS. Simultaneously, $y_j(t)$ are responsible for the energy outflow back to the bath, i.e., for dissipation and, therefore, for the nonuniform (thermal) probabilistic distribution of the DS energy. We emphasize that unitarity in the average is fulfilled according to Eqs. (9) and (10).

In view of Eqs. (7) and (8),

$$\left\langle \prod_{j,m} x(t_j)y(t'_m)\right\rangle = \left[\prod_m \frac{\delta}{\delta f(t'_m)}\left\langle\prod_j B(t_j,f)\right\rangle\right]_{f=0}.$$ (11)

Therefore, $\langle y(t)\rangle = 0$, $\langle y(t)y(t')\rangle = 0$, and all the higher autocorrelation functions of $y(t)$ are also equal to zero. However, the correlation functions between $y(t)$ and $x(t)$ are nonzero and present the response of the bath to the perturbation. Thus, $y(t)$ are, strictly speaking, not C numbers. Fortunately, their unusual properties only facilitate calculations. It is important that $y(t)$ can correlate only with later values $x(t' > t)$ according to the principle of causality.

For the case of the Gaussian equilibrium bath, all functions (11) are expressed in terms of pair correlation functions:

$$\langle x_j(\tau)x_m(0)\rangle = \int_0^\infty \cos(\omega\tau)S_{jm}(\omega)\frac{d\omega}{\pi},$$

$$\langle x_j(\tau)y_m(0)\rangle = 2\vartheta(\tau)$$ (12)

$$\times \int_0^\infty \sin(\omega\tau)\tanh\left(\frac{\omega}{2T}\right)S_{jm}(\omega)\frac{d\omega}{\pi}.$$

Here, T is temperature, $\vartheta(\tau)$ is the Heaviside step function, and $S_{jm}(\omega)$ is the nonnegative spectral matrix. Equations (12) show that neglect of the $y(t)$ component of the random sources in Eqs. (5) and (6) would mean in essence that the temperature of the thermostat is infinite.

Equations (9) and (10) contain only the average value of the stochastic density matrix $\rho(t)$ of the DS. Its higher statistical moments

$$\langle\rho(t)\otimes\ldots\otimes\rho(t)\rangle$$ (13)

describe several copies of the DS interacting with one common bath. The indistinguishability of the copies requires specifying their quantum statistics. According to [1], the case of Fermi statistics reduces to the analysis of moments (13). In this case, an additional (e.g., Coulomb) interaction between the copies of the DS can be included as an interaction through a second (Gaussian) bath [additional pairs of sources $x(t)$ and $y(t)$].

2. We apply this formalism to a two-level DS (TLDS) interacting with a Gaussian bath. We can set

$$J = \begin{pmatrix} 1 & 0 \\ 0 & -1 \end{pmatrix}, \quad D = \begin{pmatrix} 0 & 1 \\ 1 & 0 \end{pmatrix},$$ (14)

and $H_d(t) = u(t)J/2$. Here, $u(t)$ is the energy difference between the states, which possibly depends on time as a result of an external action on the TLDS. The operator D is responsible for contact with the bath, which induces random switches of the TLDS between its states. The operator J corresponds to the observation of
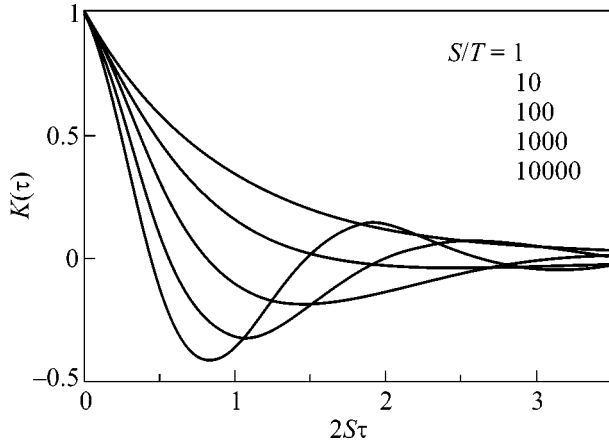
Fig. 1. Correlation function of the two-level dynamic system for the relative intensity of white noise of the bath $S/T =$ (from top to bottom) 1, 10, 100, 1000, and 10 000.

Fig. 2. Ratio Δ/Δ_0 of the coefficients of diffusion calculated including and neglecting the dissipative reaction of the bath vs. the relative intensity of (1) white and (2) low-frequency Lorentzian bath noise with $\tau_0 T = 10$.

the state such as the spin orientation or the velocity of a quantum particle in the simplest model of one-dimensional Brownian motion. This model illustrates the role of the $y(t)$ component of a random source, i.e., the dissipative term $y(t)D \circ \rho(t)$ in Eqs. (5) and (6).

Let the initial states of the free TLDS have the same energy; i.e., $u(t) \equiv 0$. Differential stochastic equation (5), (6) is explicitly integrable. In particular, the trace

$$\theta(t, v) \equiv \mathrm{Tr}_D \rho(t) = \rho_{11} + \rho_{22}$$

satisfies the recurrence relation

$$\theta(t, v) = Y(t, -\infty)$$

$$+ \int\limits_{t > t_1 > t_2} Y(t, t_1) v(t_1) X(t_1, t_2) v(t_2) \theta(t_2, v) dt_1 dt_2, \quad (15)$$

where

$$X(t_1, t_2) \equiv \cos\left[2 \int\limits_{t_2}^{t_1} x(t') dt'\right],$$

$$Y(t_1, t_2) \equiv \cosh\left[\int\limits_{t_2}^{t_1} y(t') dt'\right].$$

In this case, $\Xi(t, v) = \langle \theta(t, v) \rangle$.

We analyze the correlation function of fluctuations of spin (or Brownian-particle velocity, etc.) $K(\tau) = \langle J(\tau)J(0) \rangle$ and the diffusion coefficient $\Delta = \int_0^\infty K(\tau) d\tau$. The most interesting case is the case of white noise of the bath in the sense that $S(\omega) = \mathrm{const}$ in Eq. (12) (we emphasize, however, that both correlation functions (12) cannot simultaneously be δ functions, and quantum noise is never white in this sense). From Eq. (15), aver-
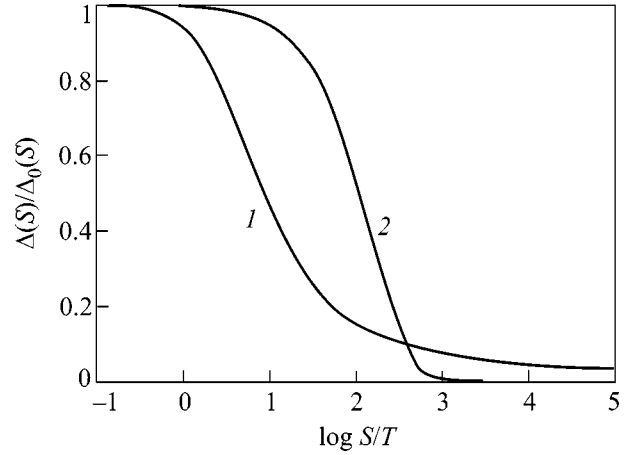
aging in view of Eq. (12) and differentiating with respect to the test function, we obtain

$$K(\tau) = e^{-2S\tau} \cos\left\{\frac{2S}{\pi} \int\limits_0^\tau \ln \tanh\left(\frac{\pi T \tau'}{2}\right) d\tau'\right\}. \quad (16)$$

Figure 1 shows that monotonic relaxation becomes oscillatory when the dimensionless noise intensity S/T increases. Formally, this is the effect of the $y(t)$ component, i.e., the feedback effect of the TLDS on the bath [in the absence of $y(t)$, correlation would be purely exponential for any S/T value].

However, the opposite approximation

$$S(\omega) = S/[1 + (\tau_0 \omega)^2], \quad \tau_0 T \gg 1, \quad (17)$$

where the sufficiently long time of noise correlation (bath reaction) τ_0 excludes high frequencies, can be more correct in practice. In this case, it is convenient to introduce the binding energy ϵ as $S(0) = 2\epsilon^2 \tau_0$. Calculating the correlation function under assumptions (17), we find that monotonic relaxation (close to exponential) proceeds for weak coupling ($\epsilon/T < 1$), and

$$K(\tau) \approx \exp(-2\epsilon^2 \tau^2) \cos(\epsilon^2 \tau/T), \quad (18)$$

for $\epsilon/T > 1$ (strong coupling); i.e., oscillations appear and are multiplied again.

It is clear that the relaxation oscillations mean an additional decrease in the coefficient of diffusion Δ [spectral density $J(t)$ for zero frequency] compared to its value Δ_0 in the absence of $y(t)$. Figure 2 shows this effect as a function of $S/T \equiv S(0)/T$ for (1) white noise and (2) Lorentzian noise at $T\tau_0 = 10$. In the latter case, the coefficient of diffusion can become anomalously small, leading to the localization of a Brownian particle.

Oscillatory relaxation means that the response of the TLDS to a periodic external action can become resonant, being a maximum for a nonzero frequency of the action (if the frequency is fixed, it is a maximum for nonzero bath noise). Such phenomena are known as stochastic resonance (see, e.g., review [2]).

We also note that oscillatory relaxation belongs to the type of non-Markovian processes that could not be adequately analyzed in the theory of Markovian quantum dynamical semigroups, i.e., time-local master equations (for this theory, which dates back to Lindblad's work [3], see, e.g., [4]). In terms of this theory, we consider the stochastic "expansion" of the semigroup that is non-Markovian so far as the correlation function $x(\tau)y(0)$ determining oscillations in Eq. (16) differs from the δ function.

3. Since the states are symmetric (degenerate), trace (15) contains only even powers of $v(t)$. If $u(t) \neq 0$, symmetry is violated. We define the integral operators $\hat{I}$, $\hat{C}$, and $\hat{S}$ as

$$\hat{I}f(t) = \int\limits_{-\infty}^{t} f(t')dt',$$

$$\hat{C}, \hat{S}f(t) = \int\limits_{-\infty}^{t} \cos, \sin\left\{\int\limits_{t'}^{t} u(t'')dt''\right\}f(t')dt'.$$

For $u(t) \neq 0$, the equation

$$\theta = 1 + \hat{I}y\hat{C}y\theta$$
$$+ \hat{I}(v + 2y\hat{S}x)[1 + 4\hat{I}x\hat{C}x]^{-1}\hat{I}(v + 2x\hat{S}y)\theta \tag{19}$$

can be derived instead of Eq. (15). In this case, the expression of θ in terms of $v(t)$

$$\theta(t, v) = \theta_0(t) + \int\limits_{-\infty}^{t} \tilde{J}(t_0)v(t_0)dt_0$$

$$+ \frac{1}{2}\int\limits_{-\infty}^{t}\int\limits_{-\infty}^{t} \tilde{K}(t_1, t_2)v(t_1)v(t_2)dt_1dt_2 + \dots,$$

contains the first (as well as other odd) powers. For simplicity, we consider this contribution in the limit of a hot bath, $S/T \ll 1$ and $T\tau_0 \gg 1$, when an extra $y(t)$ power introduces an additional order of smallness according to Eq. (12). Moreover, we assume that the perturbation $u(t)$ is infinitely weak. Retaining only the lowest powers of $y(t)$ and $u(t)$, we obtain

$$\tilde{J}(t_o) = J_+(t_0) + J_-(t_0), \tag{20}$$

where

$$J_+ = \int\limits_{-\infty}^{t_0} \sin\left\{2\int\limits_{t_1}^{t_0} x(t')dt'\right\}u(t_1)\int\limits_{-\infty}^{t_1} y(t_2)dt_2 dt_1,$$

$$J_- = \int\limits_{t_0}^{t} \sin\left\{2\int\limits_{t_0}^{t_1} x(t')dt'\right\}u(t_1)\int\limits_{t_1}^{t} y(t_2)dt_2 dt_1.$$

The actual observation instant of time t_0 obviously lies in the time axis earlier than the formal argument t. Under this condition, t is eliminated from the averaged results. For this reason, it is convenient to take $t = \infty$.

The function $\tilde{J}(t_0)$ obviously vanishes if the $y(t)$ component of the random source is neglected. Therefore, this component, along with $x(t)$, is responsible for the response of the DS to an external action. The integral operators acting on $u(t)$ in expressions for J_+ and J_- serve as random functions of linear response (random susceptibility, mobility, etc.), i.e., as multiplicative noise. This noise is a manifestation of the randomness (dependence on thermostat noise) of the quantum transition probabilities between states [5]. Equations (20) clearly show that the unaveraged response functions do not relax and can connect events arbitrarily distant in time.

4. In conclusion, we consider two identical TLDSs in contact with the same bath. Let these be formally distinguishable and contribute additively to an observable. Then, the characteristic functional of the total observable takes the form

$$\Xi(t, v) = \langle\theta^2(t, v)\rangle \tag{21}$$

rather than Eq. (10). In the hot-bath limit, it follows from Eq. (21) that the correlation function of this observable has the form

$$K_2(t_1, t_2) = 2\{\langle\tilde{K}(t_1, t_2)\rangle + \langle J_+(t_1)J_-(t_2)\rangle$$
$$+ \langle J_+(t_1)J_+(t_2)\rangle - 2\langle J_+(t_1)\rangle\langle J_+(t_2)\rangle\}, \tag{22}$$

where $t_1 > t_2$.

All the terms except the first in the right-hand side of Eq. (22) describe "extra" noise of the observable, which is proportional to the square of perturbation $u(t)$ and originates from (identical for both TLDSs) fluctuations of the random functions of linear response [Eq. (20)]. If $t_1 - t_2 \gg \tau_c$, where τ_c is the correlation time of fast noise of the observable [relaxation time of $K(\tau)$ in the absence of perturbation], only the second term remains and does not relax altogether. The formal order-of-magnitude estimation of this long-lived correlation gives

$$|\langle J_+(\infty)J_-(\infty)\rangle| \sim (\tau_c^2/\tau_0^2)\langle\tilde{J}\rangle^2.$$

The ratio τ_c/τ_0 is a function of the parameter $\epsilon\tau_0$ and can be either much larger than unity (for $\epsilon\tau_0 \ll 1$) or much less than unity (for $\epsilon\tau_0 \gg 1$).

We note that the term $J_-(t_0)$ in Eq. (20) corresponds to the "reaction of past to future," because it contains only future values of all variables with respect to the observation instant of time. Any correlation function in which the time argument of J_- is later is obviously equal to zero; otherwise, it is physically meaningless. However, correlations between J_- and later J_+ values do not contradict the principle of causality. The property of these correlations to be long-lived is completely similar to the properties of quantum-probability fluctuations considered in [5]. They are also caused by the coherence (unitarity) between the joint evolution of the DS and the bath. This coherence is violated by the acts of observation of the DS but conserves always between them. Contrary to [5], the consideration of unrelaxing correlations is not restricted by any time interval.

REFERENCES

1. Yu. E. Kuzovlev, cond-mat/0102171.
2. L. Gammaitoni, P. Hanngi, P. Jung, *et al.*, Rev. Mod. Phys. **70**, 223 (1998).
3. G. Lindblad, Commun. Math. Phys. **48**, 119 (1976).
4. *Quantum Random Processes and Open Systems*, Ed. by A. S. Kholevo (Mir, Moscow, 1988).
5. Yu. E. Kuzovlev, Yu. V. Medvedev, and A. M. Grishin, Pis'ma Zh. Éksp. Teor. Fiz. **72**, 832 (2000) [JETP Lett. **72**, 574 (2000)].

Translated by R. Tyapaev

Mach Cones and Magnetic Forces in Saturn's Rings[¶]

T. W. Hartquist[1] and O. Havnes[2]

[1] Department of Physics and Astronomy, University of Leeds, Leeds, LS2 9JT, UK
[2] Department of Physics, University of Tromsø, N-9037 Tromsø, Norway
Received June 2, 2003

Recently, Mamun, Shukla, and Bingham [2] claimed that Havnes and his collaborators [1] mistakenly neglected magnetic fields in their work on Mach cones as potentially powerful diagnostics of properties in Saturn's rings. We show that the magnetic force on a charged particle is entirely negligible in comparison with the electric force on the particle in a wave with a wavenumber relevant to the Saturnian Mach cone problem. Havnes *et al.* [1] were not in error. © *2003 MAIK "Nauka/Interperiodica".*

PACS numbers: 96.30.Wr; 96.30.Mh; 96.35.Pb; 52.27.Lw; 52.35.Fp

Havnes and his collaborators [1] pointed out that the detection and observation of Mach cones around larger solid bodies in Saturn's ring system would provide a valuable means of diagnosing properties of the dusty ring plasma. They based their analysis on a consideration of the properties of dust acoustic waves in an unmagnetized plasma. Recently, Mamun *et al.* [2] argued that the analysis must be based on the study of hydromagnetic waves in a dusty plasma, e.g., [3]. Here we show that Havnes *et al.* [1] were justified in the neglect of the magnetic field in their studies of Mach cones in Saturn's rings.

We consider a dust–ion plasma as in [2] and take ρ_d, ρ_i, $v_d\hat{z}$, $v_i\hat{z}$, $\rho_i c_i^2$, $Z_d e$, e, m_d, m_i, and $E\hat{z}$ to be the mass density of dust, the mass density of ions, the dust velocity, the ion velocity, the thermal pressure of the ions, the charge carried by a dust grain, the charge of a proton, the mass of a dust grain, the mass of an ion, and the electric field, where $\hat{z}$ is the unit vector in the z direction. c_i is taken to be a constant. Waves are assumed to propagate in the z direction in a uniform static background medium. Background quantities are signified by subscript 0, and perturbation quantities are signified by subscript 1. Perturbation quantities are assumed to vary with time, t, and z as $\exp(i\omega t - ikz)$.

The linearized equations governing the propagation of a dust acoustic wave in the two fluid medium are

$$i\omega\rho_{d1} - ik\rho_{d0}v_{d1} = 0, \tag{1}$$

$$i\omega\rho_{d0}v_{d1} = \frac{\rho_{d0}}{m_d}Z_d eE, \tag{2}$$

$$i\omega\rho_{i1} - ik\rho_{i0}v_{i1} = 0, \tag{3}$$

$$-ikc_i^2\rho_{i1} = \frac{\rho_{i0}}{m_i}eE, \tag{4}$$

$$-ikE = 4\pi e\left(\frac{\rho_{i1}}{m_i} + \frac{Z_d\rho_{d1}}{m_d}\right). \tag{5}$$

We have taken the pressure of the dust fluid to be zero. The dust fluid is assumed to have a much greater density than the ion fluid, leading to the neglect of the ion fluid's inertia in equation (4). We note that $\rho_{i0}/m_i = -(\rho_{d0}/m_d)Z_d$. As pointed out by Mamun *et al.* [2], for low-frequency dust waves unaffected by the magnetic field, $\omega/k = (Z_d^2\rho_{d0}k_B T_{i0}m_i/\rho_{i0}m_d^2)^{1/2}$, where k_B and T_{i0} are Boltzmann's constant and the ion temperature. $c_i = (k_B T_{i0}/m_i)^{1/2}$.

We take B_0 to be the strength of the background magnetic field. The maximum magnitude of the component of the ion velocity perpendicular to the direction of propagation is given by

$$|v_{i\perp}| = \left(\frac{e|v_{i1}|B_0}{c}\right)\left(\frac{1}{m_i\omega}\right) = \frac{\omega_{gi}}{\omega}|v_{i1}|, \tag{6}$$

where c is the speed of light and $\omega_{gi} \equiv eB_0/m_i c$ is the ion gyrofrequency.

The magnetic force per unit volume in the z direction on ions has a maximum magnitude of

$$F_{BZ} = \frac{\rho_{i0}}{m_i}e\frac{\omega_{gi}}{\omega}\frac{|v_{i1}|}{c}B_0 = \rho_{i0}\frac{\omega_{gi}^2}{\omega}|v_{i1}|. \tag{7}$$

The ratio of F_{BZ} to the magnitude of the pressure force per unit volume on the ions is

$$R \equiv \left(\rho_{i0}\frac{\omega_{gi}^2}{\omega}|v_{i1}|\right)\left(\frac{1}{k|\rho_i|c_i^2}\right) = \frac{\omega_{gi}^2}{\omega^2}\frac{\rho_{i0}}{\rho_{d0}}. \tag{8}$$

[¶] This article was submitted by the authors in English.

The magnetic force is negligible if

$$R \ll 1 . \tag{9}$$

For a magnetic field strength of 0.03 Gauss, at the corotation distance, and an ion mass of 16 amu, $\omega_{gi} \approx 18$ s^{-1}. We assume that each grain is spherical with a radius of 0.25 μm and is composed of material with a density of 1 g/cm^3. Thus, $\rho_{i0}/\rho_{d0} = 5 \times 10^{-10}|Z_d|$. For a medium in which $T_{i0} = 10$ eV, the frequency of a wave unaffected by the magnetic field is given by $\omega = 2|Z_d|^{1/2}/\lambda$, where λ is the wavelength in meters.

Condition (9) shows that the neglect of the magnetic field in the work by Havnes *et al.* [1] on Mach cones in Saturn's rings is entirely justified and that $R \approx 0.01$ for $\lambda \simeq 500$ m. An examination of the results of Mamun *et al.* [2] also shows that, for wavelengths below several hundred meters, which will be generated by boulders, the effect of the magnetic field is negligible, and their dispersion relation reduces to that of the dust acoustic wave. For wavelengths of more than about 1 km, the magnetic field becomes progressively more important and should be included. Li and Havnes [3] have performed a study of such waves in Saturn's rings based on kinetic theory with magnetized ions and electrons but unmagnetized dust. However, such large wavelengths should not be important for Mach cones generated by large boulders.

REFERENCES

1. O. Havnes, T. Aslaksen, T. W. Hartquist, *et al.*, J. Geophys. Res. **100**, 1731 (1995); J. Vac. Sci. Technol. A **14**, 525 (1996); Planet. Space Sci. **49**, 223 (2001); A. Brattli, O. Havnes, and F. Melandso, Phys. Plasmas **9**, 958 (2002).
2. A. A. Mamun, P. K. Shukla, and R. Bingham, JETP Lett. **77**, 541 (2003).
3. F. Li and O. Havnes, Planet. Space Sci. **48**, 117 (2000).

Comment on Mach Cones and Magnetic Forces in Saturn's Rings¶

P. K. Shukla, A. A. Mamun, and R. Bingham

Institut für Theoretische Physik IV, Fakultät für Physik und Astronomie,
Ruhr-Universität Bochum, D-44780 Bochum, Germany

Received June 9, 2003

We clarify the underlying physics of long-wavelength dust magnetoacoustic waves and short-wavelength (in comparison with the ion gyroradius ρ_i) dust acoustic waves that are involved in the formation of Mach cones in the magnetized dusty plasma of Saturn's rings.© *2003 MAIK "Nauka/Interperiodica".*

PACS numbers: 96.30.Wr; 96.30.Mh; 96.35.Pb; 52.27.Lw; 52.35.Fp

About eight years ago, Havnes *et al.* [1] employed the dispersion relation of Rao, Shukla, and Yu's [2] dust acoustic waves (DAWs) for an unmagnetized dusty plasma to predict the formation of dust acoustic Mach cones in Saturn's rings. The DAWs are low-frequency (in comparison with the dust plasma frequency), long-wavelength (in comparison with the dusty plasma Debye radius [3]) electrostatic waves in which the restoring force comes from the pressures of inertialess electrons and ions, while the dust mass provides the inertia to maintain the waves. Thus, Havnes *et al.* [1] used the phase speed $V_p(=\omega/k)$ of unmagnetized DAWs to obtain the Mach cone opening angle $\theta = \sin^{-1}(V_p/V_b)$, where $V_b (>V_p)$ is the speed of a dust boulder that lies in the equatorial plane of Saturn's rings, which shall provide valuable information regarding the plasma and dust parameters once the *Cassini* spacecraft starts gathering data in July 2004. Since the dusty plasma in Saturn's rings is magnetized, it is very important to understand the properties of waves in a dusty magnetoplasma [3].

In a recent letter, Mamun, Shukla, and Bingham [4] predicted the formation of Mach cones involving low-frequency (in comparison with the dust gyrofrequency ω_{cd}), long-wavelength (in comparison with the ion gyroradius ρ_i) slow dust magnetoacoustic waves in an ion–dust plasma. Mamun *et al.* [4] found that, for the plasma parameters of Saturn's rings (viz. Saturn's magnetic field $B_0 \sim 0.1$ G, the dust number density $n_d = 10$ cm^{-3}, the dust charge number $Z_d \sim 10^3$, the dust material mass density 1 g/cm^3, the dust radius 0.5 μm, the ion number density $n_i \sim 10^4$ cm^{-3}, the ion temperature $T_i \sim 10$ eV, the ion Debye radius $\lambda_{Di} \simeq 23$ cm, and ion gyroradius $\rho_i \sim 45$ m), the dust Alfvén speed $V_{Ad}(=B_0/\sqrt{4\pi n_d m_d})$ is much larger than the DAW

speed $C_D[=(Z_d^2 n_d T_i/n_i m_d)^{1/2}]$, since Saturn's plasma parameter $\beta(=8\pi n_i T_i/B_0^2)$ is fairly low (~10^{-4}), where m_d is the mass of the dust particle. Accordingly, they suggested that long-wavelength slow dust magnetoacoustic waves propagating almost perpendicular to the external magnetic field direction are a viable candidate for Mach cone formation in the equatorial region of Saturn's rings, where a dust boulder moves in a Keplerian orbit. Hartquist and Havnes [5] refute this scenario, since they failed to derive dispersion relations (8) and (9) in [4], which have been obtained from our exact equations (4) and (5). It should be stressed that the forms of the low-frequency ($\ll \omega_{cd} = Z_d eB_0/m_d c$, where e is the magnitude of the electron charge and c is the speed of light in vacuum) dust shear Alfvén and dust magnetoacoustic wave dispersion relations in an ion–dust plasma are identical to those of hydromagnetic waves in an electron–ion plasma [6], except that the role of electrons and ions is replaced by ions and dust, respectively. It turns out that, in the phase speed of the dust magnetoacoustic waves, we have the dust Alfvén speed $(B_0/\sqrt{4\pi n_d m_d})$ and the ion skin depth (c/ω_{pi}), in contrast to the usual Alfvén speed $(B_0/\sqrt{4\pi n_i m_i})$ and the electron skin depth (c/ω_{pe}) in an electron–ion plasma, where ω_{pi} (ω_{pe}) is the ion (electron) plasma frequency and m_i is the ion mass. Thus, in slow dust magnetoacoustic waves, the restoring force comes from the magnetic pressure and the dust mass provides the inertia. The wave dispersion is due to the ion inertial force. For Saturn's plasma parameters, the wavelengths of slow dust magnetoacoustic waves, which could be involved in the formation of Mach cones, are in the range of several hundred meters to a few kilometers, depending on the values of B_0, which vary between 0.025–0.2 G in Saturn's rings, where $c/\omega_{pi} \simeq 3.5$ km. As an illustration, we mention that, for 2-km scale size

¶This article was submitted by the authors in English.

slow dust magnetoacoustic waves, we have $V_b/V_p \simeq 1.1$, 3.8, and 3.8 for $B_0 = 0.01$, 0.05, and 0.1 G, respectively.

Furthermore, we have critically examined the arguments of Hartquist and Havnes [5] regarding the neglect of the Lorentz force in the ion dynamics involved in *short-wavelength, electrostatic DAWs* in a magnetized dusty plasma that we discussed in [4, p. 645]. We note that a fluid ion response, given by Eq. (4) in [5], is incorrect for short-wavelength ($b_i = k_\perp^2 \rho_i^2$ $\geqslant 1$, where $\mathbf{k}_\perp$ is the component of the wavevector $\mathbf{k}$ perpendicular to Saturn's magnetic field $\hat{\mathbf{z}} B_0$ and $\hat{\mathbf{z}}$ is the unit vector along the z axis) DAWs. For low-frequency ($\omega \ll \omega_{ci} = eB_0/m_i c$) arbitrary-wavelength electrostatic modes, we must use, instead of Eq. (4) in [5], the ion density perturbation [7]

$$n_{i1} = -n_i \left[1 - \Gamma_0(b_i) + 2\Gamma_1(b_i) \frac{\omega^2}{\omega_{ci}^2} \right] \frac{e\phi}{T_i}, \qquad (1)$$

for two-dimensional ions in equatorial plane of Saturn's rings. Here, $\Gamma_{0,1}(b_i) = I_{0,1}(b_i)\exp(-b_i)$, $I_0(I_1)$ is the modified Bessel function of zero (first) order and ϕ is the DAW potential. For $b_i \geqslant 1$, we can approximate Eq. (1) as

$$n_{i1} = -\frac{n_i e\phi}{T_i}, \qquad (2)$$

which is a Boltzmann distribution associated with an ion susceptibility $\chi_i \approx 1/k^2\lambda_{Di}^2$, where $\lambda_{Di} = (T_i/4\pi n_i e^2)^{1/2}$ is the ion Debye radius. Equation (2) physically dictates that, in the potential of short-wavelength DAWs, unmagnetized ions execute a straight-line orbit across $\hat{\mathbf{z}}$ and they charge neutralize negatively charged dust, which has very slow motion. The dust number density perturbation n_{d1} for $\omega^2 \gg \omega_{cd}^2$ is [3]

$$n_{d1} = -\frac{n_d Z_d e}{m_d} k^2 \phi. \qquad (3)$$

For $\omega \ll k_z V_{Te}$, $\omega_{ce} k_z/k_\perp$, where k_z is the component of the wavevector along $\hat{\mathbf{z}}$, V_{Te} is the electron thermal speed, and ω_{ce} is the electron gyrofrequency, the electrons rapidly thermalize along $\hat{\mathbf{z}}$ and establish a Boltzmann distribution. The corresponding electron number density perturbation is

$$n_{e1} = \frac{n_e e\phi}{T_e}, \qquad (4)$$

where T_e is the electron temperature and $n_e = n_i - Z_d n_d$. Substituting (2), (3), and (4) into the Fourier-trans-

formed Poisson equation, we have the frequency of short-wavelength dispersive DAWs

$$\omega = \frac{k\lambda_{Di}\omega_{pd}}{(1 + \sigma + k^2\lambda_{Di}^2)^{1/2}} \equiv \frac{kC_D}{(1 + \sigma + k^2\lambda_{Di}^2)^{1/2}}, \qquad (5)$$

which coincides with Rao, Shukla, and Yu's unmagnetized DAW frequency that Havnes *et al.* [1] employed to predict the DAW Mach cone in Saturn's rings. Here, $\omega_{pd} = (4\pi Z_d^2 e^2 n_d/m_d)^{1/2}$ is the dust plasma frequency and $\sigma = n_e T_i/n_i T_e \ll 1$. It turns out that, for Saturn's plasma parameters, the wavelengths of the DAWs should be ~30 m for $\omega \simeq 1 \text{ s}^{-1}$, $T_i = 10$ eV, $T_e = 10 T_i$, $n_i = 10^4 \text{ cm}^{-3}$, $n_e = 0.1 n_i$, $\omega_{pd} \simeq 21 \text{ s}^{-1}$, and $\lambda_{Di} \simeq 23$ cm.

In conclusion, we have discussed the drawbacks of the research carried out in [5] and have clarified the underlying physics of low-frequency ($\ll\omega_{cd}$), long-wavelength ($k_\perp^2 \rho_i^2 \ll 1$) slow dust magnetoacoustic waves and short-wavelength ($k_\perp^2 \rho_i^2 \gg 1$) intermediate-frequency ($\omega_{cd} \ll \omega \ll \omega_{ci}$) DAWs that may participate in the formation of Mach cones in Saturn's rings. These transverse and longitudinal waves in magnetized dusty plasmas can be generated by ion temperature anisotropy and electron/ion beams. The resonance interaction between a dust boulder and short- and long-wavelength modes, as discussed here, can give rise to Mach cones in the equatorial plane of Saturn's rings, which should be detectable by the onboard instruments of the *Cassini* spacecraft.

REFERENCES

1. O. Havnes, T. Aslaksen, T. W. Hartquist, *et al.*, J. Geophys. Res. **100**, 1731 (1995).
2. N. N. Rao, P. K. Shukla, and M. Y. Yu, Planet. Space Sci. **38**, 543 (1990).
3. P. K. Shukla and A. A. Mamun, *Introduction to Dusty Plasma Physics* (Inst. of Physics, Bristol, 2002).
4. A. A. Mamun, P. K. Shukla, and R. Bingham, JETP Lett. **77**, 541 (2003).
5. T. W. Hartquist and O. Havnes, JETP Lett. **78**, 97 (2003).
6. A. I. Akhiezer, I. A. Akhiezer, R. V. Polovin, A. G. Sitenko, and K. N. Stepanov, *Plasma Electrodynamics: Linear Theory* (Nauka, Moscow, 1974; Pergamon, New York, 1975), Vol. 1; Y. Ohsawa, J. Phys. Soc. Jpn. **54**, 4073 (1985).
7. M. Brambilla, *Kinetic Theory of Plasma Waves* (Clarendon Press, Oxford, 1998), p. 333.